Investigation of Light Absorption and Emission in Ge and GeSn Films Grown on Si Substrates

by

Jay Mathews

A Dissertation Presented in Partial Fulfillment
of the Requirements for the Degree
Doctor of Philosophy

Approved April 2011 by the
Graduate Supervisory Committee:

José Menéndez, Co-Chair
John Kouvetakis, Co-Chair
Fernando Ponce
Jeffery Drucker
Andrew Chizmeshya

ARIZONA STATE UNIVERSITY

May 2011

ABSTRACT

$Ge_{1-y}Sn_y$ alloys represent a new class of photonic materials for integrated optoelectronics on Si. In this work, the electrical and optical properties of $Ge_{1-y}Sn_y$ alloy films grown on Si, with concentrations in the range $0 \leq y \leq 0.04$, are studied via a variety of methods. The first microelectronic devices from GeSn films were fabricated using newly developed CMOS-compatible protocols, and the devices were characterized with respect to their electrical properties and optical response. The detectors were found to have a detection range that extends into the near-IR, and the detection edge is found to shift to longer wavelengths with increasing Sn content, mainly due to the compositional dependence of the direct band gap E_0. With only 2 % Sn, all of the telecommunication bands are covered by a single detector.

Room temperature photoluminescence was observed from GeSn films with Sn content up to 4 %. The peak wavelength of the emission was found to shift to lower energies with increasing Sn content, corresponding to the decrease in the direct band gap E_0 of the material. An additional peak in the spectrum was assigned to the indirect band gap. The separation between the direct and indirect peaks was found to decrease with increasing Sn concentration, as expected. Electroluminescence was also observed from Ge/Si and $Ge_{0.98}Sn_{0.02}$ photodiodes under forward bias, and the luminescence spectra were found to match well with the observed photoluminescence

spectra. A theoretical expression was developed for the luminescence due to the direct band gap and fit to the data.

ACKNOWLEDGMENTS

This work could not have been done without the help of the other people in my research group. Dr. Radek Roucka directed the device fabrication and characterization project, as well as the electro-/photoluminescence project. Without his knowledge and insight, this work could not have happened. Dr. John Tolle, Richard Beeler, Chang'e Weng, Junqi (Jerry) Xie, Chi (Seth) Xu, and Liying Jiang contributed to the growth and characterization of materials. Dr. Vijay D'Costa performed spectroscopic ellipsometry and helped with understanding the optical properties of materials. My advisors, Profs. John Kouvetakis and José Menéndez, were also instrumental in this work. Without their support and knowledge, this project would not have gone anywhere.

Additionally, I would like to acknowledge the support provided by ASU. The departments of Physics and Chemistry & Biochemistry both provided logistical support. I also gratefully acknowledge the use of the facilities and equipment of the Center for Solid State Electronics Research (CSSER), Center for Solid State Science (CSSS), and the Center for High Resolution Electron Microscopy (CHREM) at Arizona State University.

This research was funded, in part, by the U.S. Department of Energy under contract DE-FG36-08GO18003, the U.S. Air Force Office of Scientific Research Multi-disciplinary Research Initiative (MURI) under contract DOD AFOSR FA9550-06-01-0442, the National Science Foundation under grant

DMR-0907600, and the Interconnect Focus Center (IFC), one of the Semiconductor Research Corporation/DARPA Focus Centers.

TABLE OF CONTENTS

Page

LIST OF TABLES ix

LIST OF FIGURES x

CHAPTER

I. BACKGROUND AND MOTIVATION 1

A. Introduction 1

B. Early development of germanium as an electronic material 2

C. Germanium and its role in semiconductor optoelectronics 10

1. Band Structure 10

2. Optical absorption in germanium 12

3. Light emission in germanium 20

4. Epitaxial growth of germanium on silicon 25

D. A new approach: Extension of optical properties of germanium via tin alloying 29

1. Band Structure and optical properties of $Ge_{1-y}Sn_y$ alloys 29

2. Growth of $Ge_{1-y}Sn_y$ alloys 35

II. INVESTIGATION OF LIGHT ABSORPTION IN GE AND GESN FILMS GROWN ON SI 37

A. Fabrication and characterization of photoconductors from $Ge_{1-y}Sn_y$ films grown on Si 37

1. Introduction 37

2. Materials and methods 37

CHAPTER Page

(a) Fabrication of microelectronic devices 37

(b) Electrical and optical device characterization 41

3. Theory 43

4. Results and discussion 50

(a) Device processing and fabrication 50

(b) Electrical and optical properties of devices 53

5. Conclusions 62

B. Fabrication and characterization of *p-i-n* heterostructure photodiodes from $Ge_{1-y}Sn_y$ films on Si 62

1. Introduction 62

2. Materials and methods 63

3. Theory 66

4. Results and discussion 73

(a) Photodiode fabrication 73

(b) Characterization of Ge/Si photodiodes 77

(c) Characterization of $Ge_{0.98}Sn_{0.02}$/Si photodiodes 84

(d) Characterization of $Ge_{0.99}Sn_{0.01}$/Si photodiodes 87

(e) Characterization of $Ge_{0.998}Sn_{0.002}$/Si photodiodes 91

(e) Characterization of $Ge_{0.97}Sn_{0.03}$/Si photodiodes 99

5. Conclusions 101

III. INVESTIGATION OF LIGHT EMISSION IN GE AND GESN FILMS GROWN ON SI 106

CHAPTER Page

A. Room temperature photoluminescence in $Ge_{1-y}Sn_y$ films 106

1. Introduction 106

2. Materials and methods.....106

3. Theory.....110

4. Results and discussion 116

(a) Annealing of GeSn films in H_2 ambient 116

(b) Photoluminescence measurements 121

5. Conclusions.....131

B. Electroluminescence from Ge and $Ge_{0.98}Sn_{0.02}$ *p-i-n* heterostructure diodes.....132

1. Introduction 132

2. Materials and methods.....132

3. Theory.....134

4. Results and discussion 136

5. Conclusions.....141

IV. CONCLUSIONS AND SUGGESTIONS FOR FURTHER WORK.....142

REFERENCES.....145

APPENDIX

A Fabrication and processing protocols.....154

B Electro-optical device characterization apparatus.....166

C Room temperature photoluminescence and electroluminescence measurement apparatus.....175

CHAPTER Page

D Permissions for reprinted materials 193

LIST OF TABLES

Table Page

I. Sn content, thicknesses, and doping concentrations of $Ge_{1-y}Sn_y$ layers used for fabrication of photoconductors..... 38

II. Summary of results of measurements of photocurrents on photoconductors fabricated from undoped layers..... 55

III. List of substrate resistivities, Sn concentrations, layer thicknesses, and doping concentrations for heterostructures that were processed into devices. 65

IV. Band structure and elastic parameters for pure Ge used to compute the optical absorption..... 73

V. List of growth methods, Sn contents, and thicknesses for the $Ge_{1-y}Sn_y$ films prepared for photoluminescence..... 108

VI. Sn concentrations, optimal annealing temperatures, and measured bi-axial tensile strains in the H_2-annealed $Ge_{1-y}Sn_y$ films..... 120

VII. List of Sn contents, thickness of intrinsic layers, thickness of and doping concentration in capping layers, and residual tensile strains for the two heterostructures in this study..... 133

LIST OF FIGURES

Figure Page

1. Picture of the first point-contact transistor created by Bardeen and Brattain at Bell Labs 4
2. Energy versus wave vector diagram showing the band structure of Ge as calculated by Herman using orthogonalized plane waves and some experimental data 6
3. Picture of the first integrated circuit created by J. Kilby in 1958..... 8
4. Energy versus wave vector diagram showing the electronic band structure of Ge 10
5. Fraction of solar spectrum captured by Ge as a function of layer thickness 18
6. Diagram showing transition from indirect to direct band gap material in Ge with application of biaxial tensile strain, and plot of the values of the energy gaps in Ge at the L- and Γ-points as a function of tensile strain 24
7. Energy versus wave vector diagram showing the electronic band structures of Ge and α-Sn 30
8. Plot showing the difference in energy between the minima of the conduction band in $Ge_{1-y}Sn_y$ at the Γ- and L-points as a function of both tensile strain and Sn concentration 33
9. Schematic of GeSn photoconductor device design 39

Figure Page

10. Diagram of circuit used for measurement of optical response of photoconductors 42

11. Diagram of an ideal photoconductor consisting of a slab of semiconducting material with metal electrodes on either end.. 44

12. SEM image of a GeSn film on Si that has been etched by RIE..... 51

13. Optical image of fully fabricated 250×250 μm^2 $Ge_{0.98}Sn_{0.02}$ photoconductors 52

14. I-V curve for a 250×250 μm^2 photoconductor made from undoped and *n*-type (inset) $Ge_{0.98}Sn_{0,02}$ layers 53

15. Diagram showing equivalent circuit for *n*-type $Ge_{0.98}Sn_{0.02}$ photoconductors 54

16. Plot of photocurrents vs. incident light power obtained from devices fabricated from an undoped $Ge_{0.98}Sn_{0.02}$ film for a variety of bias voltages..... 56

17. Plot of photocurrent vs. product of incident light power and voltage across device obtained from a 259×250 μm^2 device fabricated from an undoped $Ge_{0.98}Sn_{0.02}$ film 58

18. Plot of external quantum efficiency vs. wavelength of incident light measured on 250×250 μm^2 photoconductor fabricated from sample APD24A 60

Figure Page

19. Absorption coefficients of bulk Ge and $Ge_{0.98}Sn_{0.02}$ as measured by spectroscopic ellipsometry 61

20. Schematic cross-sectional view and plan view of the GeSn/Si *n-i-p* heterostructure diode design 63

21. SIMS profile obtained from a pure Ge sample showing the atomic concentrations of Ge, Si, and P in the sample as a function of depth 64

22. SEM image (900x) of device fabricated from $Ge_{0.98}Sn_{0.02}$ films that did not show diode-like electrical characteristics 75

23. SEM image (4500x) of device fabricated from $Ge_{0.98}Sn_{0.02}$ films that did not show diode-like electrical characteristics 76

24. Current density (A/cm^2) curves for photodiodes with diameters ranging from 60 to 250 μm for samples with intrinsic region thickness of 350 and 900 nm 78

25. Dark current versus dislocation density plot showing a best fit through the data of Colace and Assanto and the corresponding extrapolation into the regime of our electrical measurement 79

26. Arrhenius plot of the dark current showing an increase of the activation energy with increasing reverse bias 80

27. Experimental and theoretical EQE plots for two Ge/Si diode devices 81

Figure Page

28. I–V curves of the 900-nm Ge photodiode without and under illumination 82

29. EQE dependence on reverse bias of the 900-nm Ge photodiode without and under illumination by a 0.6 mW laser diode operating at 1300 nm 83

30. Dark current density plots for the $Ge_{0.98}Sn_{0.02}$ photodiodes with mesa diameters ranging from 60 to 250 μm and active layer thickness of 350 nm..... 85

31. Arrhenius plots (natural log of dark current versus 1/kT) of devices with 250 μm diameter..... 86

32. Experimental and theoretical EQE of $Ge_{0.98}Sn_{0.02}$ photodiode 87

33. Dark current density vs. voltage curves for various sized diodes fabricated from $Ge_{0.99}Sn_{0.01}$ films..... 88

34. Current vs. voltage curves for a 300 μm $Ge_{0.99}Sn_{0.02}$ photodiode with and without illumination by a 1300 nm laser at 0.6 mW... 89

35. EQE at zero bias of a 300 μm diameter $Ge_{0.99}Sn_{0.01}$ photodiode is plotted as a function of wavelength..... 90

36. Arrhenius plots of the dark current density at selected reverse bias values for a 100 μm $Ge_{0.998}Sn_{0.002}$ diode 92

37. Experimental and theoretical EQE obtained from 300 μm diameter $Ge_{0.998}Sn_{0.002}$ and pure Ge photodiodes..... 94

Figure Page

38. Experimental and theoretical derivatives of responsivity for the two diodes in FIG. 36 95

39. Responsivity vs bias of $Ge_{0.998}Sn_{0.002}$ photodiode under illumination by a laser diode at 1300 and 1550 nm 98

40. Current-voltage curves obtained from diodes fabricated from $Ge_{0.97}Sn_{0.03}$ films 100

41. EQE vs. wavelength obtained from a $Ge_{0.97}Sn_{0.03}$ photodiode at zero bias 101

42. Dark current densities obtained from 250 μm photodiodes with varying Sn content 102

43. EQE curves obtained from 300 μm diameter photodiodes with varying Sn concentration 104

44. Random RBS spectra of $Ge_{1-y}Sn_y$ films containing 0.6, 1.5, and 3.0 % Sn 107

45. Representative plot showing 2θ/ω scan of a GeSn film before and after annealing in H_2 ambient 118

46. Plot of 2θ/ω scan of $Ge_{0.96}Sn_{0.04}$ film after annealing past the critical temperature 118

47. Plot of ω rocking curve scan of peak from (004) reflection from a $Ge_{0.975}Sn_{0.025}$ film 119

48. Photoluminescence spectra obtained from $Ge_{1-y}Sn_y$ films under 400 mW illumination by 980 nm laser 122

Figure Page

49. Comparison of PL spectrum obtained from bulk Ge wafer with that obtained from a pure Ge film 123

50. Plot of emission energy of direct gap peaks from $Ge_{1-y}Sn_y$ films as a function of Sn concentration *y* 126

51. Plot of energy separation between peaks assigned to the direct and indirect band gaps in $Ge_{1-y}Sn_y$ films as a function of Sn concentration *y* 127

52. The experimental PL spectra are compared with the fits obtained using the theoretical expression in Eq. 89 128

53. Measured PL spectrum and theoretical fit for 4% Sn sample under 400 mW illumination by 980 nm laser 129

54. Diagrams illustrating the structures of the *p*-Si/*i*-Ge/*n*-Ge and *p*-Si/*i*-GeSn/*n*-GeSn heterostructure diodes 133

55. Electroluminescence (EL) signal from the Ge and GeSn diode devices compared with room temperature photoluminescence (PL) spectra from similarly grown Ge and GeSn layers 136

56. Electroluminescence spectra from Si/Ge and $Si/Ge_{0.98}Sn_{0.02}$ heterostructure *p*-*i*-*n* diodes as a function of the injection current density 137

57. Experimental electroluminescence peak intensities and corresponding theoretical predictions based on Eq. 89 139

I. BACKGROUND AND MOTIVATION

A. Introduction

In today's world, semiconductor devices play important roles in almost every aspect of our lives. From computers to cell phones to iPods, the consumer market is dominated by semiconductor electronics. Even the most mundane parts of our existence are tied to electronics. Their role in areas such as transportation, power generation and distribution, national defense, and communication is crucial to our society. As technology develops, so does our need for new technology to push to the next level. We need faster computers capable of transmitting and storing more data than ever before. At the same time, our power needs must be met and our energy efficiency must increase. Photonic materials have a role to play in solving all of these problems.

Germanium-tin alloys represent a new class of photonic materials, which present a unique opportunity in materials science. For the first time, it may be possible to realize direct band gap materials entirely from Group IV alloys for optoelectronics integrated on Si. These materials could pave the way for new infrared lasers, high-efficiency extended range photodetectors, high-speed optical interconnects in Si-based microprocessors, and next-generation solar cells.

This thesis will present the results of research on the optical properties of crystalline $Ge_{1-y}Sn_y$ ($0 \leq y \leq 0.05$) alloys grown epitaxially on Si substrates

and the realization of the first microelectronic devices produced from such films. The subjects of light absorption and light emission in these novel alloys were studied through optical characterization of the materials, as well as through electrical and optical characterization of microelectronic devices fabricated from them. The focus is on understanding how the direct and indirect band gaps shift as Sn is incorporated into the Ge lattice, and how the optical absorption and emission properties are affected.

Chapter I presents the history of Ge as an electronic material and a description of its optical properties, followed by an introduction to GeSn alloys and their properties. Chapter II presents the results of the fabrication and characterization of the first microelectronic photodetectors based on GeSn alloys and compares the results with similar detectors made from pure Ge. In Chapter III, the results of photoluminescence and electroluminescence spectroscopy on a range of Ge and GeSn materials and devices are presented. Chapter IV covers some peripheral work on cathodoluminescence studies in InGaAs films grown on Ge-on-Si virtual substrates. In Chapter V, the results will be summarized and suggestions for further work will be presented.

B. Early development of germanium as an electronic material

Germanium has a long and interesting history. Despite the fact that the semiconductor industry of today is based on silicon, germanium was actually the driving force behind early semiconductor theory and the innovations that led to what we know today as electronics.[1,2]

In 1869, Mendeleev published "On the Relationship of the Properties of the Elements to their Atomic Weights," in which he created a table of the known elements.[3] In his paper, he also predicted the existence of several new, as yet undiscovered, atoms. In fact, he predicted an element with atomic weight 70 between the known elements Si and Sn, which he called "eka-silicon". In 1886, Winkler was studying the silver-rich mineral argyrodite when he discovered what appeared to be the element predicted by Mendeleev.[4] Although the properties of the substance found by Winkler did not exactly match the properties predicted by Mendeleev, he still found that the atomic weight was as predicted. Winkler called this new element germanium (Ge). The fact that Mendeleev is largely credited with the creation of today's periodic table is due, in large part, to his correct prediction of Ge.

Up until the 1930's, Ge was thought of as a poorly conducting metal due to its poor quality. Accordingly, not much progress was made until the early 1940's when Lark-Horovitz started working on purification of Ge at Purdue.[5] The work was funded by the war effort in order to produce high-frequency crystal detectors for radar. The ability to produce high-quality polycrystalline Ge led to a myriad of achievements, which were summarized by Lark-Horovitz in a final report to the National Defense Research Committee (NRDC).[6] Among the breakthroughs outlined in the report was the ability to dope Ge with both *n*- and *p*-type impurities, as well as the first observation of photoelectric effects in Ge.

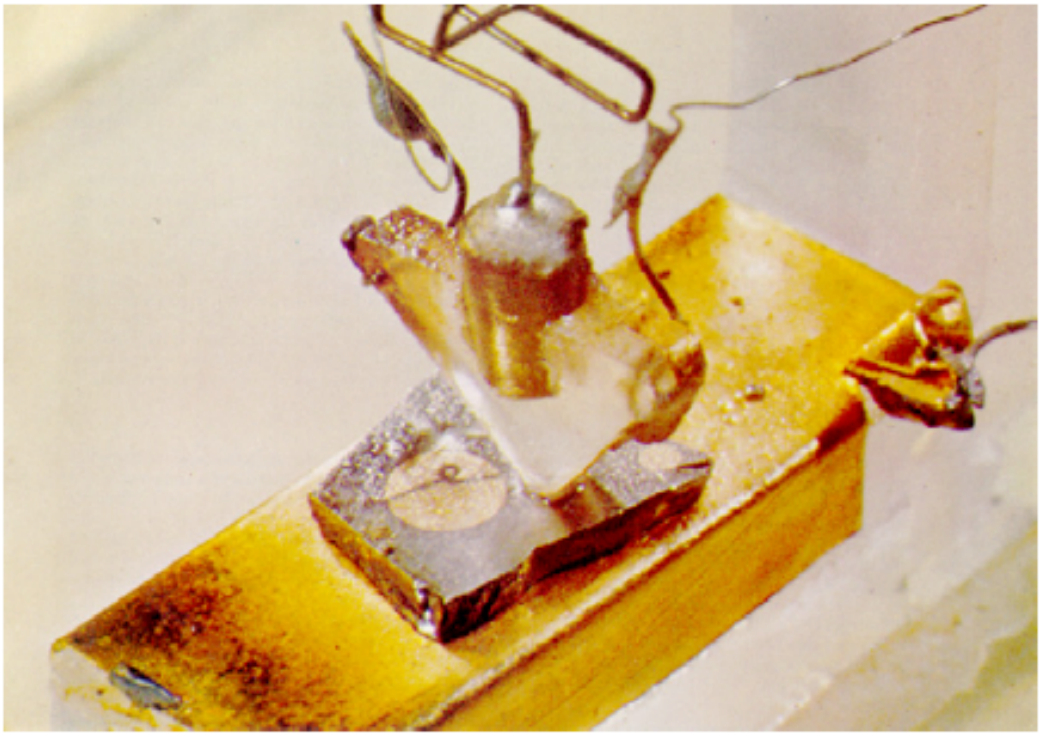

FIG. 1. Picture of the first point-contact transistor created by Bardeen and Brattain at Bell Labs. Reprinted, with permission, from *Materials Science in Semiconductor Processing*, vol. 9, issue 4-5, p. 411, August-October 2006.

The work at Purdue prompted commercial interest in applications of Ge to the area of electronics. In particular, crystal rectifiers or diodes made from Ge, such as the infamous 1N34 diode, were commercially available starting in 1946.[7] In December 1947, Bardeen and Brattain at Bell Labs created the first point-contact transistor.[8] It consisted of a piece of polycrystalline Ge obtained from Purdue[1] with two strips of gold foil held in place by a plastic wedge, as shown in FIG. 1. This "semi-conductor triode" is seen today as the beginning of modern electronics.

The work done by Lark-Horovitz started a virtual avalanche of research using Ge to understand band structure and properties of semiconductor

materials and devices. With high-quality Ge readily available, all kinds of new experiments could be performed to evaluate the behavior of this materials under different conditions.

In 1950, Johnson and Fan calculated the temperature dependence of the energy gap in Ge[9] using data from previous experiments,[3] and they found that the energy gap decreased with increasing temperature. The results agreed with theoretical predictions,[10] as well as experimental results obtained from Si.[11] In 1952, Herman used the method of orthogonalized plane waves developed by Herring[12] to calculate the band structure of diamond.[13] The calculated band structure matched well with experimental results, confirming the validity of the approach. Building on this success, Herman calculated the band structure of Ge using the same method.[14,15,16] The band structure determined by Herman is shown in FIG. 2. The minimum of the conduction band was found to occur along the [111] direction, and the lowest energy gap was calculated to be 0.65 eV at room temperature. Experimental evidence was quickly found[17,18] to confirm the band structure calculated by Herman. The value for the energy gap was found to be very close to experimental values,[6] and cyclotron resonance experiments[19] confirmed the ellipsoidal nature of the constant energy surfaces as predicted by Shockley.[20]

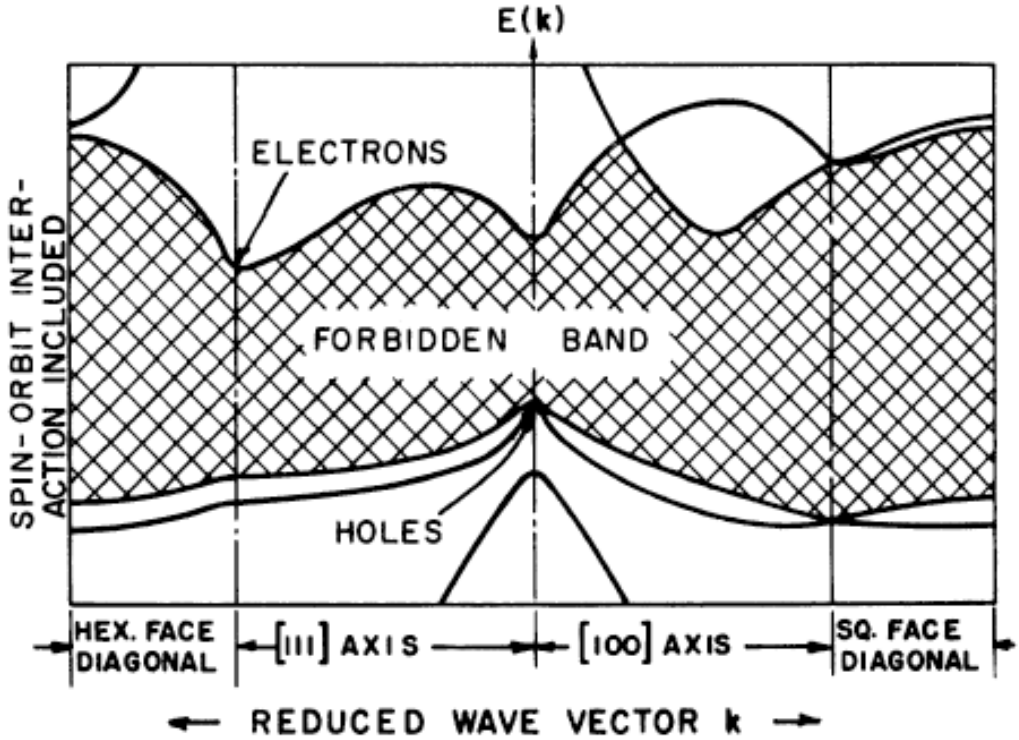

FIG. 2. Energy versus wave vector diagram showing the band structure of Ge as calculated by Herman using orthogonalized plane waves and some experimental data. © 1955 IRE (now IEEE). Reprinted, with permission, from *Proceedings of the Institute of Radio Engineers*, vol. 43, issue 12, p. 1716, December 1955.

In addition to advances in band structure theory, much progress was made in understanding the transport properties of semiconductors through the study of Ge devices. This was the birth of semiconductor device physics. Researchers such as Shockley, Haynes, and van Roosbroeck made significant contributions in this area. Advances in the interpretation of Hall measurements[21] and the realization of the first transistors[8,22] presented new opportunities for studying the movements of electrons and holes. Effects such as carrier injection[23,24] and collection[25] in transistors were studied in detail, helping to build a framework for transport properties. Mobilities and lifetimes were measured for Ge,[26,27] and a general theory of the flow of

electrons and holes was developed.[28,29] This led to further work on understanding recombination/generation[30,31] processes and the role of defects and impurities[32,33] in the electrical properties of Ge.

While the point-contact transistor was seen as a fundamental breakthrough, its design had flaws that prevented it from becoming a commercially viable product. The point contact design was not very mechanically stable, and it was very limited in the amount of current it could handle. Shockley, who had worked with Bardeen and Brattain previously and was involved with the creation of the point contact transistor, envisioned a new type of transistor that could circumvent the problems of the point contact design. This involved using *n*- and *p*-type dopants to create a "sandwich" structure with three electrodes. Today, this is known as the bipolar junction transistor.

Shockley's idea took some time to come to fruition, as advances had to be made in the growth of Ge in order to produce the *n*-*p*-*n* or *p*-*n*-*p* structures necessary for a working device. Teal and Little, working in a different group at Bell Labs, started working on growing single crystal Ge using the method outlined by Czochralski.[34] By 1950, they had developed the procedure for production of high quality, single crystal Ge.[35] Less than a year later, they were producing single crystal Ge *p*-*n* junctions,[36] which were promptly turned into solid-state rectifiers.[37] These results paved the way for Shockley's bipolar junction transistor, which was finally realized in 1951.[38]

The idea of integrated electronics preceded even the first solid-state devices. As is typical in any manufacturing setting, techniques were developed to reduce the cost of producing electronic circuits. Once solid-state transistors were in play, there was a push to try and integrate other circuit elements onto the semiconductor surface. In 1958, Kilby produced what is considered to be the first solid-state integrated circuit,[39] shown in FIG. 3. The circuit consisted of a transistor plus several resistors and capacitors made from single crystal Ge. It functioned as intended, and represents a milestone in electronics history.

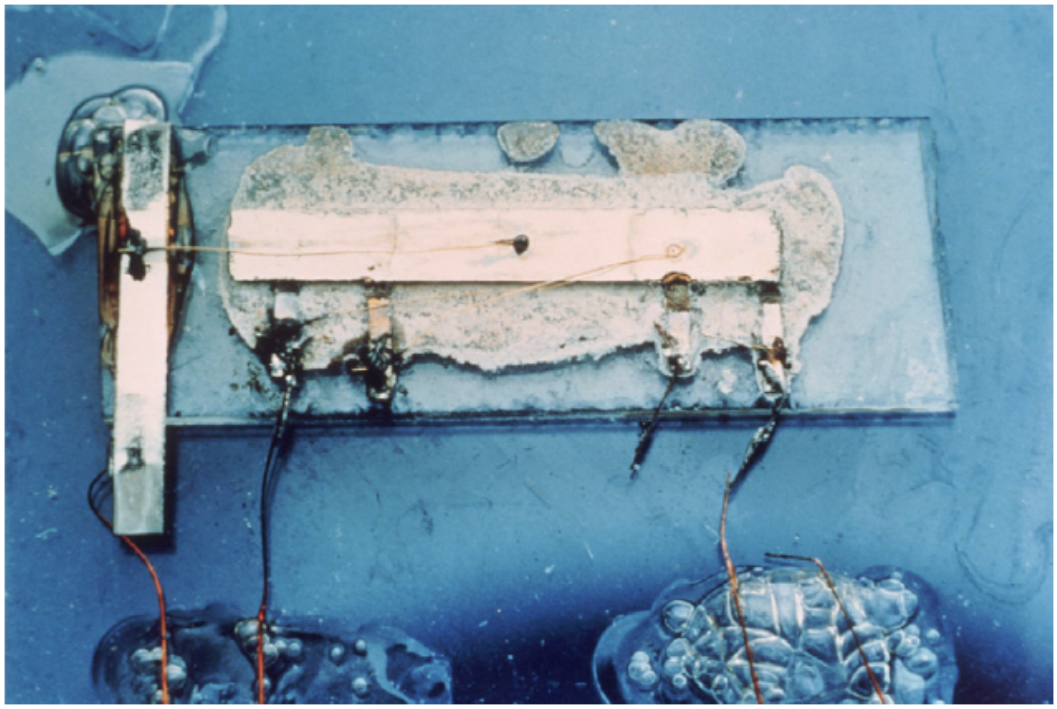

FIG. 3. Picture of the first integrated circuit created by J. Kilby in 1958. Reprinted, with permission, from *Materials Science in Semiconductor Processing*, vol. 9, issue 4-5, p. 412, August-October 2006.

At about the same time, some people at Fairchild Semiconductor were working on a similar concept using Si as the semiconductor material. Just

recently, Hoerni had shown that SiO_2 could be used as a mask for defining areas for addition of donors or acceptors via diffusion for the fabrication of diodes and transistors in Si.[40] Noyce used this new silicon planar technology to fabricate a Si-based integrated circuit.[39] This method of fabricating integrated circuits serves as the model for today's IC production. Noyce and fellow Fairchild employee Gordon E. Moore went on to found Intel, the company that produced the world's first microprocessor.

The invention of silicon planar technology proved to be the death of Ge for large-scale electronics integration. This is because of three key advantages that Si has over Ge. First, the band gap of Si is lower than that of Ge. The relatively low band gap in Ge resulted in higher intrinsic conductivity than Si at room temperature, and led to degraded performance in Ge devices at elevated temperatures. Secondly, Hoerni's work showed that SiO_2 could be used as a mask for diffusion of dopants into Si. Additionally, it is a very good electrical insulator, so individual devices could be protected by surrounding them with their native oxide. Growth of the SiO_2 could be performed very easily by heating the Si in the presence of oxygen. Lastly, the Si/SiO_2 interface has much better electrical characteristics than Ge with its native oxide. When the Ge surface is exposed to oxygen, it tends to form GeO and GeO_2.[41] These oxides tend to have a large density of surface states at the oxide/Ge interface, leading to undesirable electrical characteristics. In contrast, the Si/SiO_2 interface has a very low density of surface states. Additionally, the Ge oxides are brittle and mechanically unstable, and they can be washed off in water.

The combination of these factors caused the electronics industry to shift to Si as its primary semiconductor material.

C. Germanium and its role in semiconductor optoelectronics

1. Band structure

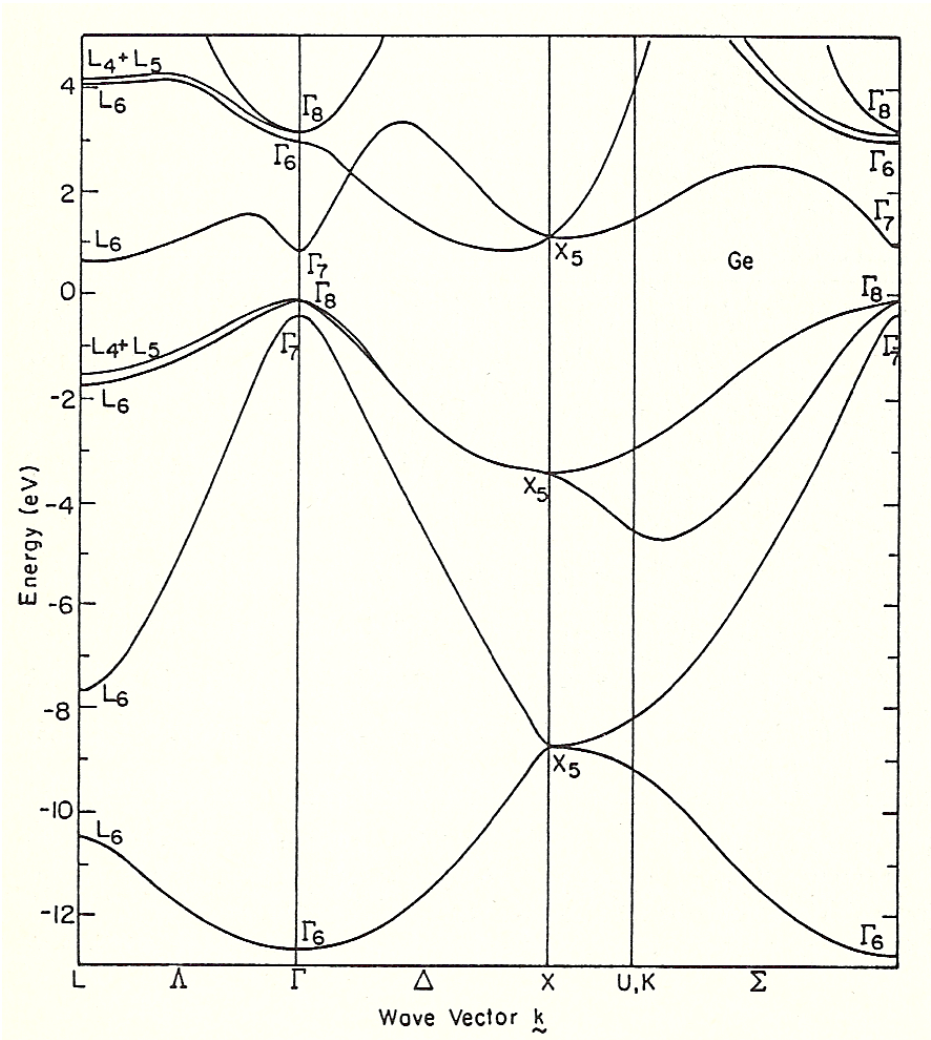

FIG. 4. Energy versus wave vector diagram showing the electronic band structure of Ge. Reprinted, with permission, from *Electronic Structure and Optical Properties of Semiconductors* (Springer-Verlag Berlin Heidelberg, New York, 1988), p. 92.

One of the interesting points listed by Lark-Horovitz in his report to the NDRC was the fact that various photo effects had been observed in Ge.[6] In early 1949, Brattain and Briggs performed the first measurement of the optical constants of Ge.[42] Later that year, continuing the work at Purdue, Lark-Horovitz and Meissner measured the reflectivity spectrum of Ge,[43] and Becker and Fan measured its infrared transmission.[44] The unique optical properties of Ge, and semiconductors in general, prompted further research to understand the optical response of Ge in terms of its band structure.

Germanium is an indirect band gap material, which can be determined by examining its band structure diagram. The lowest minimum of the conduction band does not occur at the same point in *k*-space as the maximum of the valence band, as shown in FIG. 4. This is in contrast to direct band gap materials, such as GaAs, InSb, and other III-V materials, which have the minimum of the conduction band at the center of the Brillouin zone (BZ), also called the Γ-point, which is the origin in reciprocal space. The other elemental Group IV semiconductor Si, which also has the diamond cubic structure, is an indirect band gap material as well. However, the minimum of the conduction band for Si occurs near the X-point, which is near the edge of the BZ in the [100] direction, while the minimum for Ge occurs at the L-point, which is at the edge of the BZ in the [111] direction.

In terms of optical properties, the distinction between indirect and direct band gaps is fundamental. In optically-induced transitions, energy and crystal momentum must be conserved. Indirect tetrahedral semiconductors

have their conduction band minimum away from the Brillouin zone center, while the maximum of the valence band is at the Γ-point. The difference in wave vectors between these two extrema is much larger than the wave vector of an optical photon. For crystal momentum to be conserved, there must be some additional momentum provided by another source. This extra momentum kick comes in the form of lattice vibrations, or phonons.

2. Optical absorption in germanium

Consider the case of indirect band edge absorption[45] of a photon with frequency ω. Prior to absorption, an electron has energy E_i and wave vector $\mathbf{k}_i$. After the photon is absorbed, the energy of the electron changes to E_f and its wave vector to $\mathbf{k}_f$. We must also include the absorption or emission of a phonon with frequency Ω and wave vector $\mathbf{q}$. Conservation of energy requires that

$$E_f = E_i + \hbar\omega \pm \hbar\Omega, \tag{1}$$

and conservation of momentum (neglecting that of the photon, since its momentum is very small compared to the electron and phonon momenta) requires that

$$\hbar\mathbf{k}_f \approx \hbar\mathbf{k}_i \pm \hbar\mathbf{q}. \tag{2}$$

The "±" indicates either the absorption or emission of the phonon. The "+" indicates phonon absorption, while the "-" indicates phonon emission. At room temperature, either of these cases is possible. At low temperatures,

there are very few lattice vibrations so the probability of absorbing a phonon is very low. However, phonons can still be emitted, so indirect band edge absorption is dominated by phonon emission at low temperatures.

The need for emission or absorption of phonons translates to a lower probability of absorption. Thus, the absorption coefficients for indirect semiconductors near the indirect band edge are somewhat low. The absorption coefficient increases dramatically when the photon energy is raised to a level above the direct band gap. This is because there is no longer a need for phonon emission/absorption in order to conserve momentum. In direct transitions, the momentum of the electron remains essentially unchanged by the photon absorption, so there is no requirement for phonon activity. This increases the probability of absorption and, thus, the absorption coefficient.

In the unique case of Ge, the difference between the direct and indirect band gaps at room temperature is only 140 meV.[46] The absorption is essentially zero for energies below the indirect band gap. It then increases slowly with energy until it reaches the direct band gap, at which point there is a sharp increase in absorption. This is known as the direct absorption edge. Direct band gap materials typically have very sharp absorption edges. The involvement of phonons of different energies with the indirect transition tends to broaden the absorption edge in indirect gap materials. The low band gap of Ge puts the absorption edge in the near-IR, making it useful as a material for photodetectors.

Use of Ge as a material for photodetectors was explored very early. In 1947, Benzer studied the rectification properties of Ge point contacts under illumination and found that the reverse current increased dramatically with increasing light intensity.[47] Based on this result, Shive produced the first photocell based on the Ge point contact transistor.[48] Shortly after, Becker and Fan used a Ge *p-n* junction to measure the spectral dependence of the photocurrent in Ge.[49] These first results generated much interest in the photoelectric effects in semiconductors and their possible applications for electronics,[50,51] and prompted further work to understand the physics of the interaction of light with semiconductor materials.[52,53]

Today, bulk Ge is used as a material for photodetectors in a few niche applications. Photodiodes made from bulk Ge are currently available, but the high cost of Ge wafers limits their widespread use. Additionally, the absorption of bulk Ge at 1550 nm is not quite high enough for it to be used as a detector for fiber optic communications at this wavelength. Furthermore, its absorption in the L- and U- bands is low, so III-V materials dominate the fiber optic arena.

One area where Ge is being used for its absorption properties is in the development of high-efficiency multi-junction solar cells. One of today's hottest topics in optoelectronics is the area of photovoltaics. That is, generation of electricity by conversion of solar radiation. Some of the most efficient solar cells in production are based on lattice-matched $Ge/In_{0.01}Ga_{0.99}As/In_{0.5}Ga_{0.5}P$ triple-junction architectures.[54] These cells have

achieved commercial efficiencies of up to 30%,[55] making them ideal for applications in which the cost of the solar cell is not critical, such as in spacecraft. However, their high cost has prevented their use for terrestrial applications. One way to use these more expensive cells is to use concentrators to focus the light from a large area down to the size of the cell. Using this technique, it is possible to push the efficiency of these cells past 40%.[56,57] By using low-cost optics to focus the sunlight down to a small area, the number of actual photovoltaic cells needed is reduced, so a more expensive high-efficiency cell can be used. This has brought the overall cost of the system down to reasonable levels, but further reductions are needed for this technology to become feasible for large-scale production.

State-of-the-art Ge/InGaAs/InGaP solar cells are grown on 4-6" Ge wafers, which represents more than 50% of the cost of their fabrication.[58] Ge-on-Si virtual substrates are an attractive alternative for a low-cost solution to this problem. The cost reduction per solar cell can be as high as 75% when the much lower prices and larger areas of Si wafers are considered. Additionally, larger scale system costs can be reduced due to the physical properties of the Ge-on-Si substrate relative to pure Ge. Since Si is mechanically stronger than Ge, the wafers can be made thinner than Ge wafers. This is of paramount importance for space applications, since weight is the key factor determining launch costs. For a typical 20 kW geostationary satellite mission, it has been estimated that cost savings of about $ 1.8 M per launch could be achieved by using Ge-buffer layer technologies.[58] The savings

are less substantial for concentrator photovoltaics, as the solar cell represents only 5-20% of the system cost. However, the much higher thermal conductivity of the Si substrates relative to Ge could lead to the possibility of passively cooled systems. This is especially important for applications in the American Southwest, where sunlight conditions are ideal for photovoltaic applications but elevated temperatures create additional cooling needs.

III-V solar cells have been demonstrated on Si using ultrathin Ge buffers or thick compositionally graded $Ge_{1-x}Si_x$ as templates.[59,60] In all cases, however, the Ge materials were not active components of the multijunction cell. This could be due in part to the high density of dislocations (>10^6 cm^{-2}) found in these Ge on Si buffers. An additional problem is wafer bowing due to the large thermal expansion mismatch between Ge and Si at the high processing temperatures employed (above 800 ^oC). This problem is mitigated by using ultrathin Ge buffer layers, but this implies that a Ge cell cannot not be included in this structure.

Our approach for fabrication of high-quality Ge-on-Si films may allow the integration of the multi-junction cell design on these virtual substrates. The potential feasibility of these Ge layers as bottom-cell components of the multijunction structure is illustrated in FIG. 5, which shows that a Ge thickness of ~ 5 mm is sufficient to absorb most of the solar radiation filtered by a 3-mm thick GaAs overlayer relative to the absorption by a commercial Ge wafer. Moreover, given the excess current in the Ge subcell in conventional multijunction Ge/InGaAs/InGaP cells, a reduced Ge thickness

may actually enhance the overall performance due to the associated increase in open circuit voltage. This has led Aiken[61] to propose improved Ge/InGaAs/InGaP solar cells containing thin (~1 mm) Ge cells. The theoretical increase in open circuit voltage as the Ge thickness is reduced requires a very efficient back surface passivation, and Aiken proposes to achieve this by growing the p =1×10^{16} cm^{-3} base by homoepitaxy on low resistivity (p = 1×10^{18} cm^{-3}) Ge substrates. This design is eminently transferable to our Ge-on-Si approach, since we can dope our Ge layers in situ to the specified levels.

Further theoretical modeling of the Ge bottom cell[62,63] indicates that its performance depends critically on the emitter thickness and surface recombination. Since the emitter is currently produced by diffusion, there is limited control on its structure and morphology. By contrast, our low-temperature epitaxial method based on the $(GeH_3)_3P$ precursor[64] makes it possible to fabricate arbitrarily shallow emitters with extremely sharp profiles and full control of the surface properties, further suggesting that our Ge-on-Si approach may not only lower the cost of producing Ge/InGaAs/InGaP solar cells but could actually improve their performance.

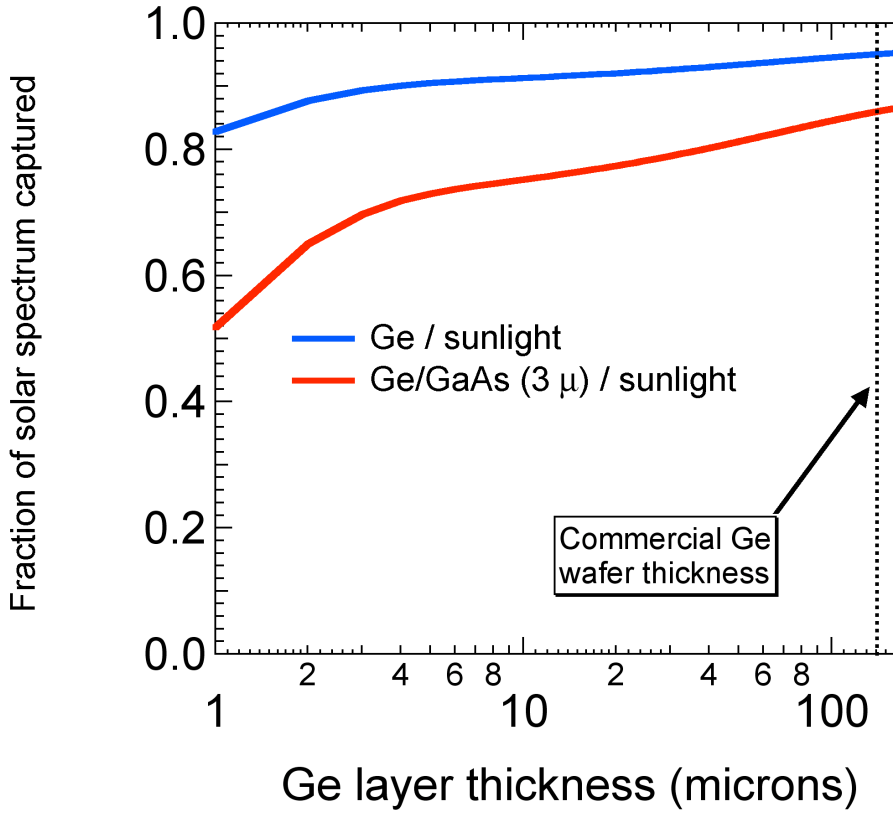

FIG. 5. Fraction of solar spectrum captured by Ge as a function of layer thickness. The plot shows that 5- microns of Ge absorb 85% of the GaAs-filtered light relative to the absorption by a Ge substrate. Reprinted, with permission, from *Solar Energy Materials and Solar Cells*, vol. 94, issue 12, p. 2363, December 2010.

Recently, Ge has seen additional interest as a material for mid- to near-IR photodetectors for Si photonic applications.[65,66,67,68] Advances in the growth of Ge-on-Si have lead to high quality, tensile-strained thin films with promising optical properties.[69] Tensile strain plays a critical role in the absorption properties of Ge. Applying tensile strain to the Ge lattice reduces both the direct and indirect band gaps.[70] This reduction in band gaps leads to a shift in the absorption edge of Ge to lower energies,[71] thereby extending the range of detection to longer wavelengths. Since the absorption edge of Ge is

near 1550 nm, the absorption at this key wavelength can be increased dramatically by introducing tensile strain.

Since Ge has a larger lattice constant that that of Si, one would think that Ge-on-Si films would be compressively strained. However, the thermal mismatch between Ge and Si plays a large role in the residual strain of Ge-on-Si films. Epitaxial Ge films are typically grown on Si at temperatures of 300-700°C, and subsequent annealing steps up to 900°C are performed to improve the quality of the Ge layers. Ge has a larger coefficient of thermal expansion than Si. When the film is cooled from the growth or annealing temperature, the Ge relaxes from its initial state of compressive strain. It contracts more quickly than the Si, leading to small amounts of residual tensile strain in the Ge layer. This idea has been used to successfully fabricate Ge-on-Si photodetectors, which exhibit extension of the detection range to longer wavelengths due to tensile strain. However, the maximum amount of tensile strain that can be achieved in Ge films grown directly on Si is 0.34%,[71] so this limits the shift of the absorption edge and, hence, the range of detection.

Several types of Ge-on-Si photodetectors have been fabricated successfully. High bandwidth metal-Ge-metal devices[72,73,74] and *p-i-n* type detectors[75,76,77] have shown promising results, although dark currents in the devices tend to be high. Accordingly, much effort has been put into reduction the dark currents through, for example, the use of high-temperature annealing to lower the density of threading dislocations.[78] The use of

heterostructure designs has yielded detectors with the lowest dark currents to date.[79] Integration of resonant cavities[80] and waveguides[81,82,83] to enhance photodetection has pushed this technology to the point where it is being used in commercial products for high-speed optical communications.[84]

3. Light emission in germanium

Band edge light emission from indirect band gap materials tends to be somewhat elusive. Physically, it is the reverse process of absorption. An electron in the conduction band and a hole in the valence band recombine. The annihilation of the electron-hole pair releases energy, which is manifested in the form of an emitted photon. The photon has an energy close to the band gap, if, as is usually the case, the electron and hole relax to the bottom and top of their respective bands before recombining.

In general, the radiative efficiency η_R of an electronic transition is given by[85]

$$\eta_R = \frac{1}{1 + \tau_R / \tau_{NR}}, \tag{3}$$

where τ_R and τ_{NR} are the radiative and non-radiative lifetimes, respectively. The non-radiative lifetime is really an effective lifetime that includes all processes by which an electron in the conduction band can transition back to the valence band without emission of a photon, such as through thermal relaxation (phonons) or interaction with defects. It is clear that the luminescent intensity will be greatest when the radiative lifetime is much

less than the non-radiative lifetime. Additionally, the presence of defects in the materials tends to decrease the non-radiative lifetime, so highly defective materials usually have very poor radiative efficiency. As with absorption, indirect band edge luminescence requires the emission or absorption of phonons with special wave vectors in order to conserve momentum. This phonon requirement leads to an increase in the radiative lifetime of the indirect band gap transition, thereby reducing the radiative efficiency. Thus, in order to observe indirect band gap luminescence in Ge at room temperature, one must use an excitation source with high energy density to increase the radiation to measurable levels.

At low temperature, the radiative efficiency of the indirect gap in Ge increases dramatically. When an electron-hole pair is formed, the negatively charged electron and net positively charged hole can be attracted through Coulomb interaction. This bound electron-hole pair is known as an exciton. Strongly bound excitons are referred to as Frenkel excitons, while those that are weakly bound are called Wannier excitons. In semiconductors, the strength of the interaction is typically fairly weak, so the excitons are Wannier excitons. If the electrons and holes are free, their wave functions do not overlap significantly, so there is a low probability for radiative transition. However, the formation of excitons leads to a strong overlap of the wave functions of the electrons and holes, so the corresponding transition probabilities are increased dramatically.

As stated previously, the minima of the conduction band at the L- and Γ-points in Ge differ by only 140 meV at room temperature.[46] While this does affect the absorption, it also has a strong effect on the luminescent properties. The occupation of the energy levels by the electrons in the conduction band will follow the Fermi distribution, which is given by

$$f(E) = \frac{1}{\exp\left(\frac{E - E_F}{kT}\right) + 1}, \tag{4}$$

where E_F is the Fermi energy. At 0 K, all states are filled up to the Fermi energy, while all other states are unfilled. As the temperature increases, more states become available for electrons to be excited into the conduction band. Since the minima of the L- and Γ-valleys are so close in energy, some electrons will occupy the states near the minimum at the Γ-point in addition to the L-point. Since the radiative lifetime of the direct band gap is very low, the population of the Γ-valley induces direct band gap luminescence in Ge. Thus, at high enough temperatures, direct band gap luminescence is observed in Ge. At low temperature, there is not enough of a tail in the Fermi distribution for there to be a significant amount of electrons in the Γ-valley, so direct band gap luminescence is not observed.

Since the population of charge carriers in the L- and Γ-valleys is determined by the distribution around the Fermi energy, it is possible to increase the carrier concentration in the Γ-valley relative to that in the L-valley by changing the Fermi level. If the Fermi energy is increased, the relative population in the Γ-valley should increase. The Fermi level in Ge can

be increased through the addition of *n*-type impurities. Thus, at finite temperatures, one should see an enhancement in the direct band gap luminescence due to an increase in *n*-type doping concentration. This effect has been seen in photoluminescence studies of *n*-type Ge-on-Si films.[86]

In addition to affecting the absorption, tensile strain has a critical role to play in the luminescence properties of Ge. In FIG. 6 (b), we plot the energy of the band gaps of Ge at the L-point $E_g(\mathrm{L})$ and at the Γ-point $E_g(\Gamma)$ as a function of tensile strain. The energy gap at the Γ-point decreases at a faster rate than that of the gap at the L-point. Thus, the energy difference between the minima of the L- and Γ-valleys decreases with increasing tensile strain. Since the relative population of the two valleys depends on their separation in energy, the tensile strain should induce a higher concentration of electrons in the Γ-valley relative to that in the L-valley. This should translate to an enhancement in the luminescence intensity of the direct gap with increasing tensile strain. This effect has been confirmed by photoluminescence measurements on mechanically stressed bulk Ge.[70]

Since the energy of the gap at the Γ-point falls faster than that at the L-point then, past some critical strain value, the band structure of Ge should transition from an indirect gap material to a direct band gap material,[87] as illustrated in FIG. 6 (a). If we examine the plots of $E_g(\mathrm{L})$ and $E_g(\Gamma)$ shown in FIG. 6 (b), we see that the two lines cross near 2%. This is the theoretical critical strain value past which Ge becomes a direct gap material.[70]

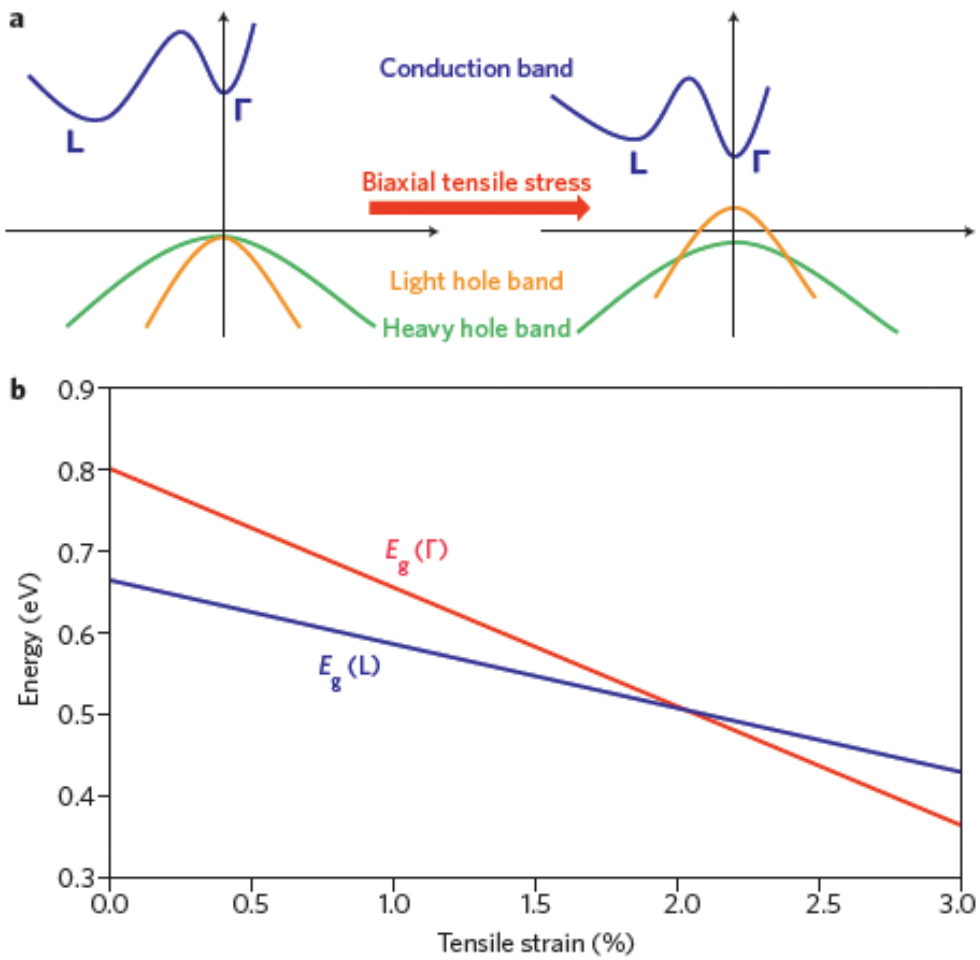

FIG. 6. (a) Diagram showing transition from indirect to direct band gap material in Ge with application of biaxial tensile strain. (b) Plot of the values of the energy gaps in Ge at the L- and Γ-points as a function of tensile strain. Reprinted, with permission, from *Nature Photonics*, vol. 4, p. 527, August 2010.

Many attempts have been made to grow highly strained Ge layers. This usually involves growth on substrates with larger lattice constants than Ge to induce the tensile strain. Recently, Huo *et al.*[88] used graded InGaAs buffer layers on GaAs substrates to produce thin Ge layers with tensile strain between 0.26% and 2.33%. They measured a dramatic enhancement in the luminescence in the highly strained (>2%) films, suggesting that direct gap Ge was achieved. If true direct gap Ge can be realized, it has potential

applications for use as a material for lasers and high-speed modulators and photodetectors suitable for on-chip optical interconnections. In fact, designs for lasers have been proposed for direct gap Ge materials using GeSn[87] and SiGeSn[89] buffer layers as strain templates.

As stated previously, the maximum theoretical strain value for Ge films grown directly on Si is 0.34%.[71] Thus, intrinsic Ge-on-Si films will never be direct band gap materials without the use of buffer layers. However, it is possible to approach direct band gap materials by combining the effects of *n*-type doping and tensile strain in Ge-on-Si films. This method has been used to fabricate light-emitting diodes from such films.[86,90,91] In fact, Liu *et al.* recently used this approach to produce the first optically pumped Ge-on-Si laser.[92] However, the requirement for *n*-type doping limits the possibility of making an efficient electrically pumped Ge-on-Si laser.

4. Epitaxial growth of germanium on silicon

Epitaxial growth of single crystal Ge on Si substrates has been an area of interest since the early 1980's. However, early attempts at Ge-on-Si growth[93,94,95,96] showed that the 4.2% lattice mismatch between Ge and Si causes Stranski-Krastanov type growth, where the growth mechanism is initially layer-by-layer but quickly switches to island-type growth after some critical thickness that depends on temperature and strain.[97] This growth mechanism leads to unacceptably high threading dislocation densities in the

Ge films. Since then, several techniques have been explored to circumvent the Stransky-Krastanov growth to achieve high quality Ge films on Si.[98]

Developments in growth of relaxed SiGe alloy films on Si[99] prompted many efforts to reduce the lattice mismatch between Ge and Si by using a series of SiGe buffer layers.[100] In this method, the Ge content is increased in each layer until pure Ge is reached. This method "bends" the dislocations so that they remain confined to the graded layer and do not propagate to the Ge film. Using this technique, Ge-on-Si films with threading dislocation densities as low as 2×10^{6} cm^{-2} have been reported.[101] Photodiodes have been fabricated successfully from Ge produced using the graded SiGe buffer layer method.

Another method for growing Ge-on-Si that has seen recent advances involves a two-step low pressure CVD growth as outlined by Luan *et al*, typically followed by cyclic thermal annealing.[66] First, an initiation layer of 30-60 nm is grown using GeH_4 at temperatures of 320-360 °C to form a high quality interface between the Ge and Si. This is followed by higher temperature growth (>600 °C) on the newly formed Ge template. Post-growth cyclic thermal annealing at temperatures greater than 750 °C is then used to reduce the threading dislocation density. This method has been used to successfully fabricate Ge-on-Si photodetectors of various types.

One of the main reasons for the high threading dislocation density in Ge-on-Si films is the lattice mismatch between Ge and Si. This causes strain during the formation of the film, which is then relieved by threading

dislocations. One way to prevent this is to limit the strain by performing selective growth. First, the Si surface is coated with an insulator, such as SiO_2. Next, lithography is used to form a pattern for device mesas. The exposed areas of the SiO_2 are then etched down to Si, leaving small windows for the growth of the Ge-on-Si device structures. By limiting the size of these windows, the strain can be mitigated during growth. This method has been used to grow Ge-on-Si devices with great success. In fact, photodetectors grown using this method are starting to be used in commercial optical transceivers for high-speed communications.[84]

Here at ASU, our research group has developed a new method for low-pressure chemical vapor deposition (LPCVD) growth of Ge-on-Si using a custom-engineered metal-organic gaseous precursor,[102,103] as demonstrated by Weng.[104] Ge is grown directly on Si(100) substrates via thermal decomposition of digermane Ge_2H_6 and the purposely-engineered additive digermylmethane $(GeH_3)_2CH_2$. The deposition is performed in a UHV-CVD reactor at temperatures of 320-400 °C and pressures in the 10^{-4} Torr range. This is followed by rapid thermal annealing (RTA) at temperatures of 600-680 °C to reduce the threading dislocation density and improve the crystallinity of the film. This method produces high-quality Ge-on-Si films with atomically flat surfaces. Doping of the films is performed in-situ by addition of diborane B_2H_6 and trigermyl phosphine $(GeH_3)_3P$ for *p*-type and *n*-type layers, respectively, producing films with carrier concentrations into

the 10^{19} cm^{-3} range. These methods were used to synthesize the Ge films presented in this thesis.

In recent years, the success of epitaxial growth of Ge films on Si substrates has helped to renew interest in Ge as a material for semiconductor microelectronics.[1,98] The drive for faster computers with more processing power at lower cost has led to a reduction in the size of the individual components and interconnects on a microprocessor chip. This shrinkage of the transistors and metal lines between them is starting to have an effect on processor performance, so methods for circumventing these issues are at the forefront of research in microprocessors.

As the node width of transistors is reduced, mobility in the channel is decreased due to interface scattering. This adversely affects the drive current for the transistor. One way to counter this is to use materials that have higher mobility than Si. The electron and hole mobilities in Ge are 3800 and 1820 $cm^2/V.s$, respectively, while those of Si are 1900 and 500 $cm^2/V.s$.[105] Thus, Ge has twice the electron mobility and over three times the hole mobility of Si, making it an attractive candidate for next generation transistors in Si-based microprocessors.[106]

The reduction in size of the metal interconnects between devices on Si chips is also becoming a problem, as the narrow width of the metal lines increases their resistance, leading to power dissipation and increased heat generation. One of the ways currently being explored to avoid this problem is the use of optical interconnects. This involves using optical signals between

devices instead of electrical signals. This could be accomplished by using laser sources, waveguides, and high-speed modulators and detectors. However, this requires the integration of optoelectronics directly on Si. Ge-on-Si films are currently being explored as a possible material for Si-based detectors and modulators for optical interconnects.

Ge also has applications in the area of photovoltaics. The highest efficiency solar cells being produced now are multijunction solar cells. Some of these high-efficiency designs use a Ge bulk substrate to form the bottom cell.[54,55] Layers of InGaAs and InGaP are grown epitaxially on the Ge substrate to form the other junctions. In order to get the highest efficiency, these materials must be lattice matched to the substrate. This approach has produced multijunction cells with efficiencies[56] greater than 40%. However, the high cost of the Ge substrate prevents their widespread use. Replacing the bulk Ge wafer with a lower cost Ge-on-Si wafer would cut the manufacturing cost considerably, making the design more viable for large-scale implementation.

D. A new approach: Extension of optical properties of germanium via tin alloying

1. Band structure and optical properties of $Ge_{1-y}Sn_y$ alloys

Elemental Sn forms two different crystal structures. At room temperature it has a tetragonal structure, which is known as white tin (β-Sn).

At temperatures below 13.2 °C, Sn forms a diamond cubic structure, called grey tin (α-Sn). It is the latter we are concerned with, since Ge has the diamond cubic structure. The band structure of α-Sn, shown in FIG. 7, was first calculated by Groves and Paul.[107] Pure α-Sn is not a semiconductor material but rather a semimetal. Strictly speaking, it is a zero band gap material, as the highest valence band and the lowest conduction band meet at the Γ-point.

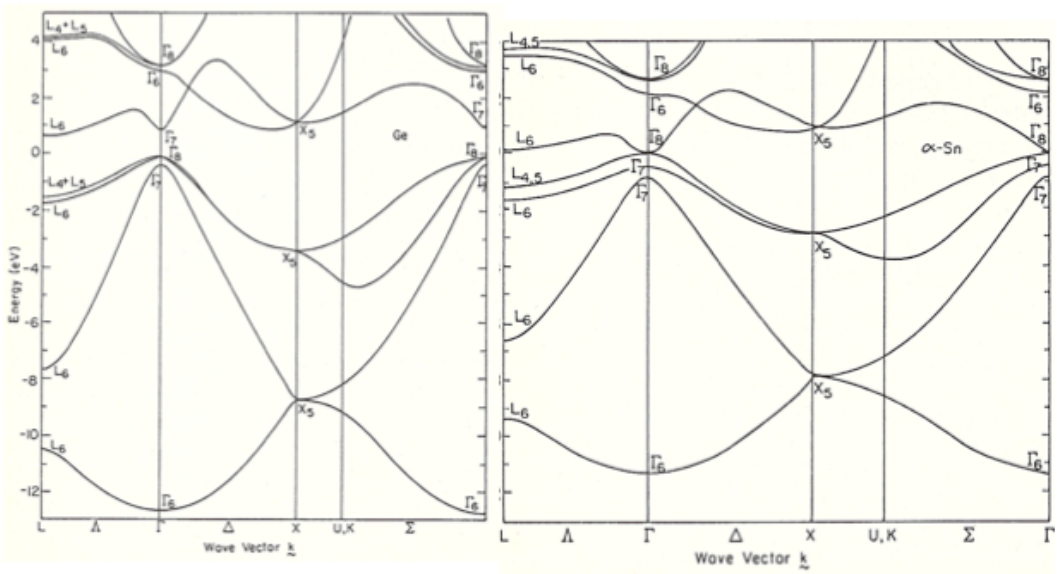

FIG. 7. Energy versus wave vector diagram showing the electronic band structure of Ge (left) and α-Sn (right). Reprinted, with permission, from *Electronic Structure and Optical Properties of Semiconductors* (Springer-Verlag Berlin Heidelberg, New York, 1988), p. 92.

In 1982, Goodman proposed that solid solutions of Ge and Sn in the diamond cubic structure could be synthesized, and that direct band gap materials with high mobilities were possible.[108] In order to understand this idea, we must examine the band structures of the two materials. Comparing

the band structure of α-Sn (FIG. 7) to that of Ge (FIG. 4), we see that in α-Sn the two degenerate heavy hole valence bands in Ge shift upward past the conduction band. The direct band gap E_0 is

$$E_0 = E(\Gamma_7) - E(\Gamma_8), \tag{5}$$

where $E(\Gamma_7)$ is the energy of the conduction band at the Γ-point and $E(\Gamma_8)$ is the energy of the heavy hole bands at the Γ-point. In Ge, this quantity is positive and has the value 0.8 eV. In α-Sn, since the bands are flipped, this quantity is negative and has value -0.4 eV, making it 1.2 eV lower than the direct gap of Ge. Thus, when α-Sn is incorporated into Ge, the direct band gap must decrease with increasing Sn concentration until it reaches zero, at which point the alloy becomes a semimetal. Up to that critical concentration, the material should be a semiconductor with a direct band gap that is tunable with Sn concentration over the range 0-0.8 eV.

The indirect band gap is also affected by the addition of Sn. The band gap of α-Sn at the L-point is 0.14 eV, while that of Ge is 0.66 eV. This means the indirect band gap must also decrease with increasing Sn concentration, but it will never reach zero. Since the difference between the gaps at the L-point in the two materials is smaller than the difference between the gaps at the Γ-point, the direct band gap should decrease faster than the indirect gap.

In general, the energies $E_i(y)$ of the optical critical points of $Ge_{1-y}Sn_y$ alloys can be well described by a quadratic polynomial of the form

$$E_i(y) = E_i^{Ge}(1-y) + E_i^{Sn}(y) - b_i y(1-y), \tag{6}$$

where E_i^{Ge} and E_i^{Sn} are the critical point energies for Ge and α-Sn, respectively. The coefficient b_i is known as the bowing parameter. This bowing parameter indicates how much the change in the critical point energies deviates from a linear interpolation between those of Ge and α-Sn. The critical point energies have been studied on thin GeSn films through optical measurements. Experimentally, the direct gap energy $E_0(y)$ of $Ge_{1-y}Sn_y$ is found to decrease faster than predicted by tight binding and pseudopotential calculations in the virtual crystal approximation.[109] The bowing parameter is also found to be relatively large compared to the bowing parameter for the direct band gap of $Ge_{1-y}Si_y$.[110] The bowing parameter for the indirect band gap of $Ge_{1-y}Sn_y$ alloys is still unknown, as methods like transmittance, reflectance, and ellipsometry are not sensitive enough to the indirect transition due to alloy broadening and the small separation between the direct and indirect gaps.

By taking into account the effects on both the direct and indirect band gaps, we start to get a picture of the band structure of GeSn alloys as a function of Sn content. For low Sn concentrations, the band structure should be Ge-like. That is, it is an indirect band gap material with the lowest gap occurring at the L-point. The difference between the minima at the L- and Γ-points decreases with increasing Sn concentration. This is very similar to the effect on the band structure of Ge when tensile strain is applied. This is represented visually in FIG. 8, which shows the difference in energies of the minima of the conduction band at the L- and Γ-points as a function of both

tensile strain and Sn incorporation. For example, we see that the relaxed alloy with just 1% Sn is equivalent to between 0.2% and 0.3% tensile strain in pure Ge.

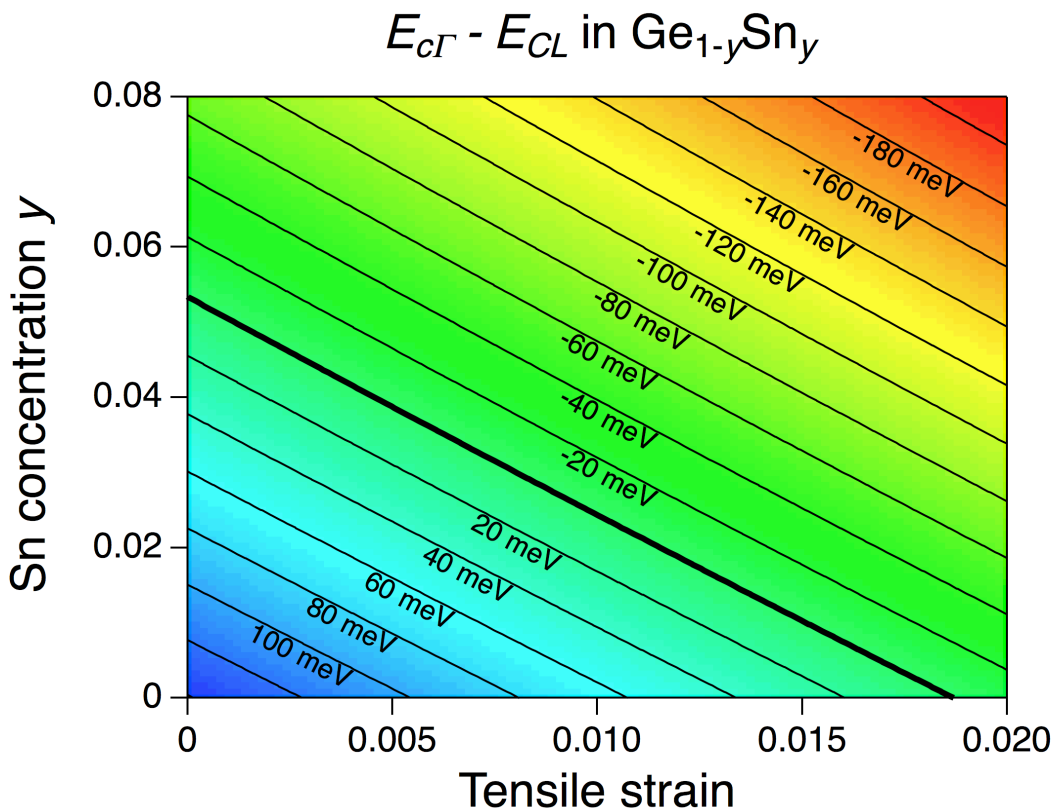

FIG. 8. Plot showing the difference in energy between the minima of the conduction band in $Ge_{1-y}Sn_y$ at the Γ- and L-points as a function of both tensile strain and Sn concentration. The thick black line represents the crossover from indirect to direct band gap material. Reprinted, with permission, from *Applied Physics Letters*, vol. 79, issue 22, p. 221912, December 2010.

Past some critical concentration y, the $Ge_{1-y}Sn_y$ alloy should become a direct gap material. This crossover has been predicted to occur around y = 0.2 by tight-binding[111] and pseudopotential[112] calculations. However, the direct band gap has been found experimentally to decrease faster than that predicted by theory. Thus, estimates based on experimental work suggest the

switch to direct band gap materials occurs between y = 0.06 and y = 0.09. For concentrations just past this critical point, the minimum at the L-point will still be close enough to that at the Γ-point that a significant concentration of electrons will populate the L-valley. Once the concentration is high enough, the electrons will essentially all be in the Γ-valley. At this point, the material should be a very efficient light absorber and emitter with a low band gap in the IR.

The maximum theoretical value for tensile strain in Ge-on-Si films that is achievable via cooling down from the melting point of Ge is 0.34%.[71] This means the tunability of the absorption and luminescence properties of Ge-on-Si films are very limited. Additionally, it is not possible to produce direct gap Ge in thick films without the use of buffer layers to increase the tensile strain. With GeSn alloys, it should be possible to produce the entire range of band gaps from 0.66 eV (pure Ge) to zero using relatively strain-free materials grown directly on Si, and direct band gap materials grown directly on Si substrates should be possible. These alloys represent an entirely new class of photonic materials that could be used for the fabrication of lasers and high-speed modulators and detectors directly on Si for integrated optical interconnects. To this end, several theoretical laser designs have been proposed based on direct gap GeSn materials.[113,114,115]

At high enough concentration y, the lowest direct band gap of $Ge_{1-y}Sn_y$ will become zero. When this happens, the material becomes a semimetal, as is the case of pure α-Sn. The transition to semimetal been predicted to occur

in $Ge_{1-y}Sn_y$ at y = 0.74 by calculations using the pseudopotential method.[112] This material will not have the interesting optical properties of the lower concentrations. Accordingly, we will focus on the semiconducting alloys.

As previously stated, much work has been done on creating highly strained Ge layers on mismatched templates. This involves growth of Ge on materials with larger lattice constants than that of Ge. Ge has a lattice parameter of 5.6575 Å, while α-Sn has a lattice parameter of 6.4912 Å.[116] Thus, $Ge_{1-y}Sn_y$ alloys should have a full range of lattice constants between these values. By growing thin layers of Ge on the $Ge_{1-y}Sn_y$ layers, it should be possible to induce enough strain for the Ge to become direct gap.

2. Growth of $Ge_{1-y}Sn_y$ alloys

In 1983, Oguz *et al.* synthesized the first microcrystalline $Ge_{1-y}Sn_y$ alloys by pulsed UV laser annealing of sputtered GeSn films.[117] By the late 1980's, several groups were producing amorphous and microcrystalline GeSn films.[118,119,120] These early growth efforts prompted theoretical research on the band structure of GeSn alloys,[111,112] which in turn drove further efforts to produce the first single-crystal GeSn material.

Many of the first successful single-crystal GeSn films were grown on novel substrates,[121,122,123] such as Ge, GaAs, and InSb, to minimize the lattice mismatch and improve epitaxy. However, even in the 1990's the need for integration with Si was recognized, and attempts were made at growth of GeSn directly on Si by vapor-phase deposition[124] and on Ge-buffered Si

substrates via solid phase[125] and molecular beam epitaxy.[126,127] The latter efforts produced high-quality thin films in which the growth conditions, band structure, and optical properties of the GeSn alloys were studied as a function of Sn concentration.[109,128] A major problem encountered during growth was the tendency of Sn to segregate toward the surface of the film. This could only be countered by lowering the growth temperature to ~100 °C, placing severe limits on the critical thicknesses of the films.

Since then, other techniques such as growth of high-Sn content GeSn on compositionally-graded GeSn buffer layers[129] have been explored for achieving direct gap GeSn. However, the most successful growth of GeSn alloys to date has occurred here at ASU. In 2001, Taraci *et al.*[130] proposed a new route to GeSn alloys via chemical vapor deposition using highly reactive Sn-containing gaseous precursors. Bauer *et al.*[131,132] took this idea further and demonstrated the growth of epitaxially stabilized GeSn films directly on Si(100) substrates using digermane Ge_2H_6 and the custom precursor deuterated stannane SnD_4. Today, our research group uses this method to produce high-quality films $Ge_{1-y}Sn_y$ films ($0 \leq y \leq 0.05$) with thicknesses up to 1 μm. Growth is performed in several custom hot-wall UHV-CVD reactors at temperatures of 350-390 °C. Doping of these films is achieved, as in the pure Ge films grown here, by addition of diborane B_2H_6 and trigermyl phosphine $(GeH_3)_3P$ for *p*-type and *n*-type layers, respectively, producing films with carrier concentrations into the 10^{19} cm^{-3} range.[133] These methods were used to synthesize the GeSn films presented in this thesis.

II. INVESTIGATION OF LIGHT ABSORPTION IN GE AND GESN FILMS GROWN ON SI

A. Fabrication and characterization of photoconductors from $Ge_{0.98}Sn_{0.02}$ films on Si

1. Introduction

The realization of high-quality micro-/optoelectronic devices based on $Ge_{1-y}Sn_y$ materials has two major requirements. First, one must be able to reproducibly grow high quality, optically active $Ge_{1-y}Sn_y$ materials. Second, processing protocols must be developed for the subsequent production of microelectronics from these materials. In this study, simple optoelectronic devices were fabricated from $Ge_{0.98}Sn_{0.02}$ films for the first time using newly developed protocols. The devices were characterized with respect to their physical, electrical, and optical properties, and the results were used to determine the feasibility of using the materials and processing protocols to fabricate high-performance optoelectronics.

2. Materials and Methods

(a) Fabrication of microelectronic devices. $Ge_{1-y}Sn_y$ films with $0.02 \leq y \leq 0.05$ and thicknesses in the range 200-600 nm were grown on high resistivity ($\rho > 1$ kΩ-cm) Si substrates using the method described in Chapter I. Most of the GeSn films were undoped, but several *p*- and *n*-type were also used. A

summary of the materials with their thicknesses and doping concentrations are presented in TABLE I. Microelectronic photoconductor structures were fabricated from the films using Si-based processing technology.

TABLE I. Sn content, thicknesses, and doping concentrations of $Ge_{1-y}Sn_y$ layers used for fabrication of photoconductors. The doping concentrations were obtained by Hall measurements.

Sample ID	Sn content (%)	Thickness (nm)	Doping concentration (cm^{-3})	Annealing
APD22A	2.0	300	undoped	RTA,
APD24A	2.0	470	undoped	RTA,
GS28A	2.0	360	undoped	none
APD58A	2.5	560	undoped	none
APD58B	2.5	480	undoped	none
T126C	2.5	405	undoped	none
T127A	3.0	510	undoped	none
T127B	3.0	490	undoped	none
T127C	3.0	440	undoped	none
T133B	5.0	200	undoped	none
PIN20B	2.0	270	$1x10^{19}$, *p*-type	none
PIN72C	2.0	325	$1x10^{19}$, *n*-type	none

A diagram of the device design is pictured in FIG. 9. The GeSn material was etched down to Si to form rectangular mesas, and ohmic contacts (formed by evaporation of Cr and Au) were placed at the ends. A layer of SiO_2 was deposited to act as surface passivation and an antireflection coating. The masks used form an array of different sized devices. The majority of the devices are 250×250 μm^2, while the rest are 500×500 μm^2, 1.25×1.25 mm^2, and 2.50×2.50 mm^2. The smaller devices are of the most interest, however, since they should have the highest response.

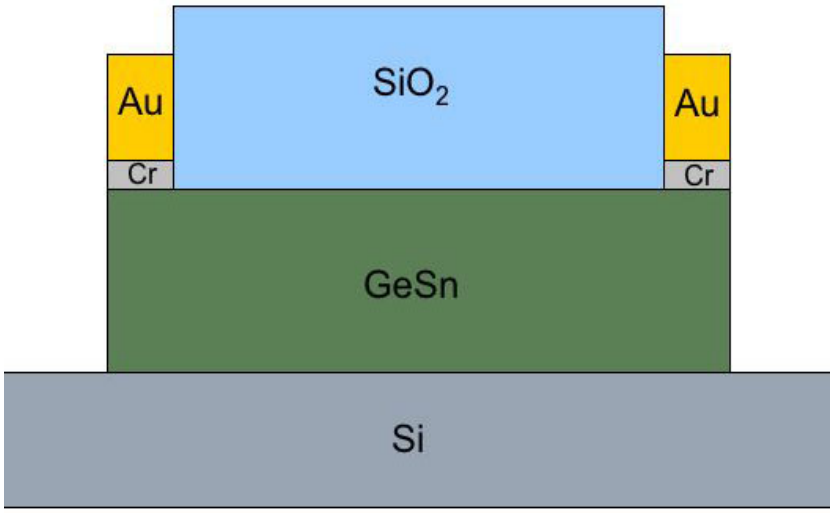

FIG. 9. Schematic of GeSn photoconductor device design.

In order to fabricate high quality microelectronics, the fabrication process must be performed in a cleanroom in order to minimize exposure to contaminants. The first step in the fabrication process was to deposit approximately 100nm of SiO_2 via plasma-enhanced chemical vapor deposition (PECVD) on top of the GeSn to passivate the surface and prevent any formation of native oxide. Prior to this, all of the samples were cleaned in an ultrasonic methanol bath, and then dried in N_2. This serves to remove any particles from the surface the samples, as well as to remove any native oxide that has formed on the surface. The SiO_2 thickness was determined by placing a small piece of bare Si with the GeSn/Si wafer in the PECVD chamber during growth. The thickness of the SiO_2 on the Si piece was measured using ellipsometry.

Once the SiO_2 deposition was complete, the wafer was spin-coated with AZ 3312 positive photoresist and exposed to UV to form the mesa pattern.

They were then immersed in AZ300MIF developer to remove the exposed photoresist. Next, the SiO_2 layer was etched away to expose the GeSn using Buffered Oxide Etch (BOE), which is a 20:1 solution of hydrofluoric acid HF and ammonium fluoride NH_4F. The mesas were formed by etching the GeSn away down to Si using reactive ion etching (RIE) in BCl_3 plasma. Once the mesas were etched, the photoresist was removed in a two-step process. First, the wafers were immersed in acetone to remove the bulk of the photoresist. Then, they were exposed to 100 W oxygen plasma for 5 minutes, removing the remaining photoresist. The etch depth was then measured using a Tencor P2 profilometer, which gives a profile of the wafer surface. The etch depth and time were used to calculate the etch rate. The etched surfaces were examined by SEM.

Next, the wafers were coated with a second layer of SiO_2 via PECVD, producing a total thickness of 520nm on top of the GeSn. This thickness was chosen to minimize reflectivity from the GeSn/Si interface. Again, the thickness was determined by measuring via ellipsometry the thickness of SiO_2 on a piece of Si. The metal contacts are produced using a "lift-off" technique. The samples were again coated with photoresist, this time with AZ 5214 negative resist. With this type of photoresist, the exposed area is stabilized, unlike positive photoresist. The metals will be deposited on top of the photoresist later, and then lifted off by removing the photoresist underneath. The negative resist is better suited for this purpose.

UV exposure using a second custom mask was used to define the contacts. The wafers were then immersed in AZ300 MIF developer to remove the unexposed photoresist to form the contact area. Again, BOE was used to etch away the SiO_2 to expose the GeSn. Immediately after, the wafers were placed in a vacuum chamber and pumped to a base pressure of 3×10^{-6} Torr. The contacts were formed by depositing 20 nm Cr followed by 200 nm Au via electron beam evaporation. Upon removal from the vacuum chamber, the wafers were immersed in acetone to dissolve the photoresist and lift off the metal, leaving the contacts. Finally, the wafers are exposed to 200 W oxygen plasma for 5 minutes to remove any remaining photoresist. The finished devices were evaluated by optical microscopy.

(b) Electrical and optical device characterization. The photoconductors were characterized with respect to their electrical and optical properties. The devices were placed on a micro-probe station for characterization. Current-voltage (I-V) curves were obtained using a Keithley 2400 source-meter. The I-V curves were used to determine whether or not ohmic contacts had been produced. The photoconductors are essentially resistors, so the I-V relationship should be linear. Ohmic contacts should not add any significant voltage drop across the device and should not have any rectifying characteristics. Thus, if ohmic contacts were produced, then the I-V curves should be linear. If there is significant contact resistance, a barrier is

produced at the metal-semiconductor interface, and a depletion region forms. This produces nonlinearity in the I-V curves.

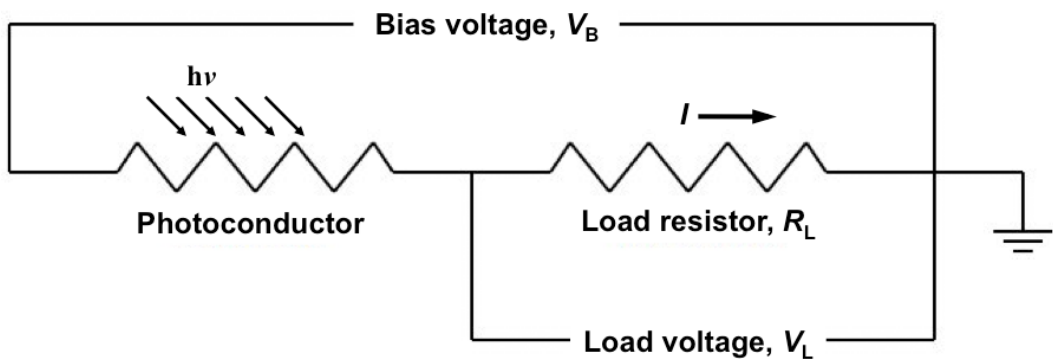

FIG. 10. Diagram of circuit used for measurement of optical response of photoconductors.

The optical response of the photoconductors was first measured at the wavelength λ=1550 nm by illuminating the device with a laser and measuring the photocurrent produced in the device. A detailed explanation of the experimental apparatus can be found in Appendix B. The measurement circuit is shown in FIG. 10. The photoconductor is placed in series with a load resistor and a fixed bias voltage is held across the series circuit. The voltage across the load resistor is measured with and without illumination by the 1550 nm laser.

Prior to illumination, the current through the circuit is I_0 and the voltage across the load resistor V_L^{dark} is given by

$$V_L^{dark} = I_0 R_L , \tag{7}$$

where R_L is the load resistance. Upon illumination, an additional current I_{ph} is produced by the conversion of photons into electron-hole pairs in the

photoconductor, so the voltage across the load resistor under illumination V_L^{illum} becomes

$$V_L^{illum} = \left(I_0 + I_{ph}\right) R_L \,. \tag{8}$$

Solving Eqs. 7 and 8 for I_0, setting them equal to each other, and solving for I_{ph} yields

$$I_{ph} = \frac{V_L^{illum} - V_L^{dark}}{R_L} = \frac{\Delta V_L}{R_L} \,, \tag{9}$$

where ΔV_L is the change in voltage across the load resistor before and after the photoconductor is illuminated by the laser. The laser light is modulated by an optical chopper, and the signal across the load resistor is measured using a lock-in amplifier.

3. Theory

The optical response of the photoconductor structures can be modeled as follows. Consider a photoconductor made up of a slab of intrinsic GeSn material with electrodes on both ends, as shown in FIG. 11. Let W be the electrode length, l the distance between the electrodes, and d the thickness of the GeSn layer. The photocurrent induced in the photoconductor due to illumination by light of frequency ν at intensity I0 can be modeled as follows.

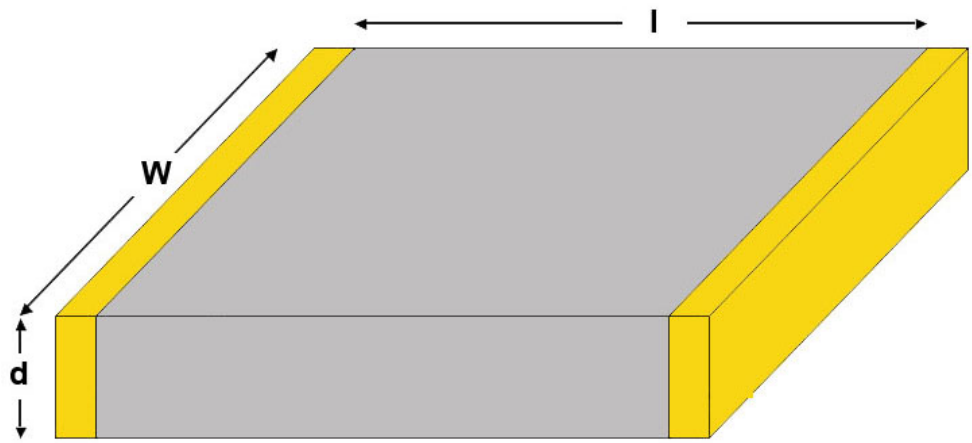

FIG. 11. Diagram of an ideal photoconductor consisting of a slab of semiconducting material with metal electrodes on either end.

Let g be the number of photons absorbed per unit area per unit time. Then the number of photons absorbed in a layer of thickness d at depth y in time dt is

$$g\,dy\,dt = \frac{\alpha I_0 (1-R)\exp(-\alpha y)}{h\nu} dy\,dt\,, \tag{10}$$

where α is the absorption coefficient for GeSn, R is the reflectivity at the GeSn surface, and h is Planck's constant.

The electron and hole concentrations, n_e and p_h respectively, of the material are

$$n_e = n_0 + n(\mathbf{r},t) \tag{11}$$

and

$$p_h = p_0 + p(\mathbf{r},t) \tag{12}$$

where n_0 and p_0 are the carrier concentrations when there is no incident light, and the second terms represent the added carriers due to photoexcitation. The photoexcited electrons and holes will diffuse and

recombine. Since the diffusion coefficients for the electrons and holes are different, a separation of charge is created. This charge separation creates a restoring electric field **E**. Assuming that the material is *p*-type, so that $n_0 \approx 0$, the equations for the electron and hole current densities, $\mathbf{j}_n$ and $\mathbf{j}_p$ are

$$\mathbf{j}_n = eD_n \nabla n + en\mu_n \mathbf{E} \tag{13}$$

and

$$\mathbf{j}_p = -eD_p \nabla p + e\left(p_0 + p\right)\mu_p \mathbf{E}, \tag{14}$$

where e is the fundamental charge, D_n and D_p are the diffusion constants for the electrons and holes, and μ_n and μ_p are the mobilities of electrons and holes, respectively.

The electrons and holes will recombine with each other with a bulk recombination lifetime τ, which is proportional to the minority carrier concentration. Since the material is assumed to be *p*-type, then the minority concentration is n. Thus, the continuity equations can be written

$$\frac{\partial n}{\partial t} = \frac{1}{e}\nabla \bullet \mathbf{j}_n - \frac{n}{\tau} + g \tag{15}$$

and

$$\frac{\partial p}{\partial t} = -\frac{1}{e}\nabla \bullet j_p - \frac{n}{\tau} + g\,. \tag{16}$$

To relate the electric field to the carrier concentrations, the equation

$$\nabla \bullet \mathbf{E} = \frac{p - n}{\varepsilon_0} \tag{17}$$

is used. Substituting the expressions for the current densities into the continuity equations and using the relation between the field and the carrier concentrations yields the two equations

$$\frac{\partial n}{\partial t} = D_n \nabla^2 n + n\mu_n \frac{p-n}{\varepsilon_0} + \mu_n \mathbf{E} \bullet \nabla n - \frac{n}{\tau} + g \tag{18}$$

and

$$\frac{\partial p}{\partial t} = D_p \nabla^2 p - \mu_n \frac{(p_0 + p)(p-n)}{\varepsilon_0} - \mu_p \mathbf{E} \bullet \nabla p - \frac{n}{\tau} + g \,. \tag{19}$$

Next, assume that $|n-p| << n, p$ so that $n \sim p$, which yields the approximations

$$\frac{\partial n}{\partial t} = D_n \nabla^2 n + \mu_n \mathbf{E} \bullet \nabla n - \frac{n}{\tau} + g \tag{20}$$

and

$$\frac{\partial n}{\partial t} = D_p \nabla^2 p - \mu_p \mathbf{E} \bullet \nabla n - \frac{n}{\tau} + g \,. \tag{21}$$

Multiplying these equations by μ_n and μ_p, respectively, and summing yields the single equation

$$\frac{\partial n}{\partial t} = D \nabla^2 n - \frac{n}{\tau} + g \,, \tag{22}$$

where

$$D = \frac{\mu_n D_p + \mu_p D_n}{\mu_n + \mu_p} \,. \tag{23}$$

Using the Einstein relations

$$\mu_n / D_n = \mu_p / D_p = e / kT \,, \tag{24}$$

D can be rewritten as

$$D = \frac{2D_n D_p}{D_n + D_p}. \tag{25}$$

The carrier concentration is assumed to be constant over the area of a single layer of thickness *dy*. While this is an approximation, the effect of the change in carrier density across the layer would be negligible. At steady state, the carrier concentration will no longer change with time and the differential equation becomes

$$\frac{\partial^2 n}{\partial y^2} - \frac{n}{L^2} = -\frac{g}{D}, \tag{26}$$

where $L = \sqrt{D\tau}$ is the diffusion length.

The boundary conditions imposed here are

$$D\left.\frac{\partial n}{\partial y}\right|_{y=0} = s_0 n(0) \tag{27}$$

and

$$D\left.\frac{\partial n}{\partial y}\right|_{y=d} = s_d n(0), \tag{28}$$

where s_0 is the recombination velocity at the GeSn/air interface and s_d is the recombination velocity at the GeSn/Si interface. Applying the boundary conditions yields the solution

$$n(y)=\frac{\alpha I_0(1-R)\tau}{2h\nu\left(\alpha^2L^2-1\right)}$$
$$\times\left[\frac{(L-s_d\tau)\left(\alpha L^2+s_0\tau\right)e^{-d/L}-(L+s_0\tau)\left(\alpha L^2-s_d\tau\right)e^{-\alpha d}}{\left(L^2+s_0s_d\tau^2\right)\sinh\left(d/L\right)+(s_0+s_d)\tau L\cosh\left(d/L\right)}e^{y/L}\right.$$
$$\left.+\frac{(L+s_d\tau)\left(\alpha L^2+s_0\tau\right)e^{d/L}-(L-s_0\tau)\left(\alpha l^2-s_d\tau\right)e^{-\alpha d}}{\left(L^2+s_0s_d\tau^2\right)\sinh\left(d/L\right)+(s_0+s_d)\tau L\cosh\left(d/L\right)}e^{-y/L}-2e^{-\alpha y}\right]. \quad (29)$$

Now that the carrier concentrations are known, the photocurrent can be calculated. The total photocurrent I_{ph} will be the sum of the photocurrent due to the electrons I_{ph}^n and the photocurrent due to the holes I_{ph}^p. If a voltage V is applied to the electrodes, then the individual photocurrents due to the electrons and holes are

$$I_{ph}^n=\int j_{ph}^n\,dx\,dy=\frac{WVe\mu_n}{l}\int_0^d n(y)\;dy \quad (30)$$

and

$$I_{ph}^p=\int j_{ph}^p\,dx\,dy=\frac{WVe\mu_p}{l}\int_0^d p(y)dy. \quad (31)$$

However, since $n(y)\approx p(y)$, the photocurrent due to the electrons can be written in terms of the photocurrent due to the holes as

$$I_{ph}^n=bI_{ph}^p, \quad (32)$$

where $b\equiv\mu_n/\mu_p$. Thus, the total photocurrent is given by

$$
\begin{aligned}
I_{ph} = & \frac{eI_0(1-R)(1+b)\tau\mu_p WV}{2h\nu\left(\alpha L^2-1\right)} \\
& \times\left[\frac{(L-s_d\tau)\left(\alpha L^2+s_0\tau\right)e^{d/L}-(L+s_0\tau)\left(\alpha L^2-s_d\tau\right)e^{-\alpha d}}{\left(L^2+s_0 s_d\tau\right)\sinh\left(d/L\right)+(s_0+s_d)\tau L\cosh\left(d/L\right)}\alpha L\left(e^{d/L}-1\right)\right. \\
& -\frac{(L+s_d\tau)\left(\alpha L^2+s_0\tau\right)e^{d/L}-(L-s_0\tau)\left(\alpha L^2-s_d\tau\right)e^{-\alpha d}}{\left(L^2+s_0 s_d\tau\right)\sinh\left(d/L\right)+(s_0+s_d)\tau L\cosh\left(d/L\right)}\alpha L\left(e^{-d/L}-1\right). \\
& \left.+2\left(e^{-\alpha d}-1\right)\right]. \qquad (33)
\end{aligned}
$$

This is a somewhat cumbersome expression to work with. Also, the recombination velocity at the GeSn/Si interface is an unknown quantity, as is the recombination velocity at the surface. However, we can write a simplified form of this by using an effective recombination lifetime τ_{eff}, given by the equation

$$
\frac{1}{\tau_{eff}} = \frac{1}{\tau} + \frac{s_0}{d} + \frac{s_d}{d}, \qquad (34)
$$

and by assuming that the carrier concentration is proportional to $e^{-\alpha y}$. Thus, the photocurrent can be written as

$$
I_{ph} = \frac{eI_0(1-R)(1+b)\tau_{eff}\mu_p WV}{h\nu l}\left(1-e^{-\alpha d}\right). \qquad (35)
$$

This expression does not expressly involve the recombination velocities, as they are included in the effective lifetime. The photocurrent is found to be proportional to the intensity of the incident light. Thus, if we make a plot of the measured photocurrent vs. intensity, the curve should be linear with a slope that is proportional to the effective lifetime. This gives us a convenient way to measure τ_{eff} experimentally.

In order to compare the photoresponse of the devices at different wavelengths, we can define the external quantum efficiency (EQE) η as the ratio of the number of electron-hole pairs created per incident photon. This quantity can be written in terms of the photocurrent I_{ph} as

$$\eta = \frac{I_{ph}/e}{P\lambda/hc} = \frac{hcI_{ph}}{eP\lambda}. \tag{36}$$

where P is the incident light power, λ is the wavelength of the light, and standard notation is used for the fundamental constants.

4. Results and Discussion

(a) Device processing and fabrication. In all cases, the fabrication process was completed with no obstacles. The SiO_2 film growth by PECVD was found to have a deposition rate of 6 nm/min. The first lithography step was performed successfully on all of the wafers. The development time was found to be in the range 50-70 s. The patterned wafers were inspected by optical microscopy for sharpness of the features. If the smallest features in the pattern were found to be well defined, then the lithography was acceptable. This was the case for all the wafers. The SiO_2 was etched successfully using BOE and the etch rates were found to be in the range 40-60 nm/min.

The GeSn layers were etched using RIE and the etch rates were found to be 20-40 nm/min. The etched surfaces were examined by SEM to determine the quality of the mesa definition and surface roughness. A representative image of an etched $Ge_{0.98}Sn_{0.02}$ film is shown in FIG. 12. The sidewalls of the mesas were found to be only 5° from vertical, and the features were very well defined. AFM measurements on a few samples found that the surface roughness in the etched areas was only a few nm.

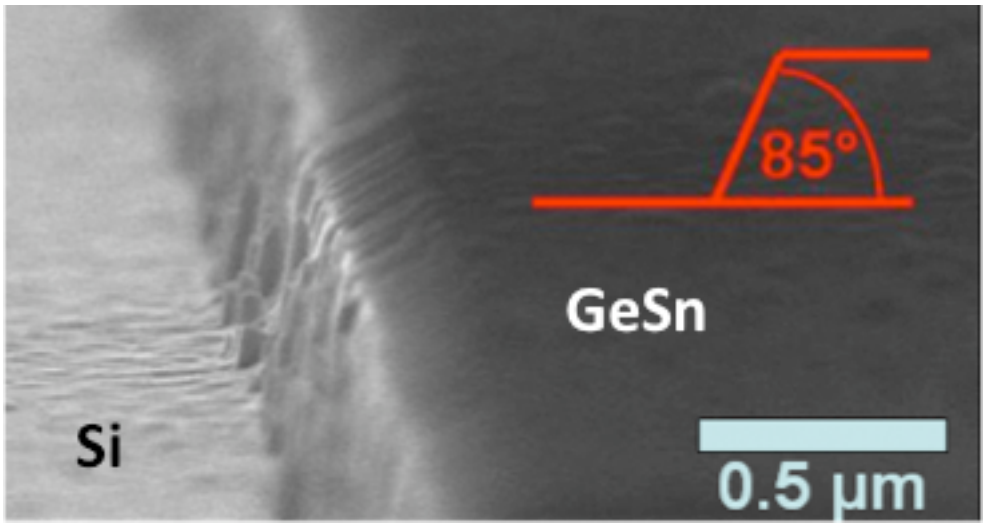

FIG. 12. SEM image of a GeSn film on Si that has been etched by RIE. The GeSn has been etched down to expose the Si on the left, while the GeSn remains intact on the right. The sidewalls were found to have an angle of 85°.

Exposure to the oxygen plasma was found to fully remove the photoresist from the wafer, leaving a clean template for the next processing step. The second SiO_2 deposition step was found to proceed just as the first. Again, the deposition rate was found to be in the 6 nm/min range. The second lithography step using image reversal was found to be successful. The

development time was found to be in the range 50-70 s, and the wafers were inspected with optical microscopy to ensure the sharpness of the pattern. The SiO_2 in the contact areas was etched away using BOE again, and the etch rates were found to be the same as previously measured. Metal deposition was performed via electron beam evaporation of Cr and Au. The Cr deposition rate was around 6 nm/min, while the Au deposition rate was slightly higher at 9 nm/min. The metal was lifted off in acetone, leaving well-defined contacts. An optical image of completed photoconductors fabricated from a $Ge_{0.98}Sn_{0.02}$ film is shown in FIG. 13.

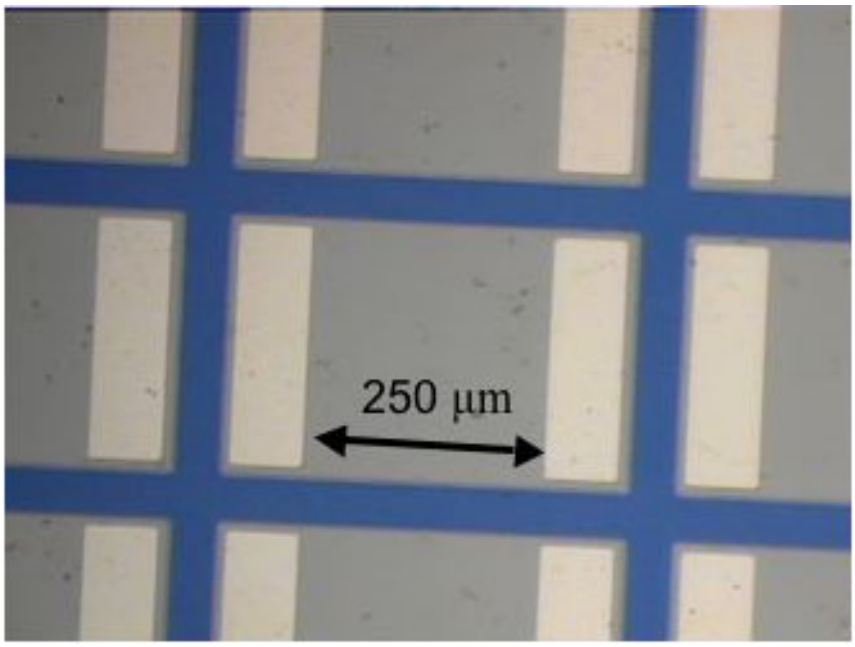

FIG. 13. Optical image of fully fabricated 250×250 μm² $Ge_{0.98}Sn_{0.02}$ photoconductors.

(b) Electrical and optical properties of devices. The fabricated photoconductors were characterized with respect to their current-voltage characteristics as well as their response to illumination by 1550 nm laser.

The current-voltage curves were found to be linear for all of the devices fabricated from undoped and *p*-type GeSn layers. The I-V curve shown in FIG. 14 was taken from a 250×250 μm² photoconductor made from an undoped $Ge_{0.98}Sn_{0.02}$ film. The linear I-V relationship shows that the contacts are indeed ohmic, as desired.

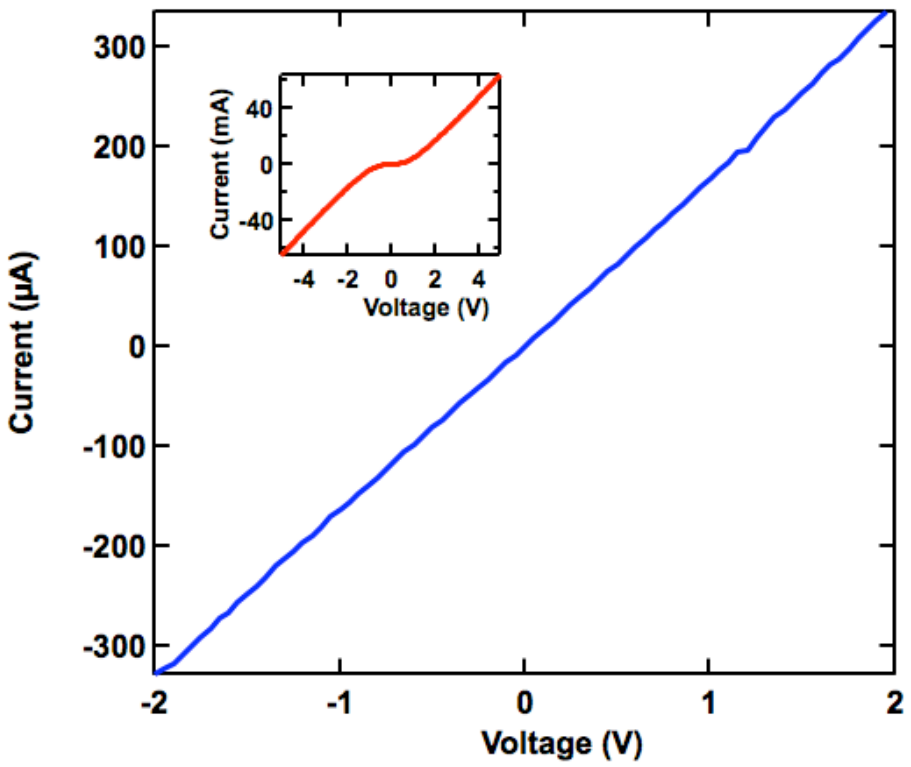

FIG. 14. I-V curve for a 250×250 μm² photoconductor made from a an undoped $Ge_{0.98}Sn_{0,02}$ layer. Inset shows I-V curve obtained from *n*-type film with same Sn content.

In the case of the *n*-type photoconductors, the I-V curves were somewhat nonlinear, as shown in FIG. 14 (inset). This indicates the formation of a barrier at the metal-semiconductor interface. The resulting behavior can be explained by the equivalent circuit pictured in FIG. 15. Essentially, there are two Schottky diodes with opposing polarity connected

by a resistor made up of the bulk of the GeSn layer. There is rectification in both directions, but at large voltages one is always reverse biased, so the current is limited. This produces the symmetric, nonlinear I-V curve pictured in FIG. 14.

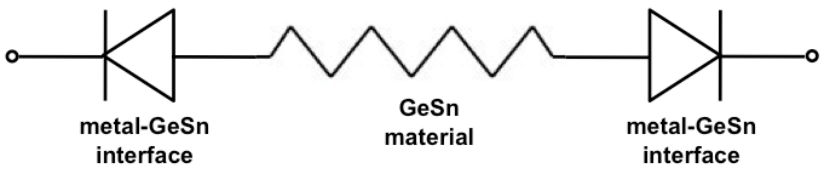

FIG. 15. Diagram showing equivalent circuit for *n*-type $Ge_{0.98}Sn_{0.02}$ photoconductors.

The formation of ohmic contacts on semiconducting materials can be very difficult. Accordingly, much effort has been put into trying to understand the physics of the metal-semiconductor interface.[134] In the ideal case, without surface states or other anomalies, the Schottky barrier height (SBH) ϕ_B between a metal with work function ϕ_M and a semiconductor with electron affinity χ_S is given by[135]

$$\phi_B = \phi_M - \chi_S \,. \tag{37}$$

Thus, for a given semiconductor, the SBH should depend very strongly on the metal work function.

In practice, the barrier height is not so straightforward. It tends to depend on the preparation of the semiconductor surface prior to metal deposition, which implies that surface states play a major role in the barrier height. In some cases, the effect of the surface states is so strong that it fixes,

or "pins", the Fermi level at the interface and the SBH becomes nearly independent of the type of metal. This type of behavior is called Fermi level pinning. This effect has been studied extensively in Ge, and it has been determined that Fermi level pinning causes most *n*-Ge/metal contacts to form Schottky barriers, while *p*-Ge/metal contacts tend to be Ohmic.[136,137,138]

In the photoconductors studied here, ohmic contacts were produced in every case except for the GeSn layer with *n*-type doping. As stated previously, the undoped GeSn films are found to be *p*-type with background concentrations in the range 10^{16}-10^{17} cm^{-3}. These results are consistent with those found for pure Ge, which suggests that the Fermi level pinning effect is present in the GeSn films as well. This is not surprising, as GeSn films with these modest Sn concentrations still have Ge-like band structure.

TABLE II. Summary of results of measurements of photocurrents on photoconductors fabricated from undoped layers.

Sample ID	Sn content (%)	Thickness (nm)	Photocurrent, I_{ph} (A)	EQE, V_B=1 V
APD22A	2.0	300	2.4×10^{-5}	3.8×10^{-3}
APD24A	2.0	470	1.5×10^{-5}	2.4×10^{-3}
GS28A	2.0	360	2.7×10^{-6}	4.3×10^{-4}
APD58A	2.5	560	7.9×10^{-7}	1.3×10^{-4}
APD58B	2.5	480	1.2×10^{-7}	1.9×10^{-4}
T126C	2.5	405	6.3×10^{-7}	1.0×10^{-4}
T127A	3.0	510	7.6×10^{-7}	1.2×10^{-4}
T127B	3.0	490	7.0×10^{-7}	1.1×10^{-4}
T127C	3.0	440	6.5×10^{-7}	1.0×10^{-4}
T133B	5.0	200	4.1×10^{-7}	6.5×10^{-5}

The photoresponse of the devices was measured at 1550 nm for a range of bias voltages of 0.1-10 V. All of the devices were found to have measureable response under illumination, but the magnitude of the photocurrent varied over a wide range, as shown in TABLE II. It was found that the photoconductors produced from layers that were not subjected to RTA treatments had photocurrents that were approximately 1-2 orders of magnitude lower than those that had been annealed. This indicates that the annealing process does, in fact, improve the crystallinity in the layer. Most likely, the density of threading dislocations is reduced, thereby increasing the effective lifetime, which in turn enhances the photocurrent and EQE.

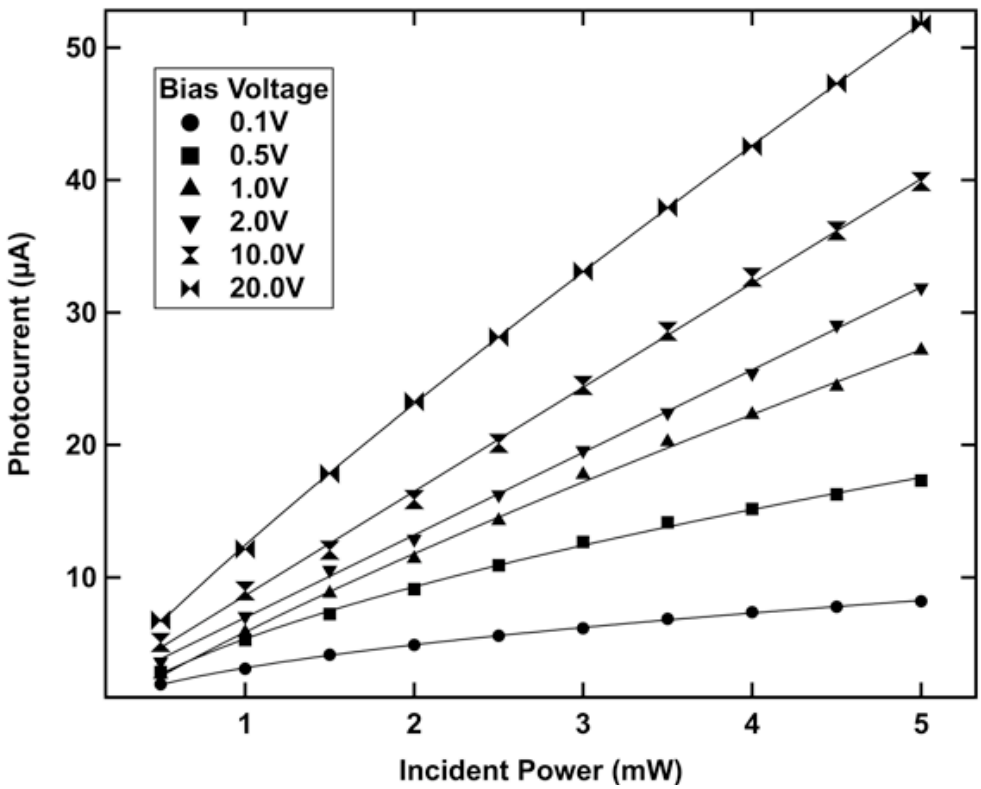

FIG. 16. Plot of photocurrents vs. incident light power obtained from devices fabricated from an undoped $Ge_{0.98}Sn_{0.02}$ film for a variety of bias voltages.

The photocurrents obtained from the sample APD24A are plotted in. For lower values of the bias voltage, the curve is non linear. As the bias voltage is increased, the curve becomes linear. From Eq. 35, it seems that it should be linear for every bias voltage, but this is not the case. This can be understood by looking at the measurement circuit diagram in FIG. 10. The bias across the series circuit V_B is held constant, not the voltage across the device. As the incident power is increased, the current produced in the device and, thus, the circuit increases. This leads to an increase in voltage across the load resistor V_L. Since V_B is held constant, the voltage V across the device must decrease. At higher values of V_B, the dark current is higher, so the extra voltage drop becomes insignificant. Thus, we only see this effect at lower bias voltages.

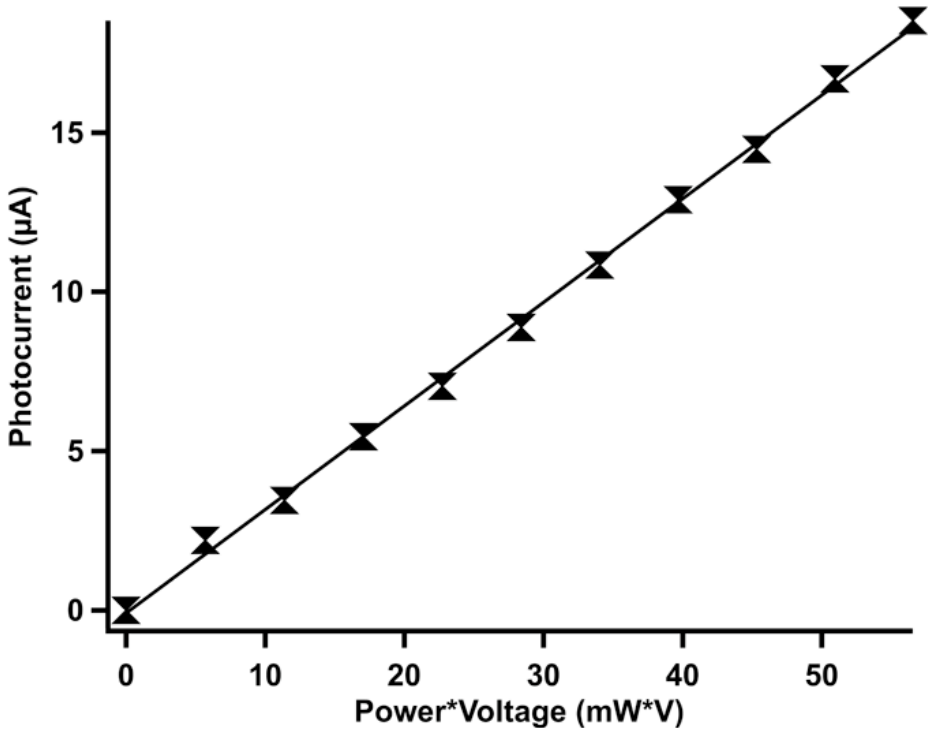

FIG. 17. Plot of photocurrent vs. product of incident light power and voltage across device obtained from a 259×250 μm² device fabricated from an undoped $Ge_{0.98}Sn_{0.02}$ film.

For a given bias voltage, we can easily obtain the voltage across the device for each value of photocurrent. We can then plot the photocurrent vs. the product of the incident power and the voltage, as shown in FIG. 17. This produces the linear result, as expected, and we can obtain the effective lifetime from the slope. The effective lifetime was found to be 5 ns in the films with the highest response. This is relatively low compared to the bulk recombination lifetime in Ge, but the thin layer is subject to the effects of surface recombination, as discussed in our theoretical model. In addition, the GeSn layer most likely has a larger defect density relative to bulk Ge, as it is grown on a mismatched template.

Photocurrent measurements on the doped photoconductors did not yield promising results. The photocurrents in the *p*-type samples were found to be on the order of 10^{-8} A, while the *n*-type samples showed no measureable change in current with illumination. In the case of the *n*-type samples, this is not surprising, as the lack of Ohmic contacts severely reduces the efficiency. The addition of the Schottky barrier at each contact makes it very difficult for the generated charge carriers to be captured at the contacts. This leads to very low efficiency. Additionally, the high carrier concentrations cause free carrier absorption, which does not contribute to the photocurrent. This is why the photocurrents in the *p*-type photoconductors are so low, despite the fact that Ohmic contacts were achieved. Additionally, the low resistivity of the GeSn material leads to high dark currents with degrade the signal to noise ratio.

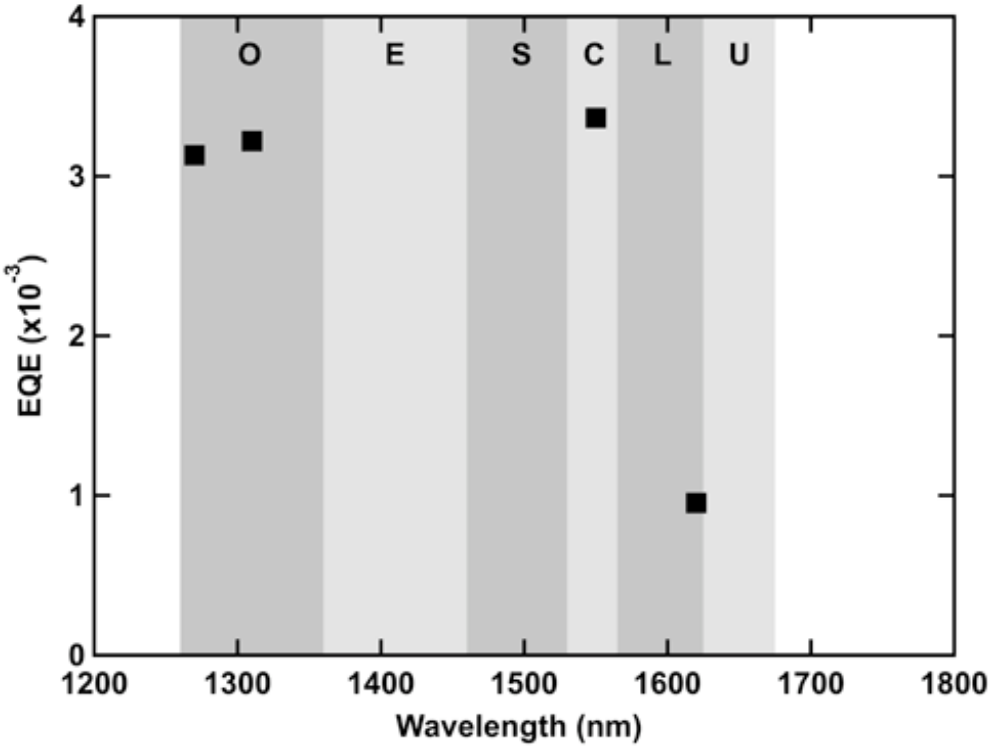

FIG. 18. Plot of external quantum efficiency vs. wavelength of incident light measured on 250×250 μm^2 photoconductor fabricated from APD24A. The gray areas indicate the ranges of the telecom bands.

The sample that showed the highest response was the $Ge_{0.98}Sn_{0.02}$ undoped film, APD24A. Accordingly, further experiments and analysis were performed on these photoconductors. Additional laser diodes with wavelengths 1270, 1300, and 1620 nm were used to illuminate the devices, and the EQE was determined for each wavelength. The results are shown in the plot in FIG. 18. The quantum efficiency is highest for wavelengths below 1600 nm and then decreases at the 1620 nm wavelength. Still, there is a significant response even at the longest wavelength. In fact, we see that there is a significant response in the bands used for telecommunications,

suggesting that a high-performance detector covering all telecom bands could be realized using GeSn materials.

These results can be understood by examining the absorption coefficient of the $Ge_{0.98}Sn_{0.02}$ alloy, as pictured in FIG. 19. The addition of just 2% Sn shifts the absorption edge lower energies relative to bulk Ge due to the lowering of the direct band gap E_0. Additionally, the edge is broadened compared to bulk Ge due to alloying. The dotted line in FIG. 19 indicates the wavelength 1550 nm. At this wavelength we see almost an order of magnitude increase in the absorption coefficient due to the addition of Sn.

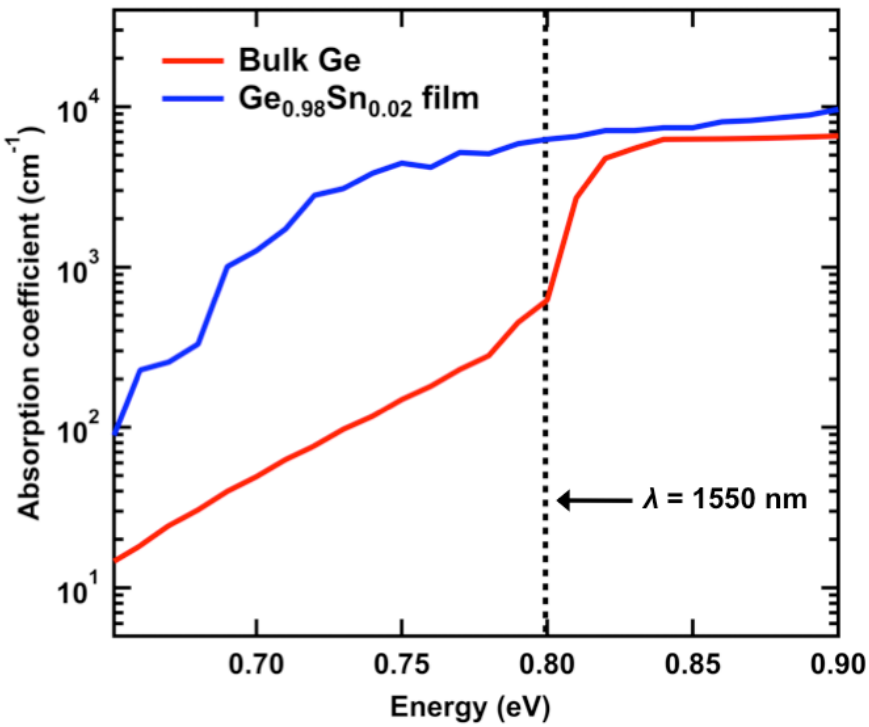

FIG. 19. Absorption coefficients of bulk Ge and $Ge_{0.98}Sn_{0.02}$ as measured by spectroscopic ellipsometry. The dotted line indicates the wavelength 1550 nm, at which there is a significant enhancement in the absorption coefficient of the GeSn film relative to that of bulk Ge. Ellipsometry measurements courtesy of V. R. D'Costa.

5. Conclusions

Microelectronic photoconductor devices were fabricated from $Ge_{1-y}Sn_y$ films for the first time. The fabrication processes were found to yield high quality device structures, and Ohmic contacts were achieved in all undoped and *p*-type devices. Ohmic contacts were not produced on *n*-type devices, most likely due to Fermi level pinning at the GeSn/metal interface. The devices fabricated from undoped films were found to exhibit measureable response to illumination by incident light at 1550 nm. The devices produced from films that underwent RTA treatments were found to have much higher response than those from films that were unannealed. The effective recombination lifetime in the annealed films was found to be in the nanosecond range. The spectral dependence of the optical response of the photoconductors made from $Ge_{0.98}Sn_{0.02}$ films showed that the photoresponse was significant even at 1620 nm, suggesting the material's potential for extended range, high performance detectors.

B. Fabrication and characterization of *p-i-n* heterostructure photodiodes from $Ge_{1-y}Sn_y$ films on Si

1. Introduction

The successful fabrication of simple photoconductor structures prompted efforts to produce high performance *p-i-n* type detectors based on $Ge_{1-y}Sn_y$ materials. The device processing protocols developed for the

photoconductors were employed in the fabrication of $Ge_{1-y}Sn_y$/Si *p-i-n* heterostructure photodiodes. The detectors were characterized with respect to their electrical and optical properties and compared to those of similar diodes made from pure Ge films.

2. Materials and Methods

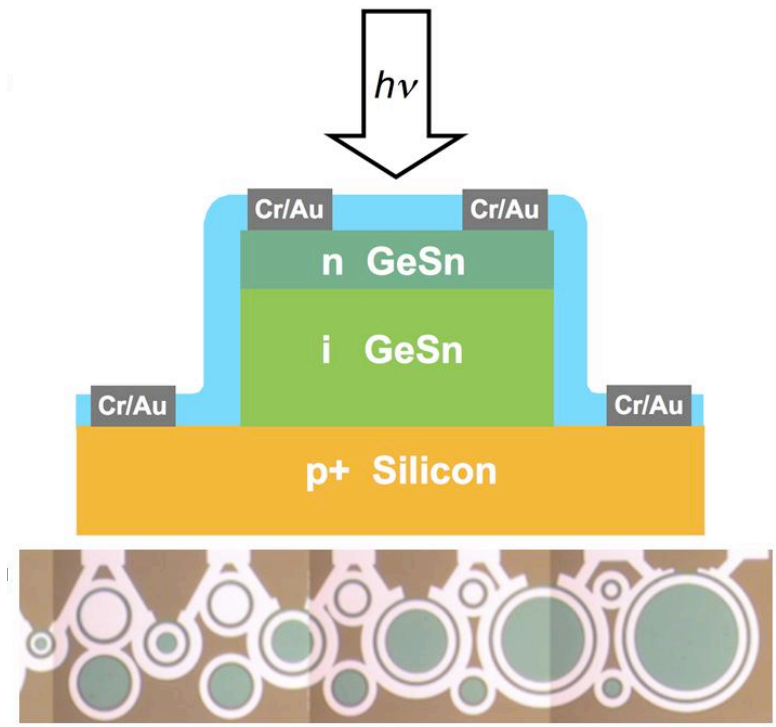

FIG. 20. Schematic cross-sectional view (top) and plan view (bottom) of the GeSn/Si *n-i-p* heterostructure diode design.

The devices presented in this study are heterostructure type diodes utilizing a highly doped Si substrate for one side of the junction, as shown in the example in FIG. 20 (top). An undoped Ge or GeSn layer with thickness up to 1 μm is deposited, followed by a highly doped (~10^{19} cm^{-3}) capping layer

of opposite type from the substrate with thickness ~100 nm. Samples grown on *p*-type wafers with *n*-type Ge/GeSn capping layers are referred to *n-i-p* devices, while those grown on *n*-type wafers with *p*-type Ge/GeSn capping layers are referred to as *p-i-n* devices for the rest of this section. Circular mesas are formed and Ohmic contacts are placed in ring geometry, as shown in FIG. 20 (bottom). The center of the ring serves as the detection window, and it has an antireflective coating made of SiO_2.

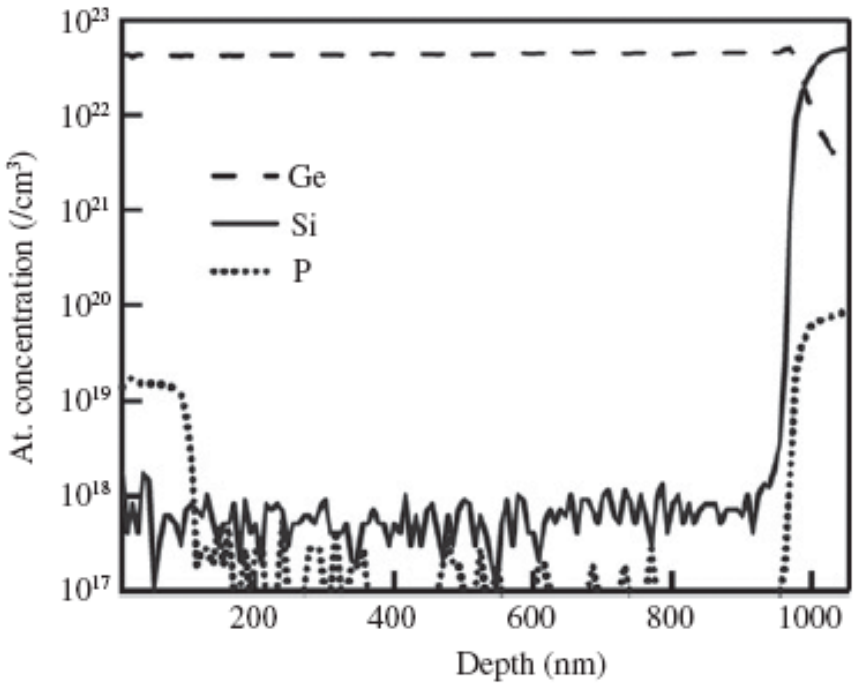

FIG. 21. SIMS profile obtained from a pure Ge sample (Ge172, total thickness 980 nm) showing the atomic concentrations of Ge, Si, and P in the sample as a function of depth. The high amount of P detected in the Si substrate is an artifact of the system and can be ignored.

The pure Ge growth was performed using the LPCVD method utilizing Ge_2H_6 and $(GeH_3)_2CH_2$, while GeSn growth was performed using the CVD method utilizing Ge_2H_6 and SnD_4. Both of these growth methods are outlined in Chapter I. Doping is performed *in situ* in both growth methods by addition

of the gaseous precursors B_2H_6 and $(GeH_3)_3P$ for *p*- and *n*-type layers, respectively. Doping concentrations in the layers were measured by IR spectroscopic ellipsometry and verified by SIMS. A typical profile of the doping obtained via SIMS from a pure Ge sample with total thickness 980 nm is presented in FIG. 21.

TABLE III. List of substrate resistivities, Sn concentrations, layer thicknesses, and doping concentrations for heterostructures that were processed into devices.

Sample ID	Substrate resistivity, type (Ω-cm)	Sn content (%)	Intrinsic layer thickness (nm)	Capping layer thickness (nm)	Capping layer doping concentration (cm^{-3})
Ge116	0.003, *n*-type	0.0	350	150	2×10^{19}, *p*-type
Ge172	0.010, *p*-type	0.0	890	90	2×10^{19}, *n*-type
GeSn20C	0.003, *n*-type	0.2	450	150	1×10^{19}, *p*-type
GSPI1208C	0.003, *n*-type	1.0	440	60	1×10^{19}, *p*-type
GSN01B	0.010, *p*-type	2.2	355	65	1×10^{20}, *n*-type
GSPI22B	0.003, *n*-type	3.0	315	145	1×10^{19}, *p*-type

The samples that were used to fabricate photodiodes are presented with their parameters in TABLE III. The successfully fabricated photodiodes were characterized with respect to their electrical properties by measuring their current-voltage (I-V) dependence. This was done at room temperature using the apparatus described in Appendix B. I-V curves were also obtained at temperatures up to 80 °C using a micro-probe station with a temperature controlled chuck. The optical response of the photodiodes in the near-IR was also measured using the apparatus described in Appendix B. The external quantum efficiency (EQE) of the photodiodes was measured in the range 1-

1.8 μm. Additional I-V measurements were taken while the photodiodes were subject to illumination by a 1300 nm laser, and the EQE dependence on reverse bias was measured.

3. Theory

For an ideal *p-n* diode, the dependence of the dark current I on the applied voltage V at temperature T is given by the Shockley equation[139]

$$I = I_s\left[\exp\left(\frac{qV}{kT}\right)-1\right], \tag{38}$$

where I_s is the saturation current. At low voltages, the exponential term is small, so we can write

$$I \approx I_s \exp\left(\frac{qV}{kT}\right). \tag{39}$$

Experimentally, it is found that the behavior at low voltages is actually

$$I \approx I_s \exp\left(\frac{qV}{nkT}\right), \tag{40}$$

where the ideality factor n is a number between 1 and 2. The ideality factor can be determined by measuring the slope of a logarithmic plot of the current versus voltage in the region where the curve is linear.

In an ideal diode, the current is due only to diffusion of carriers across the junction. For real diodes, the current can be modeled as the sum of the two components. One component is due to diffusion, and the other

component is due to recombination-generation in the space charge region. Thus, we can write[139]

$$I = I_s^D \exp\left(\frac{qV}{kT}\right) + I_s^{RG} \exp\left(\frac{qV}{2kT}\right), \tag{41}$$

where T is the temperature and I_s^D and I_s^{RG} are the saturation currents due to diffusion and recombination-generation, respectively. From this, we see that if the current is dominated by diffusion, the ideality factor n should be 1. If the current is mainly due to recombination-generation, then n will be 2.

From the Shockley equation, we see that at large reverse voltage, the current becomes saturated at I_s. Further insight into the origin of the dark currents can be gleaned by examining the temperature dependence of I_s. The current should have an Arrhenius dependence on temperature

$$I_s \propto \exp\left(\frac{E_a}{kT}\right), \tag{42}$$

where E_a is the activation energy. Thus, if we make a logarithmic plot of the saturation current versus $1/kT$, we can determine E_a. For diffusion currents[139]

$$I_s^D \propto n_i^2 \propto \exp\left(\frac{E_g}{kT}\right), \tag{43}$$

where n_i is the intrinsic carrier concentration in the semiconductor. For current due to recombination-generation, we have[139]

$$I_s^{RG} \propto n_i \propto \exp\left(\frac{E_g}{2kT}\right). \tag{44}$$

Thus, if E_a is close to E_g, then the current is dominated by diffusion of carriers across the junction. If E_a is close to $E_g/2$, it is dominated by recombination-generation in the space charge region.

The EQE η of the *p-i-n* diodes can be modeled in a relatively simple way. Let d_{top} and d_{int} are the thicknesses of the top doped layer and the intrinsic layer, respectively. In general, the fraction of light absorbed in a material f_{abs} is related to its transmittance T and reflectance R by

$$f_{abs} = 1 - T - R. \tag{45}$$

A full, rigorous treatment would take into account all reflections produced by the multilayer structure. However, we can approximate by only taking into account one reflection from the back surface. Thus, we can write

$$\eta = f_{int}\eta_C\left(1 - T_+ - R_+\right) + f_{back}\eta_C T_+ R_{back}(1 - T_- - R_-), \tag{46}$$

where η_c is the collection efficiency, T_+ (R_+) is the transmittance (reflectance) of the entire oxide/Ge stack on Si under illumination from the top surface, R_{back} is the reflectance at the back surface of the Si wafer, and T_- (R_-) is the transmittance (reflectance) of the oxide/Ge stack for illumination by the light reflected from the back surface.

For light incident from the top layer side, assuming the same absorption α, the fraction of light absorbed by the top layer f_{top} is

$$f_{top} = \frac{1 - \exp\left(-\alpha d_{top}\right)}{1 - \exp\left[-\alpha\left(d_{top} + d_{\text{int}}\right)\right]}. \tag{47}$$

Thus, the fraction of light absorbed by the intrinsic layer f_{int} is

$$\begin{aligned} f_{int} &= 1 - f_{top} = 1 - \frac{1-\exp\left(-\alpha d_{top}\right)}{1-\exp\left[-\alpha\left(d_{top}+d_{int}\right)\right]} \\ &= \frac{\exp\left(-\alpha d_{top}\right)-\exp\left[-\alpha\left(d_{top}+d_{int}\right)\right]}{1-\exp\left[-\alpha\left(d_{top}+d_{int}\right)\right]} \\ &= \frac{1-\exp\left(-\alpha d_{int}\right)}{\exp\left(\alpha d_{top}\right)-\exp\left(-\alpha d_{int}\right)}. \end{aligned} \tag{48}$$

For illumination from the intrinsic layer side, the fraction of light absorbed by the intrinsic layer is

$$\begin{aligned} f_{back} &= 1 - \frac{1-\exp\left(-\alpha d_{int}\right)}{1-\exp\left[-\alpha\left(d_{top}+d_{int}\right)\right]} \\ &= \frac{\exp\left(\alpha d_{top}\right)-\exp\left(\alpha d_{top}\right)\exp\left(-\alpha d_{int}\right)}{\exp\left(\alpha d_{top}\right)-\exp\left(-\alpha d_{int}\right)} \\ &= \exp\left(\alpha d_{top}\right) f_{int}. \end{aligned} \tag{49}$$

Thus, we can write the EQE as

$$\eta = f_{int}\eta_C\left(1-T_+-R_+\right)+\exp\left(\alpha d_{top}\right) f_{int}\eta_C T_+ R_{back}(1-T_- - R_-). \tag{50}$$

The values for transmittance and reflectance are calculated using standard transfer-matrix techniques and tabulated optical constants for SiO_2, Ge, and Si. Notice that Eq. 50 treats the light traveling through the Ge device structure as fully coherent, but neglects the coherence between the light traveling toward the back surface of the Si wafer and the light reflected at this surface. The use of the factor f_{int} in Eq. 50 is an approximation. A more rigorous treatment within the transfer-matrix formalism is discussed by Prentice.[140] The assumption that only light absorbed in the intrinsic layer

contributes to the photocurrent slightly underestimates the quantum efficiency, since light absorbed in the top layer will also contribute as long as the electron–hole pairs are generated at distances from the intrinsic layer which are comparable to the minority carrier diffusion length.

The expression for the EQE in Eq. 50 depends on the absorption coefficient of the epitaxial layers grown on the Si. The absorption coefficients of Ge and $Ge_{0.98}Sn_{0.02}$ were measured previously by spectroscopic ellipsometry, so we can use this data to model the response in devices made from these films. For other Sn concentrations, we can derive a theoretical expression. We express the absorption in Ge-like materials as

$$\alpha(E) = \alpha^{E_0}(E) + \alpha^{\text{high}}(E). \tag{51}$$

The first term accounts for the absorption related to the lowest direct band gap E_0, and the second term incorporates above-band gap transitions. Indirect transitions below the direct gap are not included. The E_0 transitions involve the heavy- and light-hole valence bands and the *s*-like conduction band near the $\boldsymbol{k} = 0$ (Γ) point in the Brillouin zone. The dispersion of all these bands is assumed to be parabolic. We express the E_0 absorption as

$$\alpha^{E_0}(E) = \alpha_0^{chh}(E)\left[f_{hh}(E) - f_c(E)\right] + \alpha_0^{clh}(E)\left[f_{lh}(E) - f_c(E)\right]. \tag{52}$$

Here the superscripts *chh* (*clh*) refer to transitions between the heavy hole band *hh* (light hole band *lh*) and the conduction band *c*. The quantity $\alpha_0^{cv}(E)$ with $v = hh$ or lh is the absorption coefficient for an empty conduction band and a full valence band. The Fermi functions $f_v(E)$ and $f_c(E)$ give the

occupation probability for the valence and conduction band states separated by an energy E. We express the absorption in terms of the real (ε_1) and imaginary (ε_2) parts of the empty-band dielectric function as

$\alpha_0^{cv}(E) = E\,\varepsilon_2^{cv}(E) \Big/ \left[\hbar c\sqrt{\varepsilon_1(E)}\right]$, where c is the speed of light and $\hbar = h/(2\pi)$.

Since the value of ε_1 changes very little at the E_0 gap, we simply use for the real part an expression of the form $\varepsilon_1(E)$ = 11.03-11.88/(E-2.62), with E in eV, which has been fit to the experimental real part of the dielectric function in pure Ge. The compositional and strain dependence of ε_1 are neglected. For each of the v = hh heavy- and v = lh light-hole components, the imaginary part of the dielectric function is written as[141]

$$\varepsilon_2^{cv}(E) = \varepsilon_x^{cv}(E) + \varepsilon_f^{cv}(E) S^{cv}(E) \tag{53}$$

where ε_x^{cv} the below-band gap excitonic contribution given by[32]

$$\varepsilon_2^{cv}(E) = \frac{16\pi |P|^2 e^4 \mu_{cv}^2 R_{cv}}{E^2 \hbar^2 m^2 \varepsilon_0} \sum_{n=1}^{\infty} \frac{1}{n^3} \delta(E - E_n) \tag{54}$$

where P is the momentum matrix element, e and m the free electron charge and mass, μ_{cv} the reduced electron-hole mass, ε_0 the static dielectric constant, and the Rydberg is defined as $R_{cv} = \mu_{cv} e^4 / (2\hbar^2 \varepsilon_0^2)$. With this definition the excitonic energy levels can be written as $E_n = E_{0v} - R_{cv}/n^2$, where E_{0v} is the light-hole (heavy-hole) direct band gap for v = lh (v = hh). The second term in Eq. 53 is given by the dielectric function ε_f^{cv} for free, uncorrelated electron-

hole pairs multiplied by the Sommerfeld enhancement factor S^{cv}. These quantities are given by[32]

$$\varepsilon_f(E) = \frac{4\sqrt{2}e^2P^2\mu_{cv}^{3/2}}{3m^2\hbar E^2}\left(E - E_{0v}\right)^{1/2}\Theta\left(E - E_{0v}\right) \tag{55}$$

and

$$S^{cv}(E) = \frac{\tau_{cv}e^{\tau_{cv}}}{\sinh\tau_{cv}}; \quad \tau_{cv} = \pi\left|\frac{R_{cv}}{E - E_{0v}}\right|^{1/2} \tag{56}$$

where $\Theta(x)$ is the unit step function.

The needed $E_{0v} = E_{0lh}$ light-hole direct gap and and $E_{0v} = E_{0hh}$ heavy-hole direct band gap are calculated as function of the strain using standard deformation potential theory. The corresponding expressions are:

$$\begin{aligned} E_{0lh} &= E_0 + \frac{\Delta_0}{2} + \delta E_0 - \frac{1}{4}\delta E_{001} - \frac{1}{2}\sqrt{\frac{9}{4}\left(\delta E_{001}\right)^2 + \Delta_0^2 + \Delta_0\delta E_{001}} \\ E_{0hh} &= E_0 + \delta E_0 + \frac{1}{2}\delta E_{001} \end{aligned} \tag{57}$$

Here Δ_0 is the spin-orbit splitting at the Γ-point of the Brillouin zone and

$$\begin{aligned} \delta E_0 &= 2a_h\left(1 - C_{12}/C_{11}\right)\varepsilon_{\parallel} \\ \delta E_{001} &= -2b\left(2C_{12}/C_{11} - 1\right)\varepsilon_{\parallel} \end{aligned}, \tag{58}$$

where $\varepsilon_{\parallel} = \left(a - a_0\right)/a_0$, C_{11} and C_{12} are elastic constants, a_h the hydrostatic E_0 gap deformation potential, and b the shear deformation potential.

For pure Ge, all parameters needed for the evaluation of Eqs. 54-59 are independently measured (including the matrix element P, which obtains from the experimental effective masses using **k·p** theory), and the values we use are summarized in TABLE IV. For $Ge_{1-y}Sn_y$ alloys the band structure

parameters are interpolated in the spirit of **k·p** theory as discussed in Ref. 141. The deformation potentials and elastic constant ratio C_{12}/C_{11} are linearly interpolated with those of α-Sn. Of course, given the small amounts of Sn in this work, the interpolated values are virtually identical to those of pure Ge. The only compositional dependence that plays a critical role in our simulations is that of the direct gap E_0, which, as indicated above, is taken as $E_0(y) = E_0^{Ge}(1-y) + E_0^{\mathrm{Ge}} - by(1-y)$ with E_0^{Ge} = 0.803 eV, E_0^{Sn} = -0.4 eV, and b = -2.5 eV.

TABLE IV. Band structure and elastic parameters for pure Ge used to compute the optical absorption. A discussion on the selection of these parameters is given in Refs. 141 and 160.

E_0 (eV)	$P^2/2m$ (eV)	μ_{clh}/m	$\mu_{c\eta h}/m$	ε_0	Δ_0 (eV)	a_h (eV)	b (eV)	C_{12}/C_{11}
0.803	12.61	0.0183	0.0300	16.2	0.297	-9.64	-1.88	0.3755

Combining Eq. 50 with our model for absorption yields an expression for the EQE as a function of photon frequency and direct band gap. This expression can then be compared with, or fitted to, the experimental data.

4. Results and Discussion

(a) Photodiode fabrication. The *p-i-n* heterostructure photodiodes are more complicated than the photoconductors in several ways. They involve the use of intentionally doped films to create heterojunctions, rather just a simple slab of undoped semiconducting materials. Additionally, the device

design requires that the same metal stack be used to form ohmic contacts on both the substrate and the capping layer simultaneously. Since Ohmic contact formation is not trivial on either Si or Ge, this is an additional complication. The mask design is also less forgiving in terms of the alignment. The photoconductors had a lot of room for error in the alignment of the contacts to the mesas. In the case of the photodiodes, the tolerances are much tighter, so misalignment is a real possibility.

The addition of dopants to the materials did not seem to cause any processing issues. The doping did not affect the lithography, and the etch rates did not seem to depend on whether or not the material was doped. The tight tolerance of the metals mask did affect the ability to produce a working device. The first attempt at producing a set of photodiodes yielded devices that did not function electrically as diodes. In fact, the electrical behavior suggested that there was a short across the junction. In order to find the cause of the short, SEM images of the completed devices were obtained. FIG. 22 shows an SEM image of one of the devices. You can clearly see that the orientation of the metal contacts is slightly off from that of the mesa pattern.

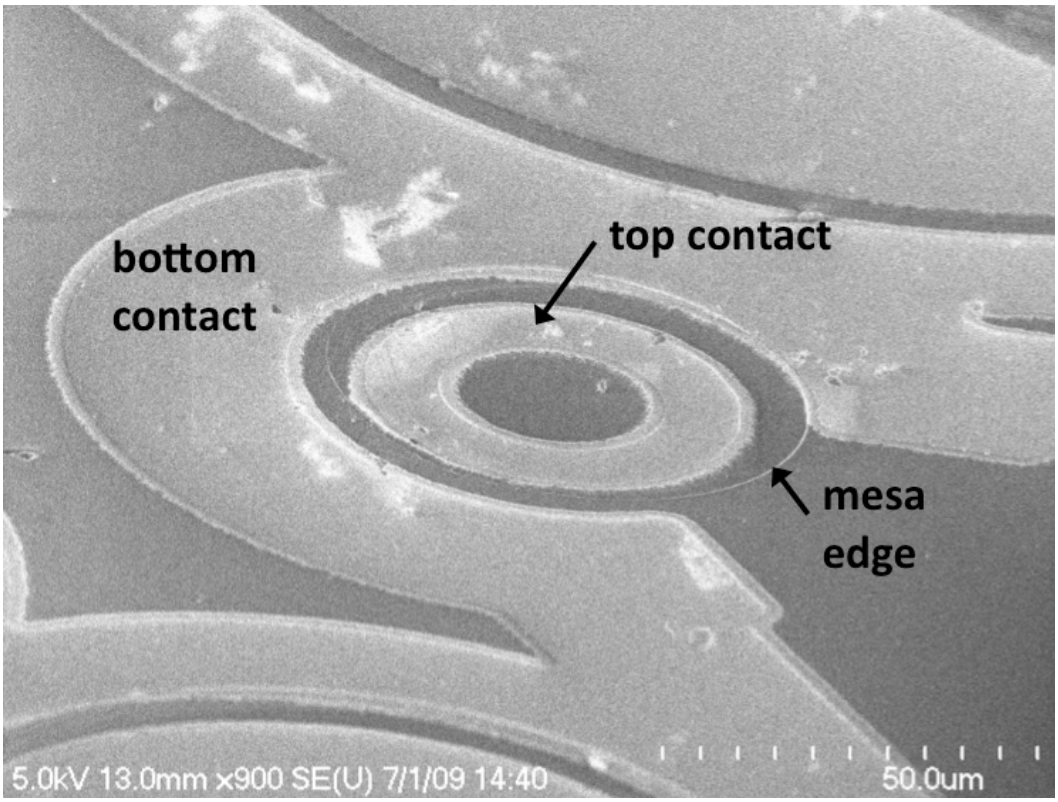

FIG. 22. SEM image of device fabricated from $Ge_{0.98}Sn_{0.02}$ films that did not show diode-like electrical characteristics. Image was taken at 5 kV energy at magnification of 900x.

From the higher magnification image in FIG. 23, we see that one metal pad is in contact with both the substrate and the top of the mesa. This is like attaching a wire to the *p* and *n* sides of a *p-n* diode. Current will flow along the shorted wire rather than through the junction. This explains the electrical behavior of the devices. This situation can be avoided by making sure the alignment is very precise. This takes some practice and a lot of patience. More details about the alignment process can be found in Appendix A.

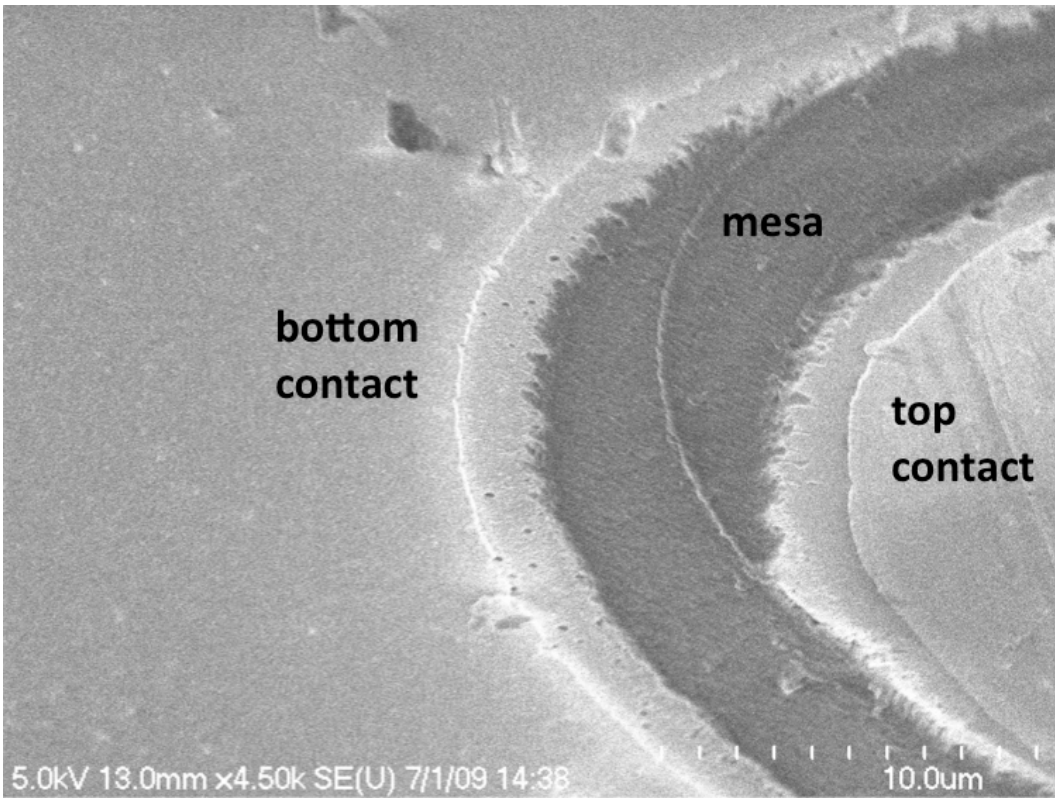

FIG. 23. SEM image of device fabricated from $Ge_{0.98}Sn_{0.02}$ films that did not show diode-like electrical characteristics. Image was taken at 5 kV energy at magnification of 4500x.

Another major issue in the fabrication process was the simultaneous formation of ohmic contacts on both the Si and Ge/GeSn surfaces. The masks we used only have one pattern for all of the metal contacts, so it is not possible to use different metals for the top and bottom contacts. Several sets of devices were attempted using silicon wafers with higher resistivities than those listed in TABLE III. It was found that the Cr/Au stack formed Ohmic contacts on the Ge/GeSn capping layers with no problem, but that the contact to Si was highly dependent on the resistivity of the wafer. In fact, Ohmic contacts could not be produced on Si using Cr/Au unless the doping in the wafer was near the 10^{19} cm^{-3} range, as it is for those wafers listed in TABLE

III. For example, use of an *n*-type Si wafer with resistivity ρ = 0.05 Ω-cm, which puts the doping in the 10^{17} cm^{-3}, range did not result in Ohmic contacts to on the Si. Thus, the devices were not usable.

(b) Characterization of Ge/Si photodiodes. The initial electrical characterization of all Ge photodiodes involved measurements of their current-voltage (I–V) curves. Typical results are shown in FIG. 24 (left) for the *p-i-n* sample with a 315-nm thick *i*-Ge layer, and in FIG. 24 (right) for the *n-i-p* sample with a 890-nm *i*-Ge layer. The plots present a set of curves obtained from diodes with diameters 60, 100, 150, 200, and 250 μm. From the slope of the linear region of the I–V curves (0.0 – 0.2 V), we have extracted an ideality factor of 1.2, which is close to the ideal value of 1. This indicates that the dark current is dominated by diffusion rather than recombination/generation in the space charge region, as expected for high-quality active Ge regions.

Further evidence for the high quality of our Ge layers is provided by the low dark current values, which compare very favorably with those reported for structures prepared under low thermal budgets. For example, Suh *et al*. find dark current densities of 2×10^{-2} A/cm^2 in *p-i-n* structures with intrinsic layer thicknesses of 1200 nm grown at 650 °C without further annealing.[142] Colace *et al*. report dark current densities of 0.2 A/cm^2 in *n-i-p* structures with 1000-nm intrinsic layers grown at 600 °C without annealing,[143] and Jutzi and coworkers find dark current densities of 0.1 A/cm^2 in *n-i-p*

structures with an intrinsic layer thickness of 300 nm and a bottom *p*-Ge layer grown by MBE at 300 °C.[144] In fact, our structures with 350-nm intrinsic layers have lower dark currents than diodes with similar intrinsic layers grown at much higher temperatures.[145]

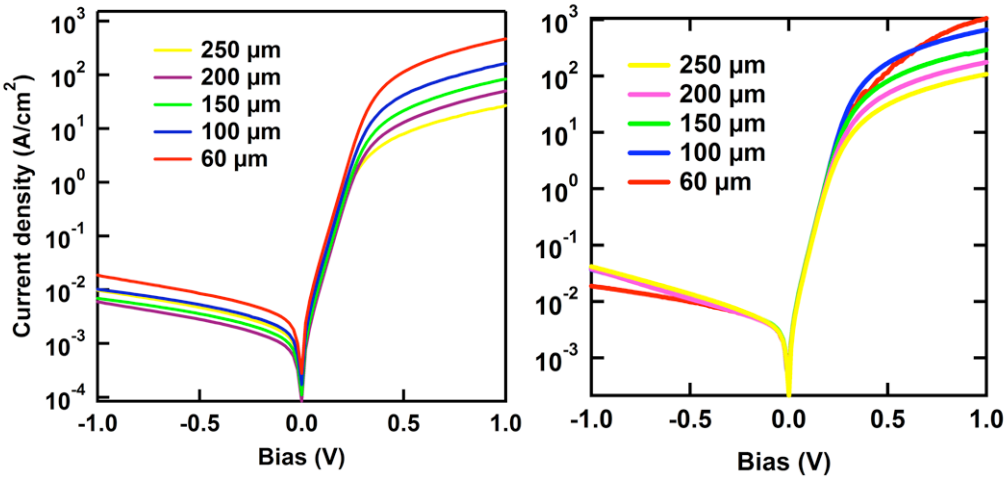

FIG. 24. Current density (A/cm2) curves for photodiodes with diameters ranging from 60 to 250 µm for samples with intrinsic region thickness of 350 (left) and 900 nm (right).

The reason for the observed low dark currents in our devices is most likely the low density of threading dislocations. In FIG. 25, we show the correlation between dark current and dislocation density as noted by Colace and Assanto is shown.[146] The grey box corresponds to our measured dark currents combined with dislocation densities found in similarly grown Ge layers.[102] Our results are in reasonable agreement with an extrapolation of the Colace—Assanto line, particularly if one considers the large errors inherent to an extrapolation of a log–log relationship.

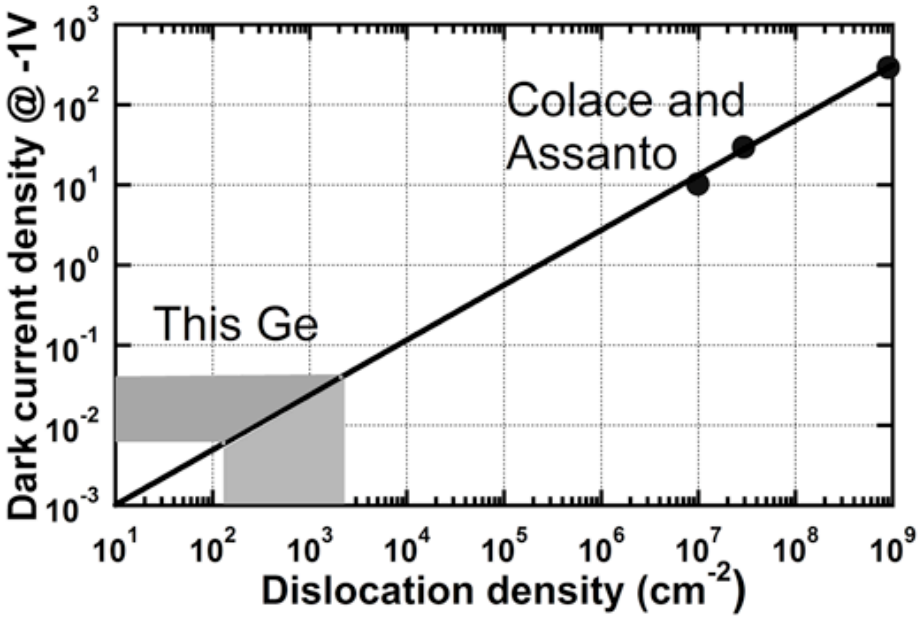

FIG. 25. Dark current versus dislocation density plot showing a best fit through the data of Colace and Assanto and the corresponding extrapolation into the regime of our electrical measurement.

Further insight into the origin of the dark current can be obtained by examining its temperature dependence. Arrhenius plots of dark current versus temperature for a set of reverse bias values between −0.2 and −1 V are shown in FIG. 26 for the p-i-n sample with the 350-nm intrinsic layer. From the slope of these curves, we obtain thermal activation energies E_a, which decrease with applied bias. The low-bias activation energies are noticeably higher than half the Ge band gap, indicating a significant diffusion contribution to the dark current, as expected from the low ideality factor of 1.2. Masini and coworkers[147] have modeled the dark current in *n-i-p* and *p-i-n* devices. The *p-i-n* structure is found to be independent of the interface recombination velocity, but for *n-i-p* structures the dark current depends strongly on the interface recombination velocity for the case of highly doped

substrates, such as those used here. Therefore, a direct comparison of dark currents between *p-i-n* and *n-i-p* devices is not straightforward.

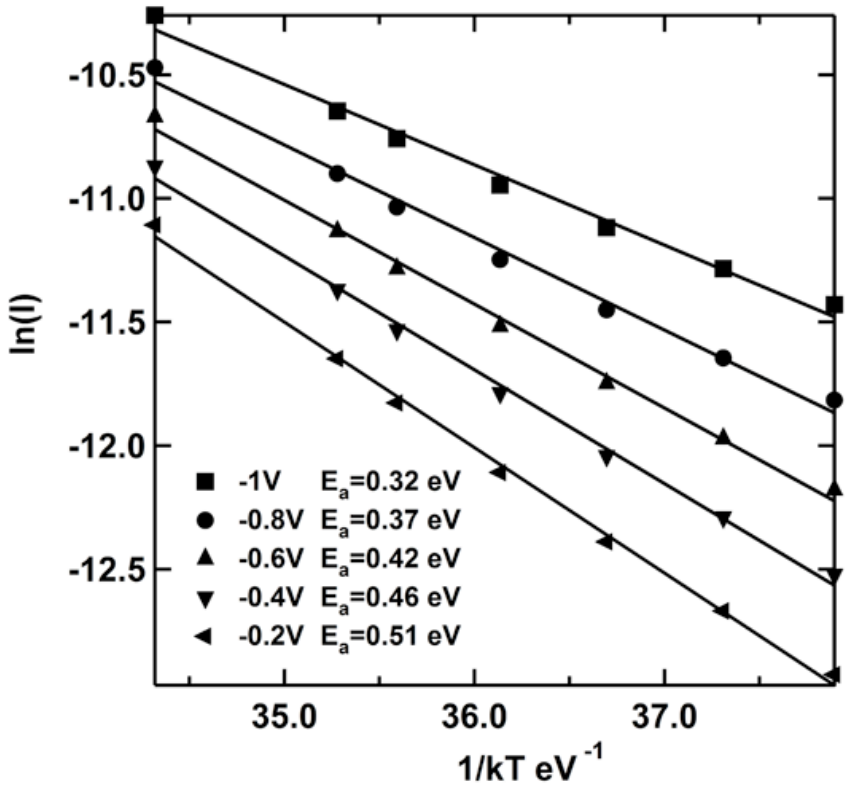

FIG. 26. Arrhenius plot of the dark current showing an increase of the activation energy with increasing reverse bias. The activation energies $E_a > E_g/2$ indicate that the dark current is dominated by diffusion.

The dark current densities do not show a strong correlation with the device diameter, from which we conclude that the leakage current is generated at the Si/Ge interface or within the bulk of the material rather than the sidewalls. This indicates that surface states do not play a significant role in the generation of the dark current. From this, we conclude that the SiO_2 coating is sufficient for passivation of the Ge surface.

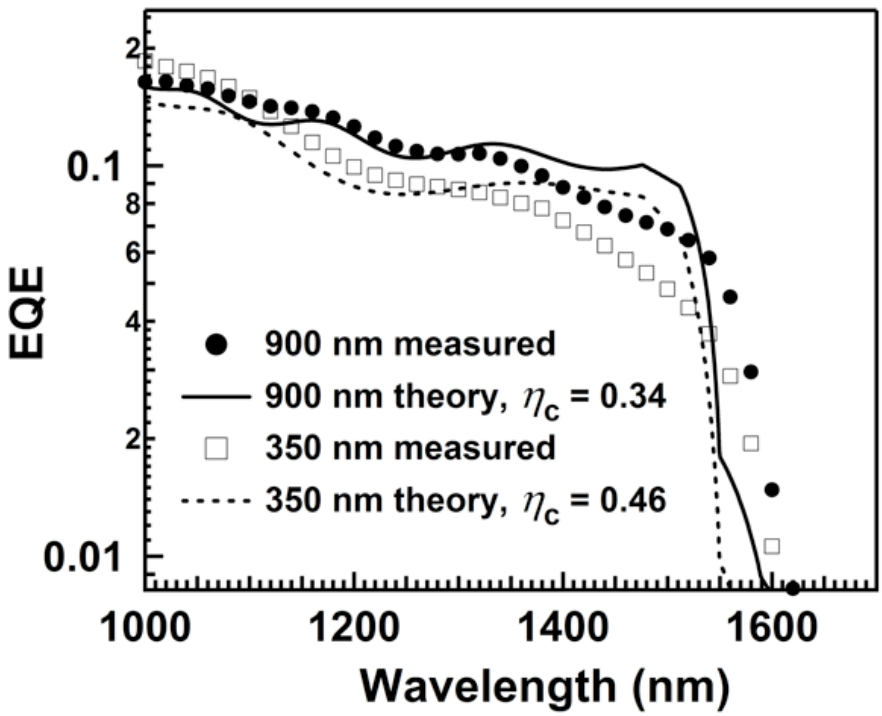

FIG. 27. EQE plots for two Ge/Si diode devices. Circles and squares represent experimental data. The lines are fits based on (1) in which the Ge layer thicknesses are adjusted to match the EQE oscillations and the collection efficiency is adjusted to fit the measured EQE at 1300 nm.

The photodiodes were also characterized with respect to their optical response. A plot of the external quantum efficiency (EQE) of two 300 μm diameter Ge/Si photodiodes as a function of incident photon wavelength is shown in FIG. 27. The theoretical curves (lines) in are fits to the experimental data (markers) using Eq. 50, in which the collection efficiency η_c is treated as an adjustable parameter, and the thickness of the intrinsic layer is adjusted to match the observed EQE oscillations. We find η_c = 0.46 for the thinner *p-i-n* sample and η_c = 0.34 for the thicker sample. The fitted layer thicknesses (87 nm *n*-Ge and 860 nm *i*-Ge in the *n-i-p* diode, and 103 nm *p*-Ge and 389 nm *i*-Ge in the *p-i-n* diode) are within 4% of the thicknesses determined from

ellipsometric measurements on the wafer prior to device processing. The discrepancy between theory and experiment at the onset of absorption in the 1500–1600-nm range is not surprising given the strong temperature dependence of the absorption coefficient in this wavelength range,[148] the possibility of residual strain effects associated with processing, and the change in the optical constants of Ge under heavy doping, which are neglected in the simulation.

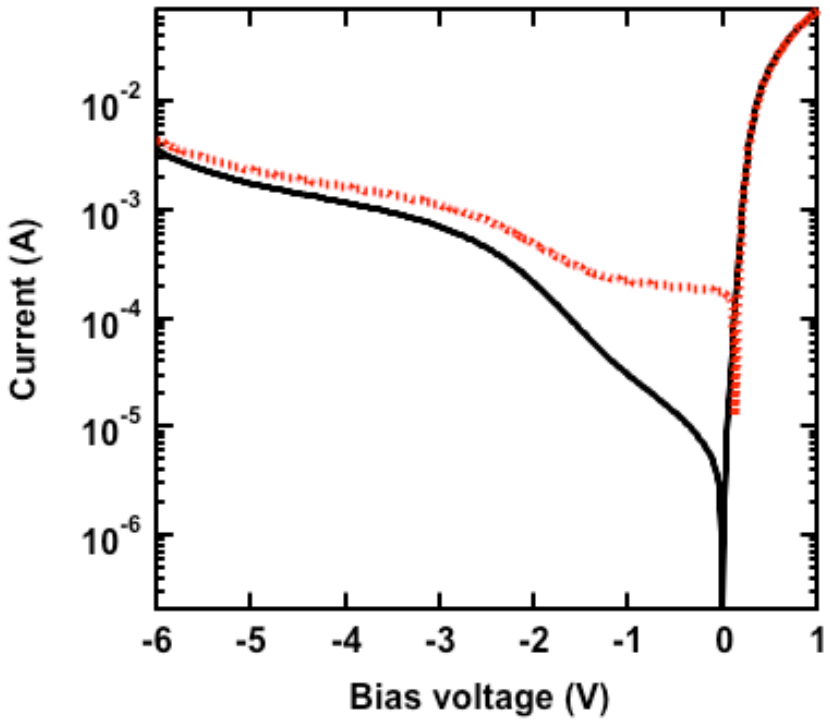

FIG. 28. I–V curves of the 900-nm Ge photodiode without and under illumination by a 0.6 mW laser diode operating at 1300 nm.

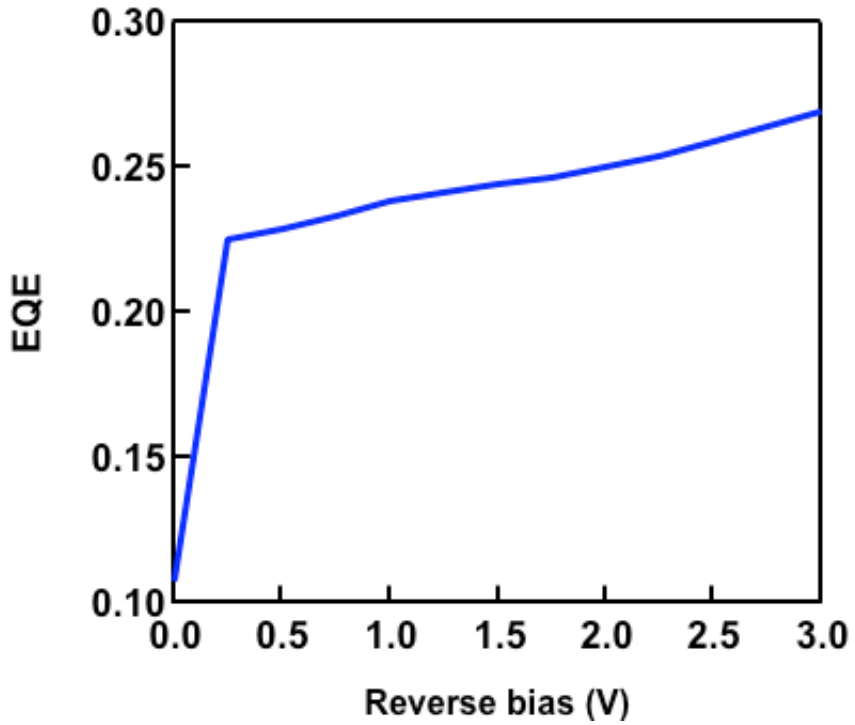

FIG. 29. EQE dependence on reverse bias of the 900-nm Ge photodiode without and under illumination by a 0.6 mW laser diode operating at 1300 nm.

The relatively low value of the collection efficiency at zero bias is probably due to residual doping in the intrinsic region. This interpretation implies that the collection efficiency should increase with reverse bias.[75] In FIG. 28, we show I–V curves for the *n-i-p* detector with an intrinsic region of 900 nm and a diameter of 300 μm. The curves were measured under dark conditions and illumination with a laser emitting 0.6 mW of 1300-nm radiation. The substantial difference between the illuminated and dark current as shown in FIG. 28 (red and black traces, respectively) allows us to extend the EQE measurements to a large reverse bias. At a bias of −0.25 V, the collection efficiency of the *n-i-p* device is $\eta_c = 0.7$ and reaches full collection at about −6 V. This behavior has been observed in Ge diodes based

on similar heterojunction designs.[149] Similar measurements of a 300-μm diameter *n-i-p* detector with a 350-nm intrinsic layer show that, at a bias of −0.25 V, full collection efficiency is achieved.

(c) Characterization of $Ge_{0.98}Sn_{0.02}$/Si photodiodes. First, we examine the results obtained from the *p-i-n* photodiodes fabricated from $Ge_{0.98}Sn_{0.02}$ films. Current density versus voltage measurements were conducted, and representative plots for devices sizes ranging from 60 to 250 μm in diameter are show in FIG. 30. The results indicate that the dark current densities at −1 V bias are ~1 A/cm^2, which is 2–3 orders of magnitude higher than those found in the pure Ge devices. This can be attributed to both the lower band gap of the GeSn material and to its higher dislocation density relative to Ge. The excess dark currents are consistent with the intermediate value obtained for the diode ideality factor of 1.5, suggesting a significant contribution from recombination–generation processes. In fact, the defect concentration is estimated to be significantly higher (by approximately two orders of magnitude) relative to the defect concentrations in the Ge samples.

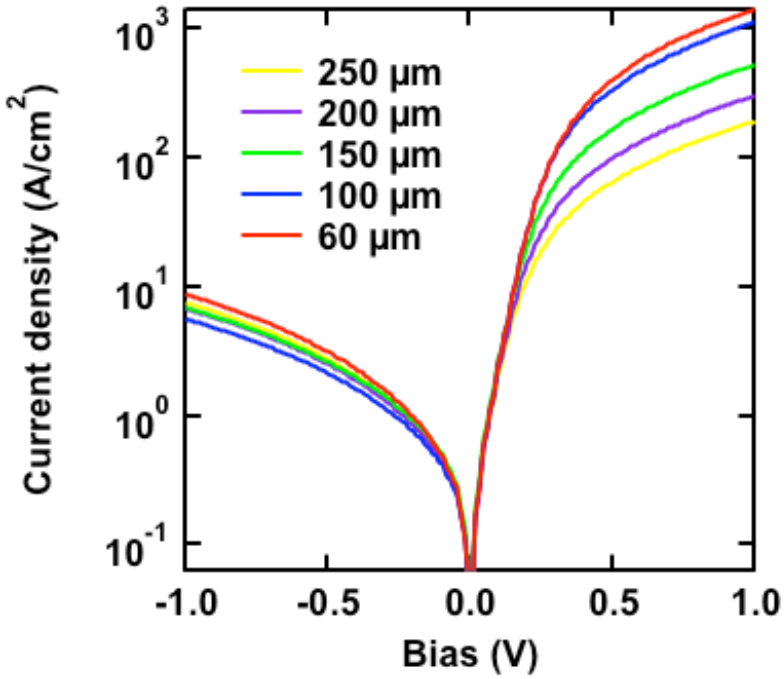

FIG. 30. Dark current density plots for the $Ge_{0.98}Sn_{0.02}$ photodiodes with mesa diameters ranging from 60 to 250 μm and active layer thickness of 350 nm.

The nature of the dark currents can be further investigated from their temperature dependence. The Arrhenius plots in FIG. 31 indicate that the activation energies E_a for a typical 250-μm device decrease from 0.18 to 0.09 eV with increasing reverse bias from 0.2 to 1 V, respectively. These values are much lower than those obtained from the pure Ge devices. Since $E_a << E_g/2$, we believe that some other mechanism in addition to recombination–generation contributes to the dark current. Similar low activation energies were reported in Ge diodes by Huang *et al.*[149] albeit at low temperatures. These workers point out that low activation energies may signal tunneling contributions to the dark current.

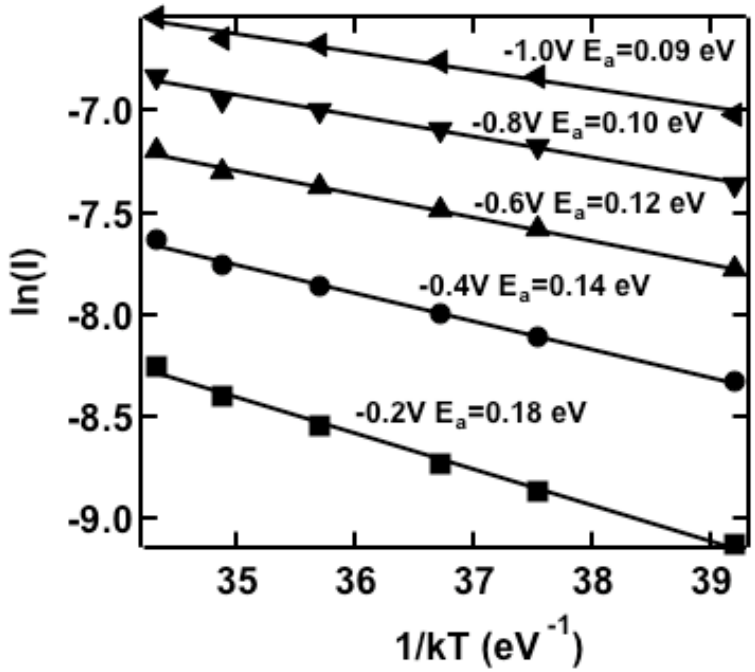

FIG. 31. Arrhenius plots (natural log of dark current versus 1/kT) of devices with 250 μm diameter. Corresponding activation energies indicate a significant contribution to the dark current from recombination generation.

In FIG. 32, we show the EQE of the $Ge_{0.98}Sn_{0.02}$/Si *n-i-p* device with an intrinsic layer thickness of ~350 nm. The EQE was measured at 0 V bias following the same protocol as with the Ge-based diodes. The solid line is a fit with Eq. 50, in which we use the absorption coefficients of $Ge_{0.98}Sn_{0.02}$, as measured by ellipsometry, in place of those of pure Ge. The fit gives η_c = 0.70, which is substantially higher than obtained from the Ge devices. Full collection is achieved at a reverse bias of −0.25 V. This, combined with the alloys' stronger optical absorption, leads to EQEs that are significantly higher than those of the thicker Ge analogs across the entire near-IR range. At telecom wavelengths of 1300 and 1550 nm, the EQEs of the GeSn photodiode are 0.14 and 0.09, respectively, which is ~30% higher than the corresponding

values of 0.1 and 0.056 determined for the 900-nm thick Ge device. Most importantly, the plot provides unequivocal evidence that the incorporation of even small amount of Sn at 2 at% into Ge significantly extends the detection range of the material. In particular, the EQE of this diode over the L band (1565–1625 nm) is about a factor of 2 higher than that of any tensile-strained Ge device in the literature,[75,142] confirming the attractive properties of $Ge_{1-y}Sn_y$ alloys for detection in this wavelength range.

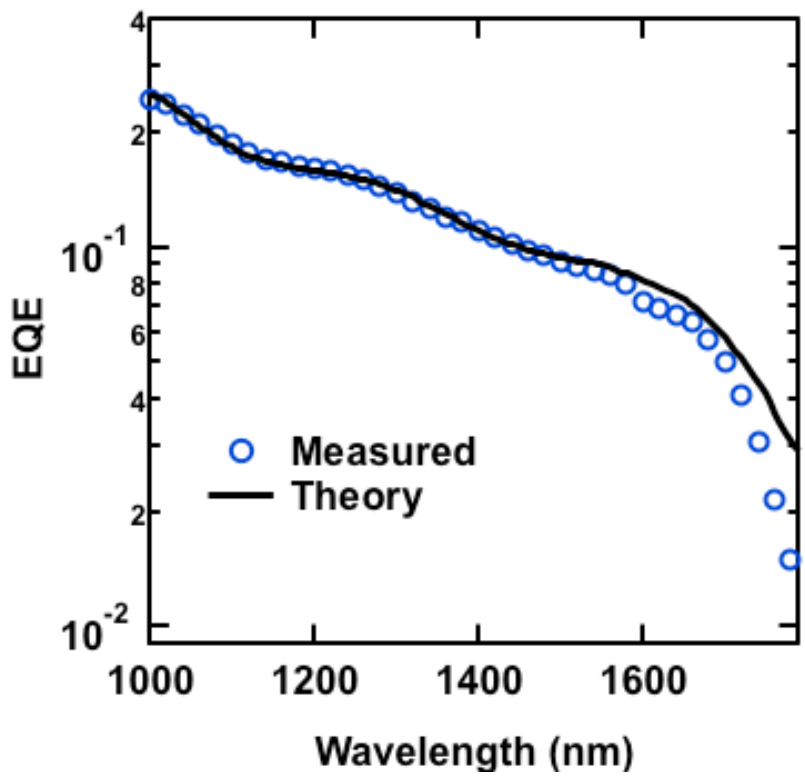

FIG. 32. Experimental (markers) and theoretical (line) EQE of $Ge_{0.98}Sn_{0.02}$ photodiode. Theoretical data was computed using Eq. 50 with absorption coefficients measured by ellipsometry.

(d) Characterization of $Ge_{0.99}Sn_{0.01}$/Si photodiodes. The electrical properties of the completed photodiodes were characterized by measuring

the dark current density vs. voltage dependence for the various device sizes. The plot in FIG. 33 shows the current densities, which are nearly independent of device size in the reverse direction. This indicates that the dark current is most likely generated in the bulk of the material or at the Si/$Ge_{0.99}Sn_{0.01}$ interface. The data was also used to extract a diode ideality factor of 1.5, which indicates that recombination-generation in the space-charge region plays a large role in the generation of the dark current.

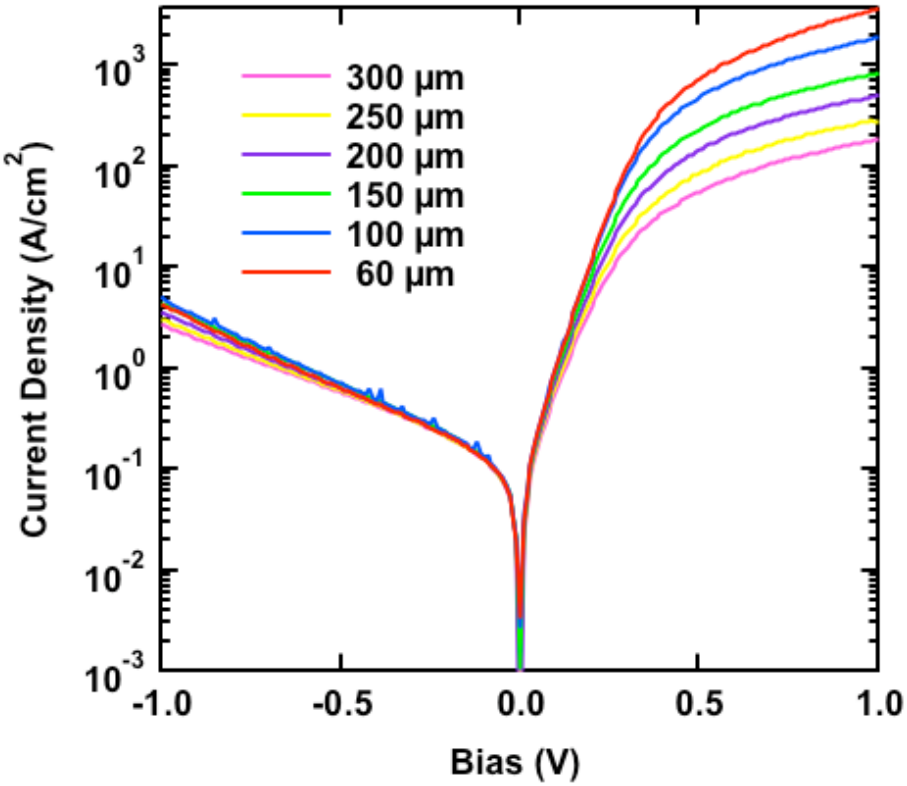

FIG. 33. Dark current density vs. voltage curves for various sized diodes fabricated from $Ge_{0.99}Sn_{0.01}$ films.

We can compare these dark currents to those measured in similar Ge (FIG. 24, left) and $Ge_{0.98}Sn_{0.02}$ samples (FIG. 30) While the different samples

do have some slight differences in thicknesses and geometry, the results can still be compared. The $Ge_{0.99}Sn_{0.01}$ devices exhibit lower dark currents than their 2% counterparts, but they have higher dark currents than the pure Ge devices. This could be due to threading dislocation densities increasing with Sn content, however detailed studies of the defect densities as a function of Sn content have yet to be conducted. The differences in dark currents in the two GeSn devices cannot be compared on equal footing however, due to the inversion of the doping type in the substrates and capping layers. This reversal of the structure leads to a difference in the alignment of the energy bands. This causes differences in dark currents, which depend on surface and interface recombination velocities, as explored by Masini, *et al.*[147]

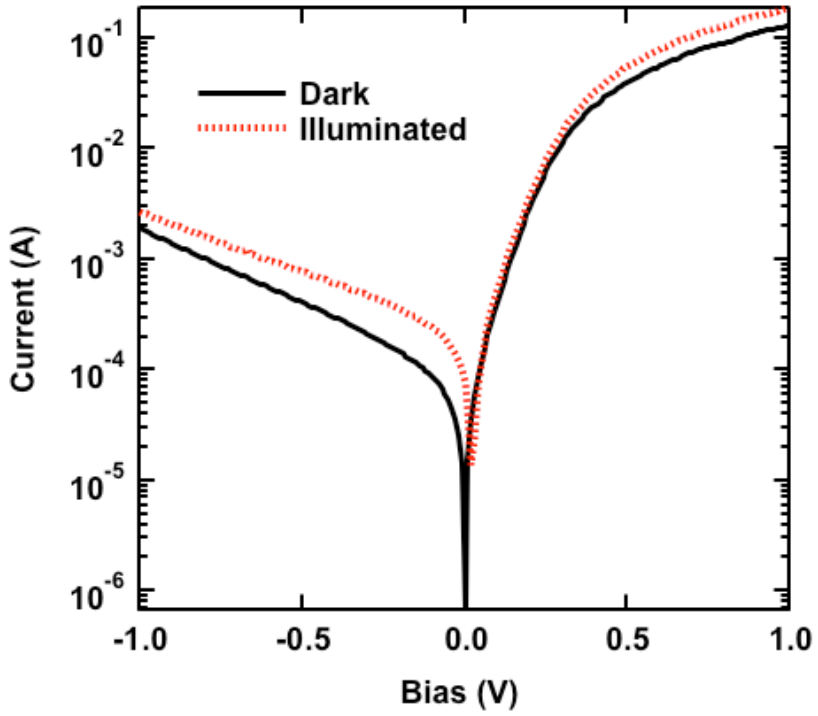

FIG. 34. Current vs. voltage curves for a 300 μm $Ge_{0.99}Sn_{0.02}$ photodiode with and withouth illumination by a 1300 nm laser at 0.6 mW.

The optical response of the devices was initially characterized by measuring the current through a 300 μm device under illumination by a 1300 nm laser source and comparing it with the dark current, as shown in FIG. 34. The significant difference between the dark and illuminated current indicates that the device should work well as a detector at this wavelength. This difference is substantial even at negative bias, so the performance of the device may be enhanced through application of a reverse bias to the detector.

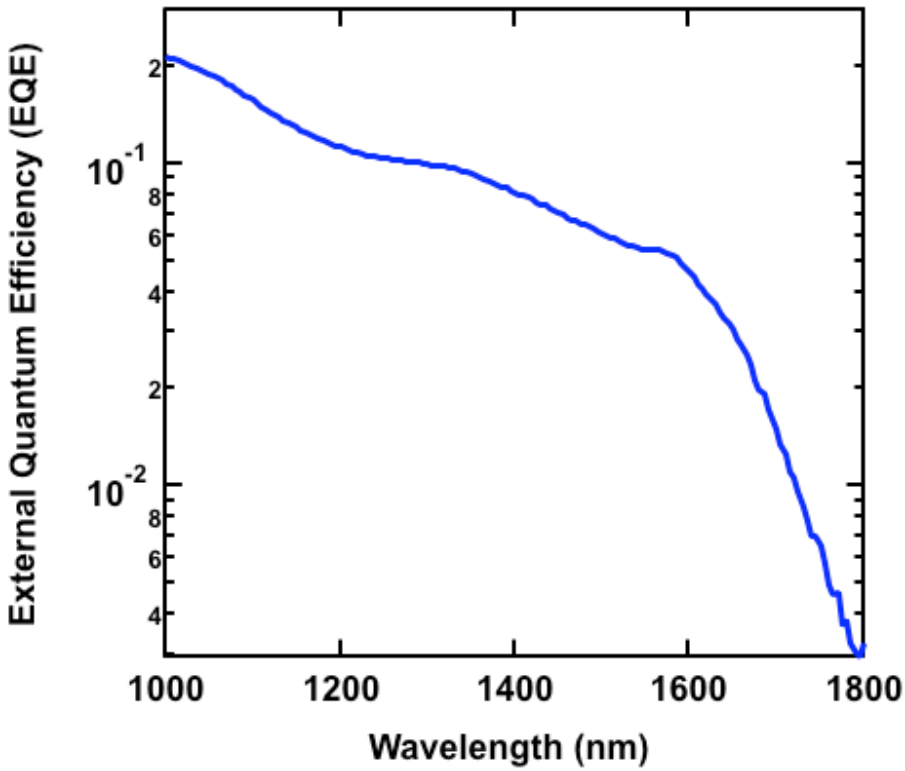

FIG. 35. EQE at zero bias of a 300 μm diameter $Ge_{0.99}Sn_{0.01}$ photodiode is plotted as a function of wavelength.

The EQE of a typical 300 μm device is plotted as a function of wavelength in FIG. 35. The response is high for wavelengths below the band gap of Ge, as expected. At longer wavelengths the responsivity is substantial, eventually cutting off at about 1750 nm. The responsivities at 1300 and 1550 nm were measured to be 0.1 and 0.07 A/W, respectively, at zero bias. The application of a reverse bias of only 0.2 V to the detector circuit was found to increase the responsivity of the device to a maximum of 0.16 A/W.

(e) Characterization of $Ge_{0.998}Sn_{0.002}$/Si photodiodes. Current-density vs. voltage measurements were conducted and a representative curves for 50, 100, 200, and 300 μm devices are shown in Figure 3. If we compare this with I-V curves measured from a similar pure-Ge on Si device (FIG. 24, left), we see that the curves exhibit a similar rectifying behavior, but with a somewhat better ideality factor (1.2) in the Ge device than in $Ge_{0.998}Sn_{0.002}$ device (1.3). The dark current densities at -1V are about one order of magnitude higher in the $Ge_{0.998}Sn_{0.002}$ device. On the other hand, similar diodes based on $Ge_{0.98}Sn_{0.02}$ layers show dark currents close to 10 A/cm^2, so that the Sn-doped material represents a significant improvement over bona fide alloys.

In the case of the pure Ge device, the dark current has a thermal activation energy E_a = 0.32 eV at V = -1 V, which is close to to $E_g/2$, where E_g is the fundamental band gap. This clearly indicates a Shockley-Read-Hall (SRH) generation mechanism. In the Sn-doped material, substitutional Sn has a measurable impact on carrier mobilities via alloy scattering, but it can be

ruled out as the source of additional SRH trap states due to the isoelectronic nature of Sn and Ge. In fact, a study of the temperature dependence of the dark current (Figure 3(b)) reveals an activation energy of E_a = 0.17 eV at -1V, which is substantially below the value of E_a obtained in the pure Ge diode. This indicates that the excess dark current in the Sn-doped device is not due to enhanced SRH generation but to some alternative mechanism.

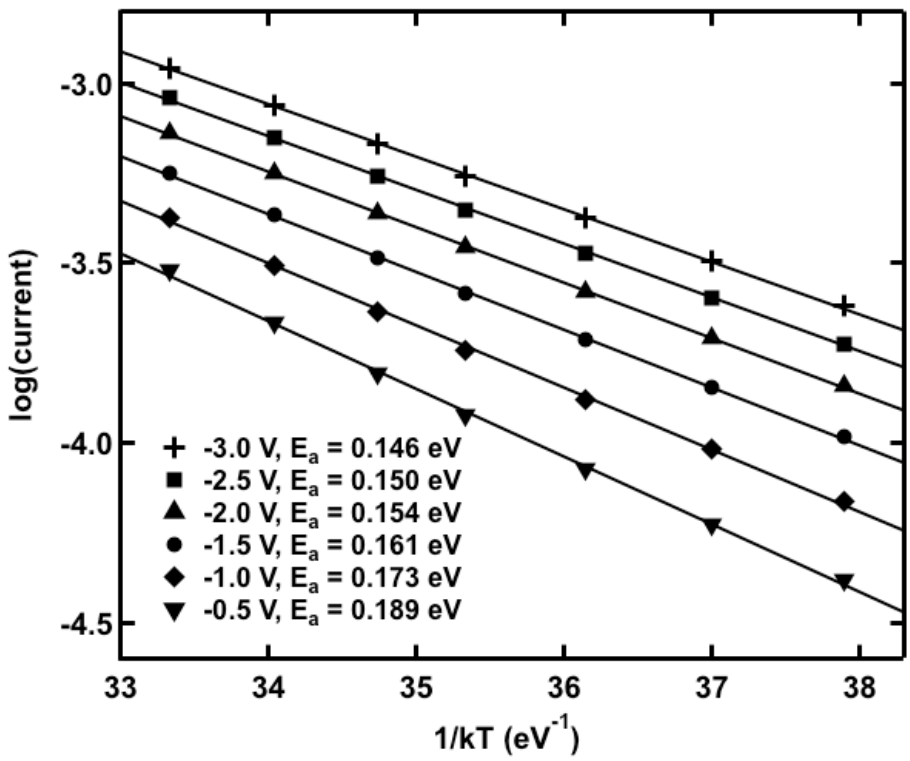

FIG. 36. Arrhenius plots of the dark current density at selected reverse bias values for a 100 µm $Ge_{0.998}Sn_{0.002}$ diode.. Activation energies are obtained from the line slopes.

Very low values of the activation energy have been associated with tunneling transitions.29,30 At this point it is unclear if the defects that cause the excess dark current in the Sn-doped diodes are located at the interface

with the Si substrate or in the material's bulk. The microstructural similarities between the pure-Ge-on-Si and Sn-doped Ge-on-Si interfaces, combined with the observation of a standard SRH mechanism in the pure-Ge-on-Si diodes, suggest a bulk origin for the excess dark current in the Sn-doped devices. However, the detailed mechanism by which layer-by-layer growth proceeds at the interface with Si may be very different in the two cases, since the pure-Ge material is grown by gas-source molecular beam epitaxy of Ge_2H_6 assisted by the $CH_2(GeH_3)_2$ metalorganic additive,22 whereas the Sn-doped material is grown via CVD of Ge_2H_6 in the presence of SnD_4. Thus one cannot rule out the possibility that different type of interface states may be generated by each of these growth processes. Further investigations of this issue will require systematic studies of devices with varying Sn concentrations and thicknesses. It is interesting to note that in diodes based on $Ge_{0.98}Sn_{0.02}$ layers the measured dark count activation energy at -1V is even smaller (E_a = 0.09 eV) Thus the intermediate E_a value obtained for the $Ge_{0.998}Sn_{0.002}$ device may signal the onset of a transition from tunneling to SRH generation. A final point to make regarding the I-V characteristics is that investigations of the dependence of the dark current density on the device diameter suggests that the leakage currents do not originate from the sidewalls of the mesas.

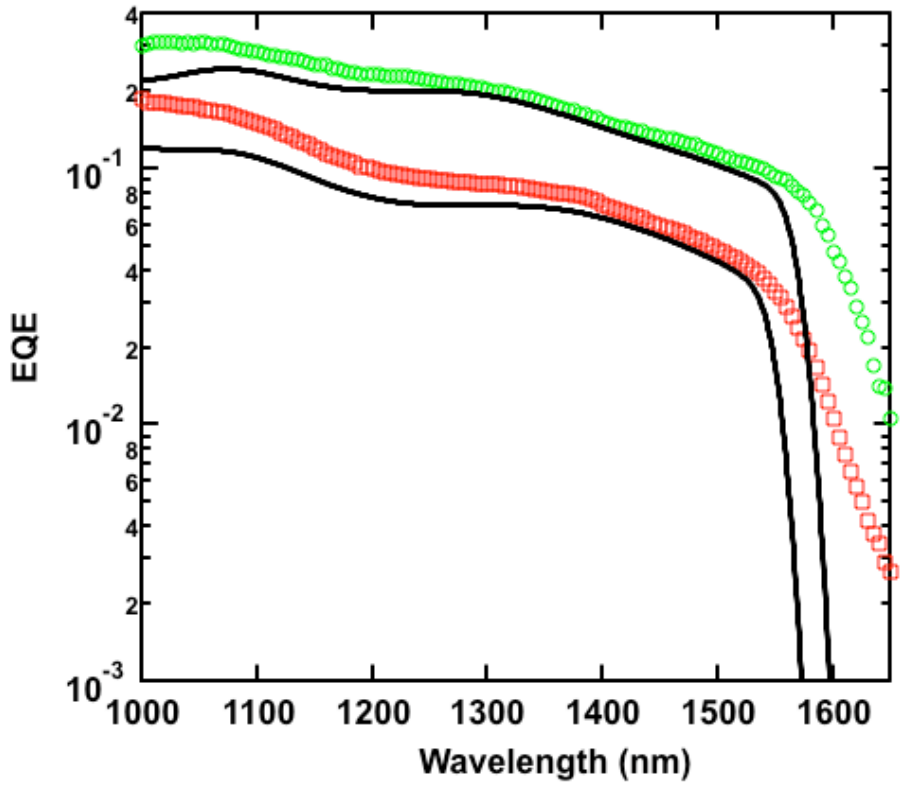

FIG. 37. Experimental (markers) and theoretical (line) EQE obtained from 300 μm diameter $Ge_{0.998}Sn_{0.002}$ and pure Ge photodiodes.

The EQE wavelength dependence at zero bias is shown in FIG. 37. The large drop in responsivity beyond ~1600 nm is associated with the lowest direct band gap of these materials near 0.8 eV. Superimposed with the step-like onset of responsivity at 1600 nm we see oscillations at shorter wavelengths that are due to interference effects. These are enhanced by computing the derivatives dR/dλ of the responsivities, as shown in Fig. 5.

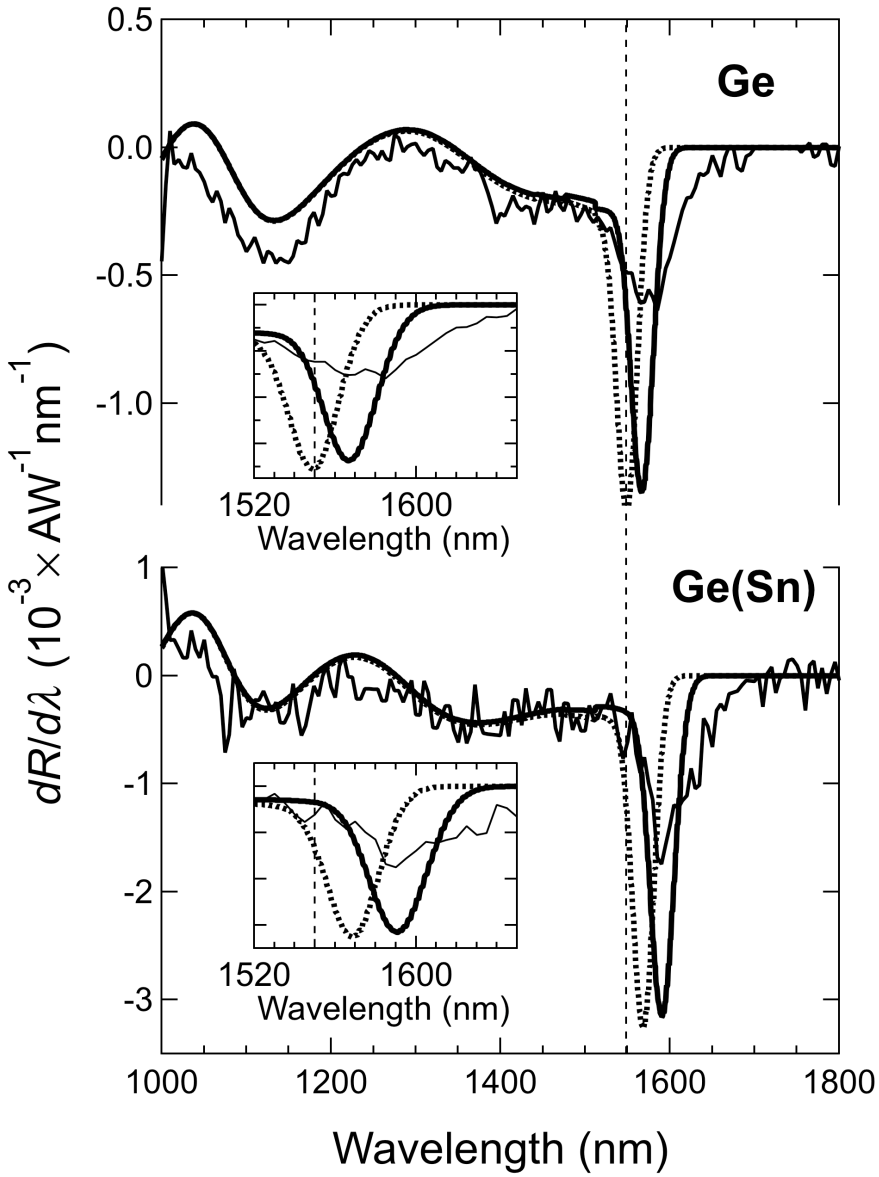

FIG. 38. Derivatives of responsivity for the two diodes in FIG. 37. The thin solid lines are numerical derivatives of the experimental data. The thick solid lines correspond to the derivatives of the model responsivities in Fig 4, and the dotted lines are the derivates of the same theoretical calculations but setting the strain equal to zero. The vertical line corresponds to 1550 nm. The insets show in more detail the spectral region around this wavelength.

The most striking feature in FIG. 37 and FIG. 38 is the clear shift to longer wavelengths in the responsivity onset corresponding to the Sn-doped device, indicating a direct band gap reduction that is clearly measurable even

for a Sn concentration as low as 0.25%. We also note that this shift is not accompanied by a broadening of the absorption edge, as seen in the case of $Ge_{0.98}Sn_{0.02}$ alloys. If anything, the direct gap onset appears to be slightly sharper in the Sn-doped device. Since the observed shift between the two diodes is comparable in magnitude to those typically induced by strain, a detailed model is needed to quantify the relative contributions from composition and strain. The model must also account for interference effects caused by the optical mismatch of the different layers.

The calculated EQE for the device using the theoretical model is also shown in FIG. 37. The band gap of the $Ge_{1-y}Sn_y$ alloy was interpolated between that of Ge and α-Sn using the standard expression $E_0(y) = E_0^{Ge}(1-y) + E_0^{Sn}y - by(1-y)$ with E_0^{Ge} = 0.803 eV, E_0^{Sn} = -0.4 eV, and b = -2.5 eV (Ref. 31). The overall thickness of the intrinsic and *p*-doped layer was adjusted to match the oscillations in FIG. 38, and the results were within 5% of the values determined from the RBS and ellipsometry measurements. The collection efficiency was fit to the experimental responsivity at 1550 nm, and we obtained η_c = 0.67 for the Sn-doped diode and η_c = 0.38 for the pure-Ge diode. These less than perfect collection efficiencies at zero bias are probably related to the 10^{16} cm^{-3} residual doping in the intrinsic layers. It is apparent from FIG. 37 that the collection efficiencies are higher at short wavelengths.

At long wavelengths, the drop in the theoretical responsivity curve is much sharper than observed experimentally, an effect that can also be seen

in the derivative profiles. This is because our simulation does not include indirect gap absorption. In spite of this limitation, the model accounts very well for the relative spectral shift between the two diodes. To understand the contributions to this shift, we show in the inset to FIG. 38 (as dotted lines) the expected responsivity derivatives in the absence of any strain. The effect of strain and composition are seen to be of the same order of magnitude.

The derivative curves in FIG. 38 offer an easy graphical interpretation of the "diminishing returns" condition mentioned in the introduction. The negative peak near 1550 nm represents the spectral range over which the responsivity changes rapidly as a function of strain and/or composition. Once this peak is to the right (longer wavelengths) of the vertical line corresponding to 1550 nm, further increases in Sn concentration and/or tensile strain lead to much smaller gains in responsivity. It is apparent that our Sn-doped sample has a nearly ideal combination of tensile strain and composition to meet this condition. To accomplish the same result based solely on pure Ge, a tensile strain level of 0.2% would be needed. In fact, such a detector was fabricated by Liu *et al.*[75] They report a responsivity R = 0.56 A/W at 1550 nm from a 2410 nm-thick Ge on Si diode in which a tensile-strain level of 0.2% is obtained by growing the bulk of the Ge layer at 700 °C and annealing the sample at 900 °C. At 1550 nm and assuming $\eta_c = 1$, our model predicts a responsivity R = 0.55 A/W for this diode—in very good agreement with the experimental value—and R = 0.54 A/W from a detector based on a material with the same Sn concentration and strain level as in our

Sn-doped Ge. On the other hand, if we want to obtain the same responsivity using perfectly relaxed Sn-doped layers, we need a Sn concentration of 0.6%. This is less than the concentration of 0.8% that would be needed to match the lowest direct band gap in both materials, following the analysis in the introduction. The discrepancy can be understood by recalling that strain broadens the absorption edge due to the light-heavy hole splitting. While this broadening is very small in the derivative profiles shown in FIG. 38, a similar plot for a tensile strain level of 0.2% shows clear evidence of the separate absorption edges associated with the light- and heavy-hole bands.

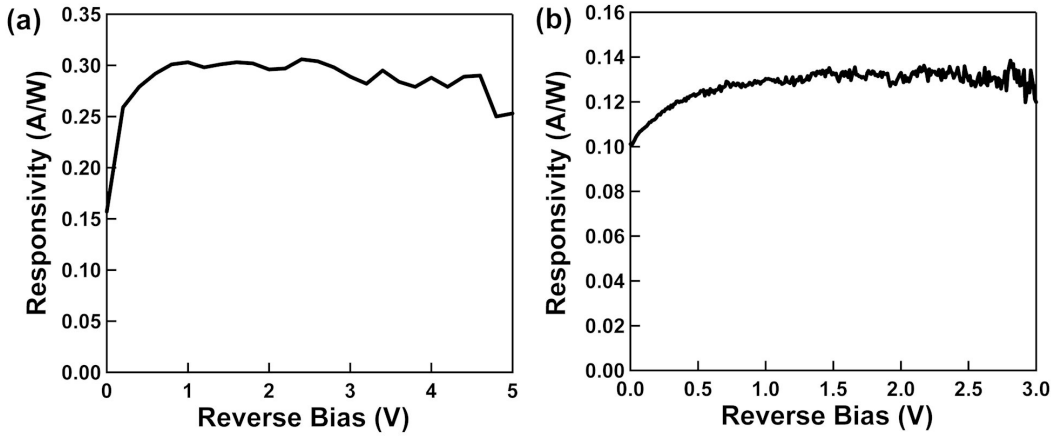

FIG. 39. Responsivity vs bias of $Ge_{0.998}Sn_{0.002}$ photodiode under illumination by a laser diode at 1300 nm (a) and 1550 nm (b).

For η_c = 1, our model predicts the responsivity R = 0.30 A/W at 1300 nm and R = 0.17 A/W at 1550 nm for our Sn-doped sample. In Fig. 6 we show the bias dependence of the responsivity at these two wavelengths and we see that at 1300 nm we do approach complete carrier collection at reverse biases above 0.5 V. At 1550 nm, on the other hand, the asymptotic value of the responsivity is 0.13 A/W, which corresponds to a collection efficiency of η_c =

0.74. These bias-dependence measurements were carried out under laser illumination, and therefore the zero bias values are probably not directly comparable to those obtained under much weaker lamp illumination.

(f) Characterization of $Ge_{0.97}Sn_{0.03}$/Si photodiodes. Representative current-voltage curves obtained from 250 and 500 μm diameter diodes are shown in FIG. 40. The dark currents are an order of magnitude higher than those in the $Ge_{0.98}Sn_{0.02}$ diodes. This follows the trend of the rise in dark current densities with increasing Sn incorporation. The high amount of current means that the current-voltage curve is affected severely by series resistance. This makes it difficult to find a linear part of the curve for the calculation of the ideality factor. Depending on which part of the curve is selected, we can get values of 1.2-1.8 for the ideality factor, so it does not tell us much. Still, from the rest of the curve, it seems that this diode does not have features as sharp as those from the other diodes. Most likely, the current in these diodes is dominated by recombination-generation in the space charge region. The curvature in the reverse direction also makes it difficult to perform thermal measurements since there is no real saturation current.

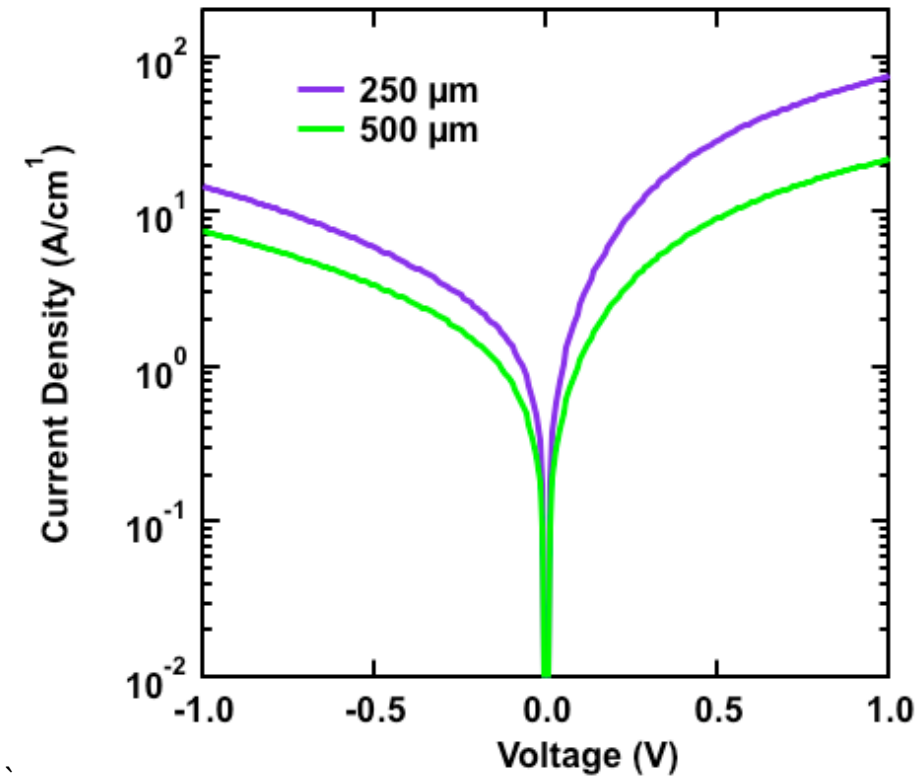

FIG. 40. Current-voltage curves obtained from diodes fabricated from $Ge_{0.97}Sn_{0.03}$ films.

The EQE was measured as a function of wavelength, as pictured in FIG. 41. The EQE remains high almost all the way out to 1800 nm, which is the end of our detection capability. This seems to be a further extension past the range covered by the $Ge_{0.98}Sn_{0.02}$ detector. However, the high dark currents lead to a degraded signal-to-noise ratio, making the curve unusually noisy compared to measurements on the photodiodes produced from lower Sn content films.

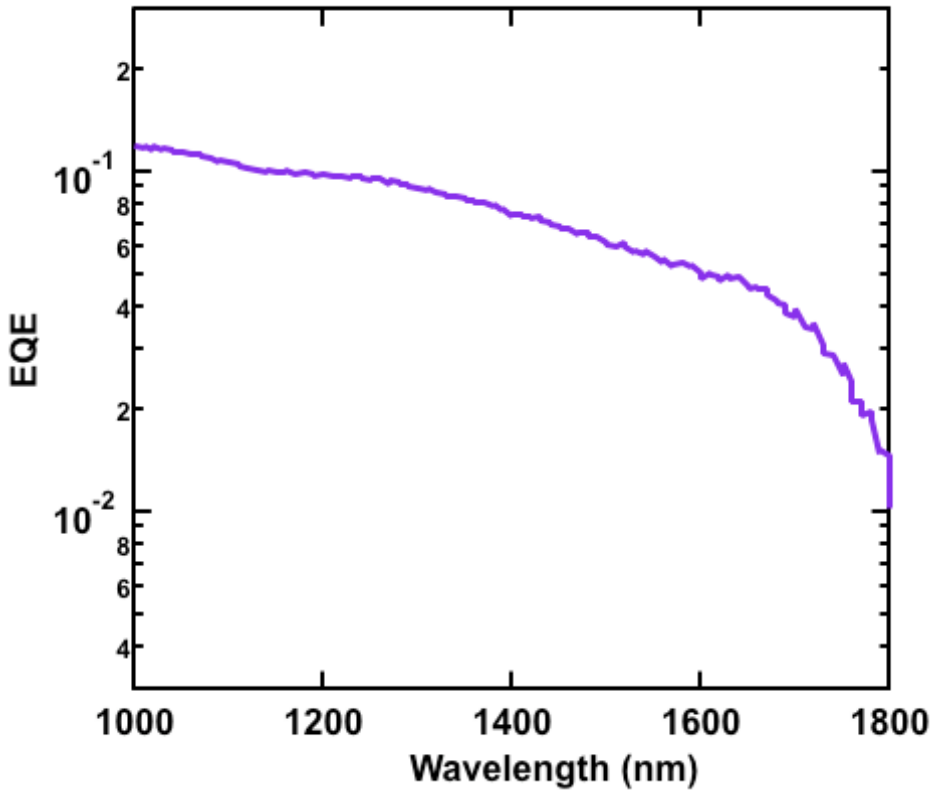

FIG. 41. EQE vs. wavelength obtained from a $Ge_{0.97}Sn_{0.03}$ photodiode at zero bias.

5. Conclusions

The results obtained from the photodiodes fabricated from films with the various Sn concentrations can be compared for additional insight into the properties of the GeSn films. First, we examine the dark current densities, which are pictured in FIG. 42. The lowest reverse currents were measured on the devices made from pure Ge films, which showed results comparable to those obtained from similar high performance Ge-on-Si diodes. These diodes also exhibited the best rectifying behavior, as evidenced by the difference in height of the two sides of the I-V curve. The reverse current is fairly flat, similar to the behavior of an ideal diode. Additionally, the ideality factor (1.2)

obtained from the I-V curve and measurements of the activation energy of the reverse saturation current indicate that the current in these diodes is mainly due to diffusion, as is the case for high quality devices. The addition of 0.2 % Sn into the Ge active layer resulted in an increase of about two orders of magnitude in the dark current, but the diodes still exhibit good rectifying behavior. The reverse current is fairly flat, as in the pure Ge case. The ideality factor increases to 1.3, which indicates a slight shift away from diffusion driven current, and the low activation energy of the saturation current could indicate the onset of tunneling current.

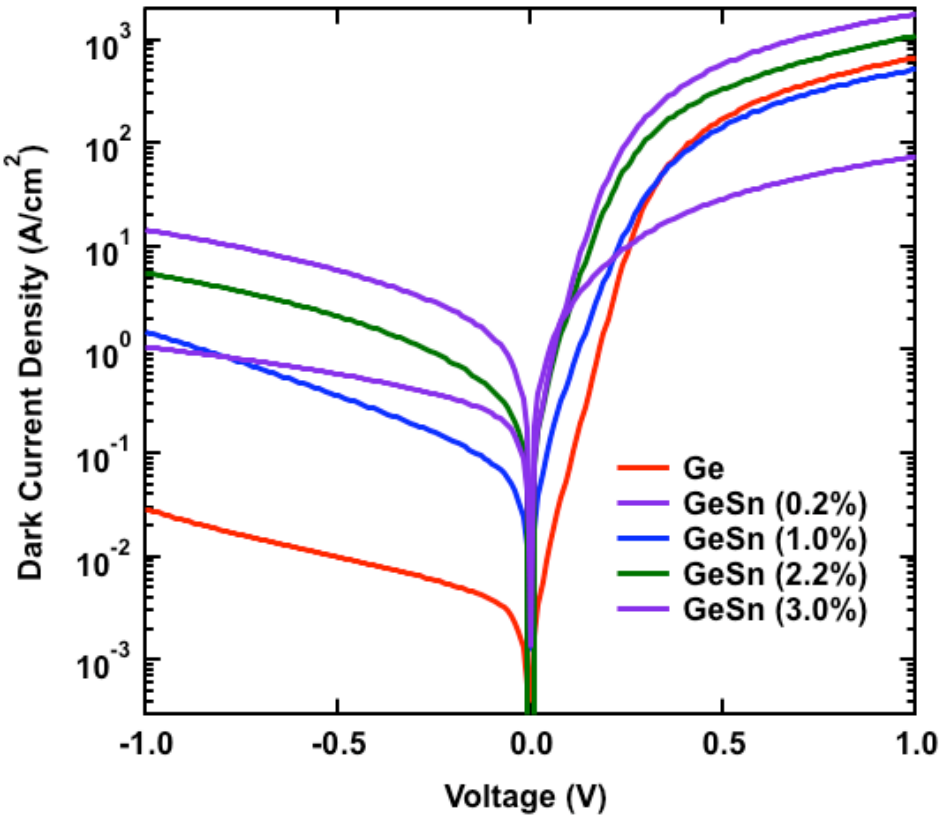

FIG. 42. Dark current densities obtained from 250 μm photodiodes with varying Sn content.

As we get to 1 % Sn, the magnitude of the dark current doesn't change much from the 0.2 % case, but the reverse current shows a larger slope in the log plot, indicating a departure from the ideal diode case. The ideality factor (1.5) indicates that recombination-generation in the space charge region is playing a large role in the dark current. At 2.2 % Sn, the current has increased two orders of magnitude relative to pure Ge. The ideality factor is 1.5, as for the 1% Sn diode. The activation energy of the saturation current has dropped even further, which could indicate a large tunneling component to the current. When the Sn content is increased to 3 %, the dark current increases even further, and the rectifying characteristics are seriously degraded. The ideality factor cannot be determined reliably, but it is estimated to be higher than that for the diodes fabricated from lower Sn content films.

The increase in dark current densities, changes in current generation mechanisms, and degradation of rectifying characteristics in the diodes with increasing Sn content could be due to an increase in the threading dislocation densities in the films. It should be noted that the background carrier concentrations for the pure Ge films are *n*-type, while those of the GeSn alloys are *p*-type, even in the 0.2 % Sn case. This could indicate that Sn substitution is creating electrically active defects that act as acceptors.

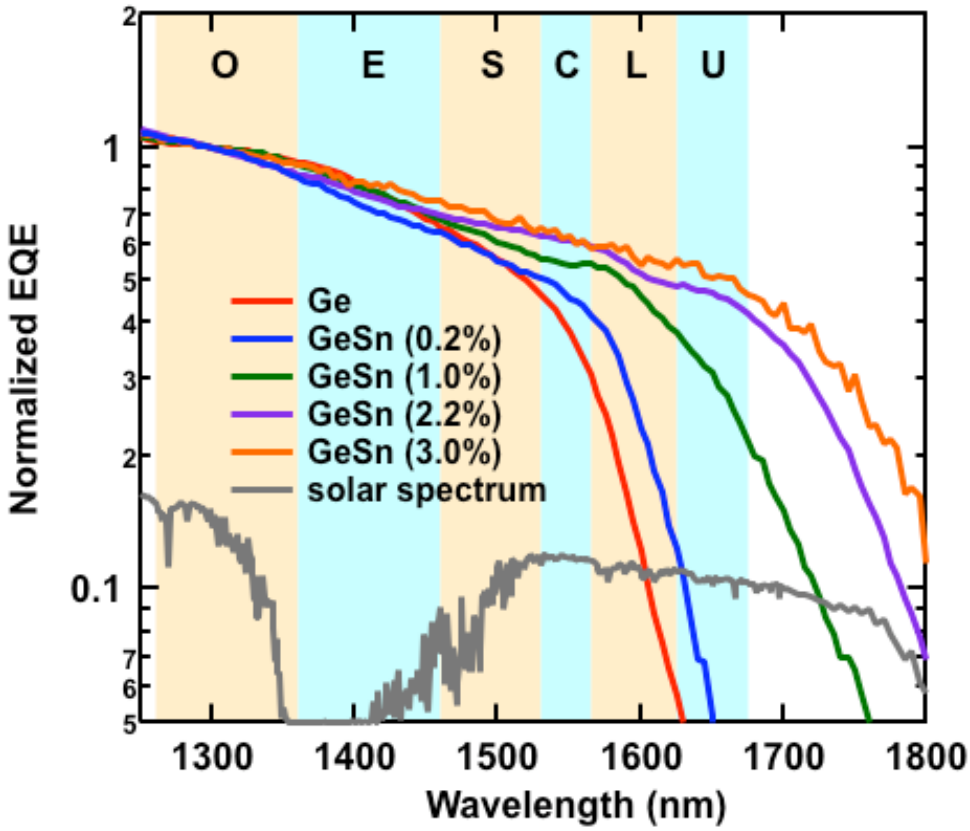

FIG. 43. EQE curves obtained from 300 μm diameter photodiodes with varying Sn concentration. Curves are normalized to response at 1300 nm for comparison. The wavelength ranges for the telecom bands are indicated, and the AM 1.5 solar spectrum is shown for comparison.

The optical response of the detectors can be compared by looking at the EQE curves normalized to their response at 1300 nm, as shown in FIG. 43. As the Sn content is increased, the detection edge of spectrum is shifted toward longer wavelengths. This is due to the strong compositional dependence of the direct band gap E_0. As Sn is incorporated into the Ge lattice, the direct gap drops rapidly, as evidenced by the clearly visible shift between the pure Ge and 0.2 % Sn curves. In fact, the addition of 0.2% Sn pushes the detection edge out to the C-band, which could make it viable for producing a high efficiency detector on Si for 1550 nm. The further shift in the detection edge

with increasing Sn content suggests that alloying with Sn could yield high efficiency detectors with tunable wavelength ranges to cover the desired telecom windows. The extended wavelength response of the detectors may also have significant implications for the design of novel photovoltaic devices, as shown in FIG. 43, since it makes it possible to capture a portion of the solar spectrum between 1400 nm and 1800 nm which is largely lost in current multijunction solar cells based on Ge as the low band gap component.

III. INVESTIGATION OF LIGHT EMISSION IN GE AND GESN FILMS GROWN ON SI

A. Room temperature photoluminescence in $Ge_{1-y}Sn_y$ films

1. Introduction

In this study, the optical properties of $Ge_{1-y}Sn_y$ films with $0 \leq y \leq 0.05$ were studied using photoluminescence spectroscopy at room temperature. The $Ge_{1-y}Sn_y$ layers, grown epitaxially on Si(100) substrates, were subjected to thermal treatment under ambient H_2 and their crystallinity was characterized through high-resolution X-ray diffraction measurements. Using this method, optimal annealing conditions for the films were determined. Room temperature photoluminescence measurements were then performed, and the corresponding peak values were determined via curve fitting. The results are compared with previous theoretical and experimental work on the compositional dependence of the direct and indirect band gaps in $Ge_{1-y}Sn_y$ alloys. Additionally, modeling of spontaneous emission was used to understand the effects of temperature, strain, and composition on the PL signal.

2. Materials and Methods

$Ge_{1-y}Sn_y$ films with thicknesses between 430 and 730 nm were grown directly on Si(100) substrates using ultra-high vacuum chemical vapor

deposition (UHV-CVD) reactions of Ge_2H_6 and SnD_4 at temperatures between 350 and 390 °C.[131] The Sn fraction in the alloy was controlled in the $0 \leq y \leq 0.04$ range by increasing the amount of SnD_4 in the gaseous mixture while systematically decreasing the deposition temperature to ensure full Sn substitution. Interestingly, the suppression of island growth remains effective even when ppm amounts of SnD_4 are admixed to the Ge_2H_6 gas, leading to extremely dilute alloys ($y \approx 0.0003$) that we use as a virtual Ge reference. In addition, we also study Ge films on Si grown by gas-source molecular beam epitaxy utilizing Ge_2H_6 with the $CH_2(GeH_3)_2$ metalorganic additive.

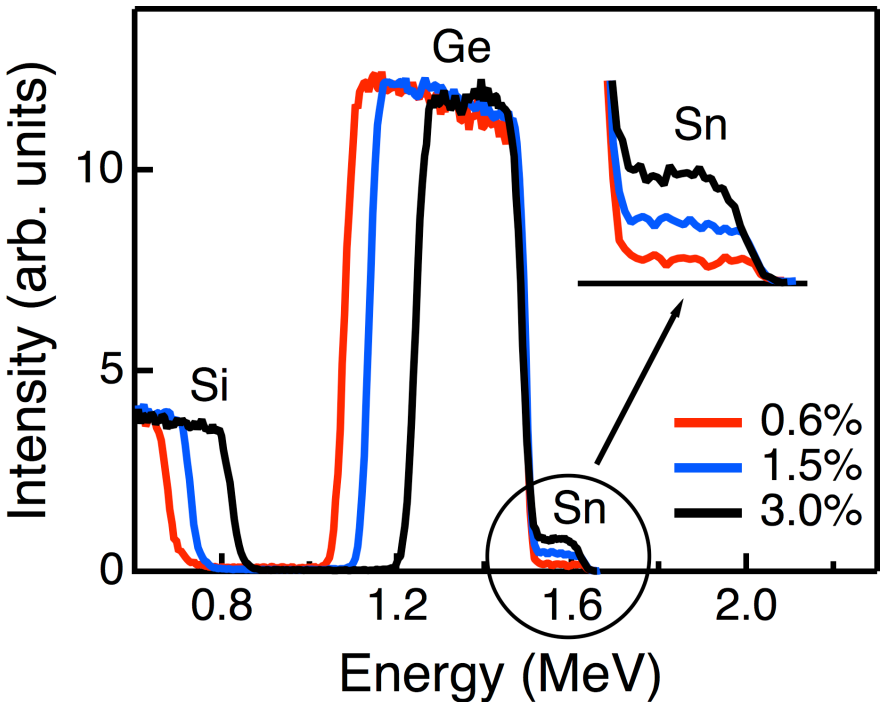

FIG. 44. Random RBS spectra of $Ge_{1-y}Sn_y$ films containing 0.6 (green), 1.5 (red) and 3.0 (black) % Sn and exhibiting thicknesses of 735 nm, 625 nm, and 450 nm, respectively. The inset is an enlarged view of the Sn signal shown as a shoulder adjacent to the main Ge peak.

After growth the samples are subject to three cycles of rapid thermal annealing (RTA) at temperatures between 350 and 750 °C and durations of 5-10 s each, depending on the sample (milder treatments for higher Sn concentrations). The RTA treatment reduces the levels of threading defects and relaxes the strain in the epitaxial layers. The Sn concentration in the alloy films is determined through Rutherford Back Scattering (RBS) experiments. Representative RBS spectra obtained from selected samples are shown in FIG. 44. The ratio χ_{min} of aligned over the random peak intensity is identical for the Ge and Sn channels in the spectra, indicating full substitutionality of the Sn atoms. The samples, presented in TABLE V, were prepared up to this point by R. T. Beeler.

TABLE V. List of growth methods, Sn contents (as measured by RBS), and thicknesses for the $Ge_{1-y}Sn_y$ films prepared for this experiment.

Sample ID	Growth method	Sn content (%)	Thickness (nm)
Ge98	LPCVD	0.0	430
Ge159	LPCVD	0.0	670
GeSn01	CVD	< 0.1	600
GeSn06	CVD	< 0.1	620
GeSn17	CVD	0.6	730
AFIT01	CVD	1.5	620
GeSn25	CVD	2.5	440
GeSn23	CVD	3.0	435
GeSn26	CVD	4.0	410

In my work, an additional heat treatment under hydrogen was adopted to passivate surface states as well as point defects and possibly dislocation boundaries. All samples were transferred into an annealing tube furnace,

pumped at 10^{-4} Torr and purged at room temperature with 20% ultrahigh purity H_2 diluted in argon. The pump/purge cycle was repeated three times after which the wafers were inserted into the hot zone and heated to temperatures up to 900 °C for 15 to 30 min under a constant stream of H_2:Ar at ambient pressure. After annealing, the samples were removed from the hot zone and allowed to cool in the tube with the H_2:Ar still flowing.

Upon removal from the tube furnace, high-resolution X-ray diffraction (HR-XRD) experiments were performed on the samples to determine the crystalline quality of the $Ge_{1-y}Sn_y$ films. $\theta/2\theta$ scans were used to measure the peak corresponding to the (004) reflection in the $Ge_{1-y}Sn_y$ layers, and ω-scans were done on this peak to measure the crystal mosaicity. These measurements were compared with those obtained on the same samples before annealing in H_2. Additionally, reciprocal space maps of the (224) reflections were used to determine the in-plane residual strain in the H_2-annealed layers. The HR-XRD measurements were performed by R. T. Beeler.

Room temperature photoluminescence (PL) experiments were performed using a 980 nm laser focused to a ~100 μm spot. The average power incident on the sample was 200 mW. A Horiba MicroHR grating spectrometer with 600 lines/mm and blaze wavelength 2 μm was used with a single-channel, LN_2-cooled extended InGaAs detector (1.3-2.3 μm range) to spectrally resolve and measure the PL signal. Further details of the experimental apparatus can be found in Appendix C.

3. Theory

We can model the emission from the $Ge_{1-y}Sn_y$ films in the following way. First, we start with the imaginary part of the dielectric function at zero temperature, ignoring the spin-orbit contribution and excluding excitonic effects, which is given by

$$\varepsilon_2 = \frac{4\sqrt{2}e^2P^2}{3m^2\hbar^3\omega^2}\left(\mu_{lh}^{3/2} + \mu_{hh}^{3/2}\right)\left(\hbar\omega - E_0\right)^{1/2}. \tag{59}$$

The dielectric function is related to the refractive index $N = n + ik$ by

$$N^2 = \left(n + ik\right)^2 = \varepsilon_1 + i\varepsilon_2, \tag{60}$$

from which we get

$$\varepsilon_2 = 2nk. \tag{61}$$

Now the absorption coefficient is related to the imaginary part of the refractive index by $\alpha = 2\omega/c$, so that we get

$$\alpha = \frac{\omega\varepsilon_2}{nc}. \tag{62}$$

Thus, our expression for the absorption coefficient becomes

$$\alpha_0 = \frac{4\sqrt{2}e^2P^2}{3m^2\hbar^3\omega nc}\left(\mu_{hh}^{3/2} + \mu_{lh}^{3/2}\right)\left(\hbar\omega - E_0\right)^{1/2}, \tag{63}$$

where we use the subscript "0" to emphasize that this expression corresponds to completely full valence bands and completely empty conduction bands at zero temperature. Now, we use the expression expression developed by Rosencher for the temperature dependent absorption $\alpha(\omega)$,

$$\alpha(\omega) = \alpha_0(\omega)\left[f_v(\hbar\omega) - f_c(\hbar\omega)\right], \tag{64}$$

where

$$f_v(\hbar\omega) = \frac{1}{1 + e^{\frac{E_v(\hbar\omega) - E_{Fv}}{kT}}} \tag{65}$$

is the probability that the valence band state is occupied by one electron. Here E_{Fv} is the quasi-Fermi level in the valence band. Similarly,

$$f_c(\hbar\omega) = \frac{1}{1 + e^{\frac{E_c(\hbar\omega) - E_{Fc}}{kT}}} \tag{66}$$

is the probability that the conduction and state is occupied by one electron. Here E_{Fc} is the quasi-Fermi level in the conduction band. Since we are assuming parabolic bands, the energies of the conduction and valence band are given by

$$E_c(\hbar\omega) = E_0 + \frac{\mu}{m_e}(\hbar\omega - E_0) \tag{67}$$

and

$$E_v(\hbar\omega) = -\frac{\mu}{m_h}(\hbar\omega - E_0), \tag{68}$$

respectively.

The electron-radiation Hamiltonian H_{eR}^{-} in second-quantization notation in the limit of infinite wavelength is

$$H_{eR}^{-} = \left(\frac{e}{m}\right)\left(\frac{2\pi\hbar}{Vn^2\omega}\right)^{1/2} \mathbf{e}_L \bullet \mathbf{p}\, a, \tag{69}$$

where a is the photon anhiliation operator and V is the volume. If we use Fermi's golden rule to calculate the transition rate per photon B_{vc}, we get

$$B_{vc} = \frac{2\pi}{\hbar}\left|H_{eR}^{-}\right|^2 \delta\left(\hbar\omega - E_c + E_v\right)$$

$$= \frac{2\pi}{\hbar}\left(\frac{e}{m}\right)^2\left(\frac{2\pi\hbar}{Vn^2\omega}\right)\left|\left\langle v\left|\mathbf{e}_L \bullet \mathbf{p}a\right|c\right\rangle\right|^2 \delta\left(\hbar\omega - E_c + E_v\right)$$

$$= \frac{4\pi^2 e^2}{Vm^2n^2\omega}\left|\left\langle v\left|\mathbf{e}_L \bullet \mathbf{p}a\right|c\right\rangle\right|^2 \delta\left(\hbar\omega - E_c + E_v\right). \tag{70}$$

If, for example, the light is linearly polarized along the *x*-axis, we need the p_x matrix element, but since we assume cubic symmetry, we take

$$\left|\left\langle c\left|\mathbf{e}_L \bullet \mathbf{p}a\right|v\right\rangle\right|^2 = \frac{1}{3}\left[\left|\left\langle c\left|p_x\right|v\right\rangle\right|^2 + \left|\left\langle c\left|p_y\right|v\right\rangle\right|^2 + \left|\left\langle c\left|p_z\right|v\right\rangle\right|^2\right] = \frac{P^2}{3} \tag{71}$$

If we substitute this into Eq. 70 and multiply by two to account for the light hole and heavy hole bands, we get

$$B_{vc} = \frac{8\pi^2 e^2 P^2}{3Vm^2n^2\omega}\delta\left(\hbar\omega - E_c + E_v\right). \tag{72}$$

If we have electromagnetic waves with a wide spectral distribution, the optical transition rate in s^{-1} is given by

$$g_{vc}(\mathbf{k}) = B_{vc} f_v\left(E_v\right)\left[1 - f_c\left(E_c\right)\right]\rho_{ph}\left(\hbar\omega\right), \tag{73}$$

where ρ_{ph} is the photon density per unit energy in the volume *V*. Clearly, the stimulated emission rate is given by

$$g_{cv}(\mathbf{k}) = B_{cv} f_c\left(E_c\right)\left[1 - f_v\left(E_v\right)\right]\rho_{ph}, \tag{74}$$

To this we must add the spontaneous emission rate, which is independent of the photon density and given by

$$g_{cv}^{spon}(\mathbf{k}) = A_{cv} f_c\left(E_c\right)\left[1 - f_v\left(E_v\right)\right], \tag{75}$$

In thermodynamic equilibrium, the photon distribution is[150]

$$\rho_{ph}(\hbar\omega) = \frac{n^3(\hbar\omega)^2}{\pi^2\hbar^3c^3}\frac{V}{\exp(\hbar\omega/kT)-1}. \tag{76}$$

But in thermodynamic equilibrium we must reach a stationary state such that

$$g_{vc}(\mathbf{k}) = g_{cv}(\mathbf{k}) + g_{cv}^{spon}(\mathbf{k}), \tag{77}$$

and

$$f_v(E) = f_c(E) = f(E), \tag{78}$$

or

$$\begin{aligned} B_{vc}f(E_v)\left[1-f(E_c)\right]\rho_{ph}(E_{vc}) = B_{cv}f(E_c)\left[1-f(E_v)\right]\rho_{ph}(E_{vc}) \\ +A_{cv}f(E_c)\left[1-f(E_v)\right], \end{aligned} \tag{79}$$

where we have used the delta function in Eq. 72 to substitute $\hbar\omega = E_c - E_v = E_{vc}$. Using Eq. 77 we can rewrite Eq. 80 as

$$\frac{n^3E_{vc}^2}{\pi^2\hbar^3c^3}\frac{V}{\exp(E_{vc}/kT)-1} = \frac{A_{cv}}{B_{cv}\exp(E_{vc}/kT)-B_{cv}}. \tag{80}$$

This is valid at all temperatures if and only if $B_{cv} = B_{vc}$, or

$$\frac{n^3E_{vc}^3}{\pi^2\hbar^3c^3}VB_{cv} = A_{cv}. \tag{81}$$

Of course, we used thermodynamic equilibrium to derive the relationships in Eq. 81, but since they represent an intrinsic property of the system, they remain valid in non-equilibrium situations. Using Eq. 72 we can write

$$A_{cv} = \frac{n^3E_{vc}^2}{\pi^2\hbar^3c^3}VB_{cv}$$

$$= \frac{n^3 E_{cv}^2}{\pi^2 \hbar^3 c^3} V \left(\frac{8e^2 P^2}{3} \right)$$
$$= \frac{8ne^2 P^2 E_{cv}^2}{3m^2 \hbar^3 c^3 \omega} = \frac{1}{\tau_R}. \tag{82}$$

where we have defined the radiative lifetime τ_R. Thus the direct band gap radiation lifetime is given by

$$\frac{1}{\tau_R} = \frac{8ne^2 P^2 E_0}{3m^2 \hbar^3 c^3}. \tag{83}$$

The spontaneous emission rate is given by the integration of Eq. 75 over the entire Brillouin zone,

$$R_{spon}(\hbar\omega) = 2\sum_{\mathbf{k}} \frac{1}{\tau_R(\mathbf{k})} f_c(\mathbf{k})\left[1 - f_v(\mathbf{k})\right]\delta\left(E_c - E_v - \hbar\omega\right). \tag{84}$$

Converting the discrete sum to an integral and performing the integration yields

$$R_{spon}(\hbar\omega) = \frac{1}{\tau_R(\hbar\omega)} \left(\frac{1}{2\pi^2} \right) \left(\frac{2\mu}{\hbar^2} \right)^{3/2} \left(\hbar\omega - E_0\right)^{1/2}$$
$$\times f_c\left[E_c(\hbar\omega)\right]\left\{1 - f_v\left[E_v(\hbar\omega)\right]\right\}. \tag{85}$$

And, using Eq. 82, we get

$$R_{spon}(\hbar\omega) = \frac{8ne^2P^2(\hbar\omega)^2}{3m^2\hbar^3c^3\omega}\left(\frac{1}{2\pi^2}\right)\left(\frac{2\mu}{\hbar^2}\right)(\hbar\omega - E_0)^{1/2}$$
$$\times f_c\left[E_c(\hbar\omega)\right]\left\{1 - f_v\left[E_v(\hbar\omega)\right]\right\}$$

$$= \frac{8\sqrt{2}ne^2P^2\mu^{3/2}\omega}{3m^2\hbar^4c^3\pi^2}(\hbar\omega - E_0)^{1/2}$$
$$\times f_c\left[E_c(\hbar\omega)\right]\left\{1 - f_v\left[E_v(\hbar\omega)\right]\right\}$$

$$= \left(\frac{n^2\omega^2}{\pi^2c^2\hbar}\right)\left[\frac{8\sqrt{2}e^2P^2}{3m^2\hbar^3\omega nc}\mu^{3/2}(\hbar\omega - E_0)^{1/2}\right]$$
$$\times f_c\left[E_c(\hbar\omega)\right]\left\{1 - f_v\left[E_v(\hbar\omega)\right]\right\}. \qquad (86)$$

Comparing this with Eq. 64, we can write

$$R_{spon}(\hbar\omega) = \left(\frac{n^2\omega^2}{\pi^2\hbar c^2}\right)\alpha(\hbar\omega)\frac{f_c\left[E_c(\hbar\omega)\right]\left\{1 - f_v\left[E_v(\hbar\omega)\right]\right\}}{f_v\left[E_v(\hbar\omega)\right] - f_c\left[E_c(\hbar\omega)\right]}. \qquad (87)$$

Somewhat lengthy but straightforward manipulation of the Fermi functions yields

$$R_{spon}(\hbar\omega) = \left(\frac{n^2\omega^2}{\pi^2\hbar c^2}\right)\alpha(\hbar\omega)\frac{1}{\exp\left[\frac{\hbar\omega - (E_{Fc} - E_{Fv})}{kT}\right] - 1}. \qquad (88)$$

Notice that this expression is *always* positive, as expected. The absorption becomes negative (gain) for $\hbar\omega < E_{Fc} - E_{Fv}$, but this is exactly compensated by the exp-1 term in the denominator of Eq. 88, which becomes negative for the same condition. If the photon frequency is much larger than the temperature (which is the case for our experiment), we get

$$R_{spon}(\hbar\omega) = \left(\frac{n^2\omega^2}{\pi^2\hbar c^2}\right)\alpha(\hbar\omega)\exp\left[\frac{(E_{Fc} - E_{Fv}) - \hbar\omega}{k_B T}\right]$$
$$= \left(\frac{n^2\omega^2}{\pi^2\hbar c^2}\right)\alpha(\hbar\omega)\exp\left[\frac{\Delta E_F - \hbar\omega}{kT}\right]. \quad (89)$$

where we have defined ΔE_F to be the difference in the quasi-Fermi levels of the conduction and valence bands.

Now that we have an expression for the emission rate in terms of the absorption coefficient, we can use the more complicated model for absorption developed in Chapter II, which takes into account excitonic effects. This should give us a more accurate model for the luminescence. While the calculated absorption is limited to the direct band gap, the conduction band minima at the *L*-point are fully taken into account for the computation of E_{Fc}. It should also be noted that strain is only taken into account in an approximate way, in that the lattice is assumed to be cubic. The effects of strain are added via the quasi-Fermi level calculations, but a more rigorous treatment would take into account the deviation from the cubic lattice symmetry.

4. Results and Discussion

(a) Annealing of GeSn films in H_2 ambient. The $Ge_{1-y}Sn_y$ films were annealed in the tube furnace under H_2 ambient for 15-60 minutes over a range of temperatures, which varied with the Sn concentration. In the case of the pure Ge films, the annealing temperatures were as high as 900 °C. In FIG.

45, we plot the results of the 2θ/ω scan of a $Ge_{0.975}Sn_{0.025}$ sample before and after annealing in H_2 ambient. We clearly see the (004) reflections of the GeSn and Si as distinct peaks. The peak position shifts slightly in the H_2-annealed sample with respect to the peak measured before annealing. This is most likely due to residual strain in the film. The strains were measured using (224) reciprocal space maps of the GeSn films and were found to be in the range 0.1-0.2%.

To the right of the GeSn peak, we see that there is a tail. This is due to alloying at the GeSn/Si interface. The alloying produces regions where the lattice parameter is slightly smaller than that of the GeSn film. This is most likely due to diffusion of Si into the GeSn layer, since the alloy at the interface is Ge-rich. The tailing in the (004) peak was observed in films annealed at temperatures of 750 °C and above. As the temperature is increased, the tail on the GeSn peak gets larger. Past some critical temperature, the GeSn films become unstable and will begin to decompose. An example of this is presented in FIG. 46, in the 2θ/ω scan from a $Ge_{0.96}Sn_{0.04}$ film that was taken past the critical temperature is shown.

Additional insight into the effects of the H_2-annealing can be obtained by comparing the ω rocking curves of the (004) peaks from the layers before and after annealing. The width of the peak corresponds to the spread in alignment of the crystal. The more narrow the peak, the more the crystal is aligned. It was found that annealing in H_2 tends to decrease the full-width

half-max (FWHM) of the peak, as shown in FIG. 47. This indicates that the crystallinity of the GeSn films is improved by H_2-annealing.

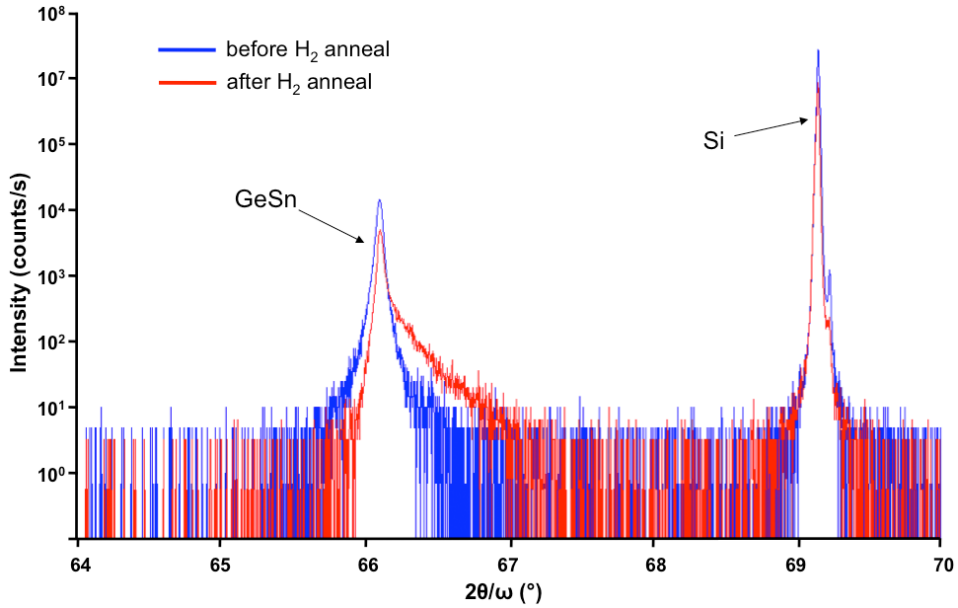

FIG. 45. Representative plot showing 2θ/ω scan of a GeSn film before and after annealing in H_2 ambient. The peaks corresponding to the (004) reflections in Si and GeSn are identified.

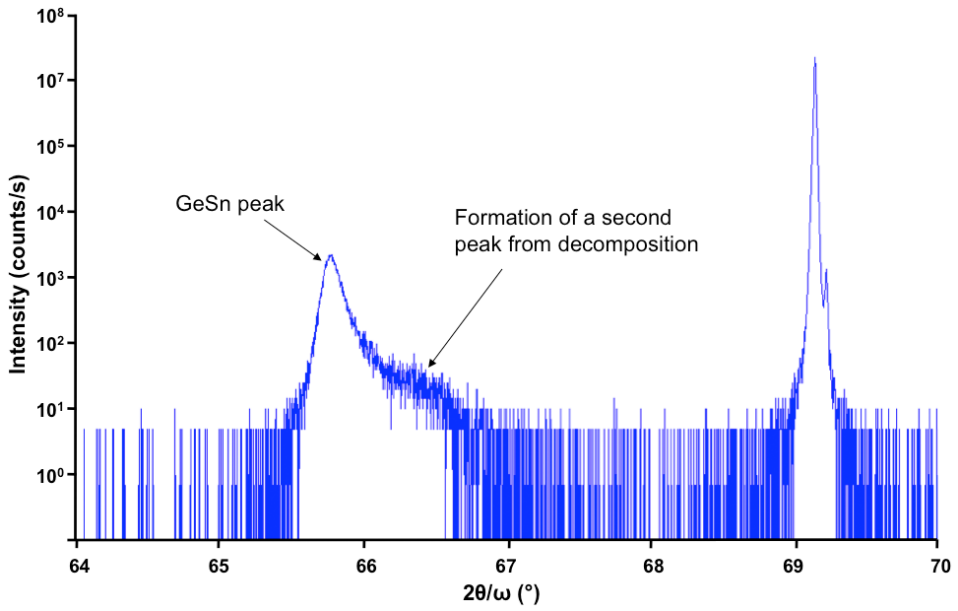

FIG. 46. Plot of 2θ/ω scan of $Ge_{0.96}Sn_{0.04}$ film after annealing past the critical temperature. The main GeSn peak is identified, along with a secondary peak due to decomposition of the layer.

The annealing time also had a minor effect. It was found that 30 minutes improved the crystallinity to a greater degree than 15 minutes, but that any extra time past 30 minutes did not make a significant difference. The optimal annealing temperatures and the measured strains in the films are shown in TABLE VI.

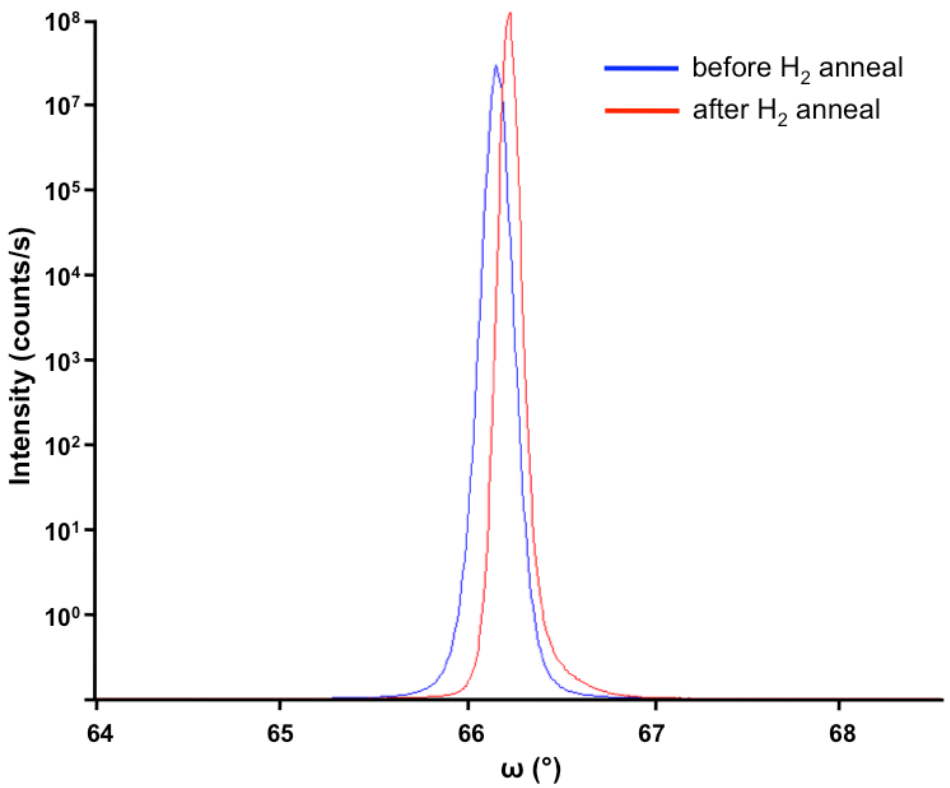

FIG. 47. Plot of ω rocking curve scan of peak from (004) reflection from a $Ge_{0.975}Sn_{0.025}$ film.

In order to verify that the H_2 environment was indeed having an effect, some annealing experiments were performed on pure Ge films under pure N_2 ambient. In these experiments, it was found that near the optimal H_2-annealing temperature, the surface of the Ge film annealed in N_2 became

discolored and the film was damaged. This indicates that the H_2 environment is instrumental in the annealing process.

TABLE VI. Sn concentrations, optimal annealing temperatures, and measured bi-axial tensile strains in the H_2-annealed $Ge_{1-y}Sn_y$ films.

Sample ID	Sn concentration (%)	Optimal annealing temperature (°C)	Tensile strain (%)
Ge98	0.0	825	0.19
Ge159	0.0	825	0.19
GeSn01	< 0.1	825	0.19
GeSn06	< 0.1	825	0.14
GeSn17	0.6	825	0.14
AFIT01	1.5	750	0.15
GeSn25	2.5	680	0.16
GeSn23	3.0	650	0.14
GeSn26	4.0	550	0.13

The use of high temperature annealing in H_2 has been previously shown to reduce threading dislocation densities[151,152] and improve the surface qualities[153] of Ge-on-Si films. The surface effects were explained by Nayfeh *et al.*,[153] who suggested that the hydrogen atoms tend to attach to Ge atoms and increase the Ge surface mobility by reducing the Ge diffusion barrier during annealing. However, our results seem to indicate that there is a bulk effect, rather than just surface passivation.

Hydrogen passivation of defects in Si has been observed under high-temperature annealing in H_2,[154] as well as through exposure to hydrogen plasma.[155] The similar behavior of Ge and Si with hydrogen suggests that the mechanism by which defect passivation occurs is the same in both materials.

Miller *et al.*[156] studied the role of hydrogen in Ge crystals through Raman spectroscopy. The authors found that there were hydrogen-induced platelets along the [111] direction, similar to those found in hydrogenated Si crystals. Thus, it is likely that the role of hydrogen passivation of defects in Ge is achieved by the same mechanism as in Si.

(b) Photoluminescence measurements. The PL spectra obtained from the $Ge_{1-y}Sn_y$ films are presented in FIG. 48. It should be noted that for each sample, the intensity increases upon H_2-annealing, but since the thermal treatment is not identical for all samples, the relative intensities may not reveal any intrinsic material property, and in fact we find that they fluctuate within one order of magnitude without any systematic dependence on y. Therefore the spectra are shown normalized to a single intensity for easier comparison. The main peak, with a full-width at half maximum (FWHM) of about 50-60 meV, shows a clear compositional dependence. For the pure Ge or extremely diluted $Ge_{1-y}Sn_y$ alloys, (collectively referred to as "Ge-films") it appears at 0.776±0.002 eV.

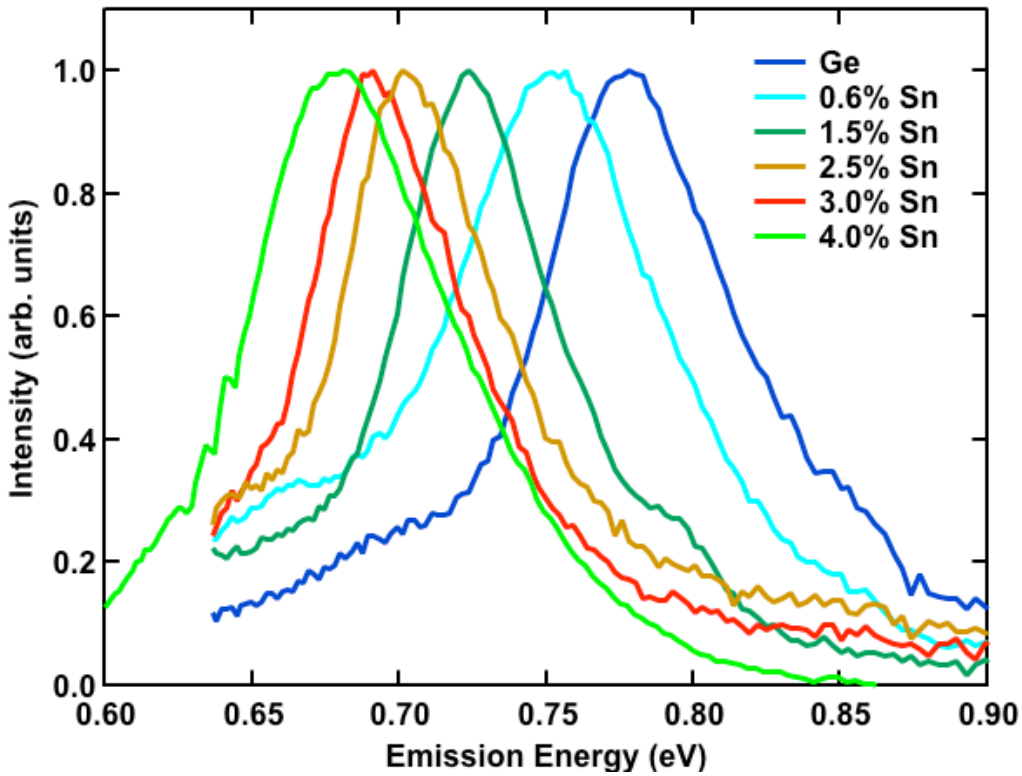

FIG. 48. Photoluminescence spectra obtained from $Ge_{1-y}Sn_y$ films under 400 mW illumination by 980 nm laser.

Measurements of bulk Ge samples were performed under identical experimental conditions for comparison, as shown in FIG. 49, and the results reveal a PL lineshape very similar to that reported in the literature,[70] with a high energy peak at 0.787 eV (FWHM = 45 meV) which corresponds to the direct gap E_0. Thus we also assign the main peak in our spectra to E_0. The small 11 meV difference between bulk and epitaxial Ge as well as the increased linewidth is perfectly consistent with the 7 meV and 23 meV downshift expected for transitions between the conduction band minimum at Γ and the heavy- and light-hole bands, respectively. The similarity of the PL linewidth between alloy and Ge-layers is quite surprising in view of the

fact that theoretical fits of the absorption coefficient in $Ge_{0.98}Sn_{0.02}$ require an additional Gaussian broadening of 70 meV. The result suggests that the states at the tails of the Gaussian distribution are "dark" in terms of their emission properties. The high-energy shoulder observed in most of the spectra in FIG. 48 has also been seen in *p*-type Ge samples and assigned to optical transitions that do not conserve crystal momentum.[15] An alternative explanation in our samples is direct-gap emission from the region close to the interface with the Si substrate, where Si intermixing would increase the E_0 energy.

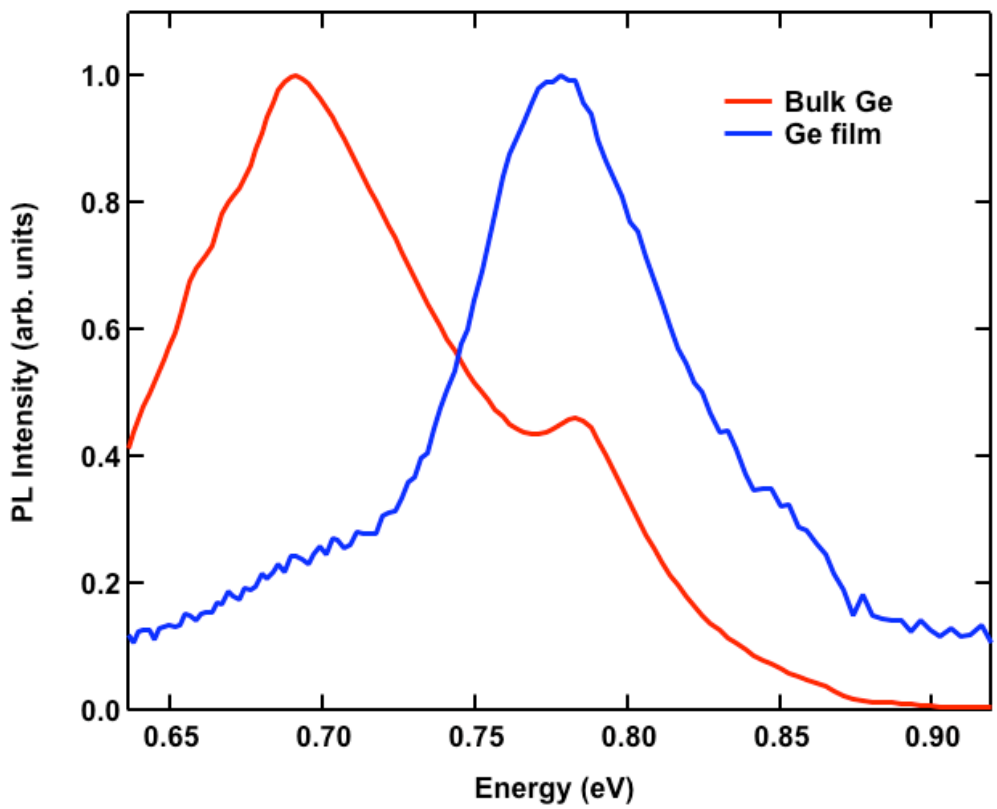

FIG. 49. Comparison of PL spectrum obtained from bulk Ge wafer with that obtained from a pure Ge film. The spectra are normalized to have the same maximum intensity.

A third weak peak at lower energy than the E_0 peak is apparent in most spectra. The peak appears at 0.703±0.002 eV in the Ge films. This is close to the indirect gap (E_{ind}) emission peak at 0.692 eV we observe in bulk Ge. We thus assign our weak low-energy peak to E_{ind} transitions. It should be pointed out, however, that the E_{ind} emission from bulk samples may not be directly comparable with the emission from thin films grown on Si substrates. In bulk Ge, the 95 meV separation between the direct and indirect emission peaks is significantly less than the 140 meV separation between the actual E_0 and E_{ind} gaps. This discrepancy reflects the complex structure of the indirect gap emission spectrum, which includes no-phonon as well as phonon-assisted transitions. The presence of defects such as misfit dislocations is likely to affect the relative weight of the no-phonon and phonon-assisted processes, so that the peak energy observed in epitaxial samples may not be directly comparable with the peak energy in the bulk. Moreover, while indirect gap emission is dominant in bulk samples, previous work on Ge-on-Si layers shows spectra that are completely dominated by the E_0 transitions. The reason for this is probably an increase in non-radiative recombination[161] combined with the lack of thermodynamic equilibrium between the electrons at the L- and Γ-valleys.[70] A quantitative theory, however, is lacking, and this makes it very difficult to extract the precise location of E_{ind} from spectral lineshapes such as those in FIG. 48. Nevertheless, the peak values were estimated using Gaussian curve fitting.

The energy value of the E_0 peak is plotted as a function of Sn concentration in FIG. 50. The compositional dependence of the direct band gap can be written as $E_0(y) = E_0^{Ge}(1-y) + E_0^{Sn}y - by(1-y)$, where E_0^{Ge} is the direct band gap in Ge, E_0^{Sn} the direct band gap in α-Sn, and *b* the so-called bowing parameter for the gap. If we fit the results in FIG. 50 with this expression, where E_0^{Sn} = -0.4 eV, and E_0^{Ge} and *b* are taken as adjustable parameters, we obtain *b* = 1.5 eV. However, if we exclude the sample with concentration *y* = 0.04, we obtain *b* = 1.8 eV, which is very close to the value *b* = 1.9 eV in Ref. 141. Moreover, if we exclude the samples with concentrations *y* > 0.02, we obtain *b* = 2.7 eV. This suggests a compositional-dependent bowing parameter, and implies that the quadratic form is not complex enough to describe the compositional dependence of the direct band gap. This behavior in the bowing parameter was seen in theoretical calculations by Yin *et al.*[157] and the large bowing was found to be due to a disordering effect.

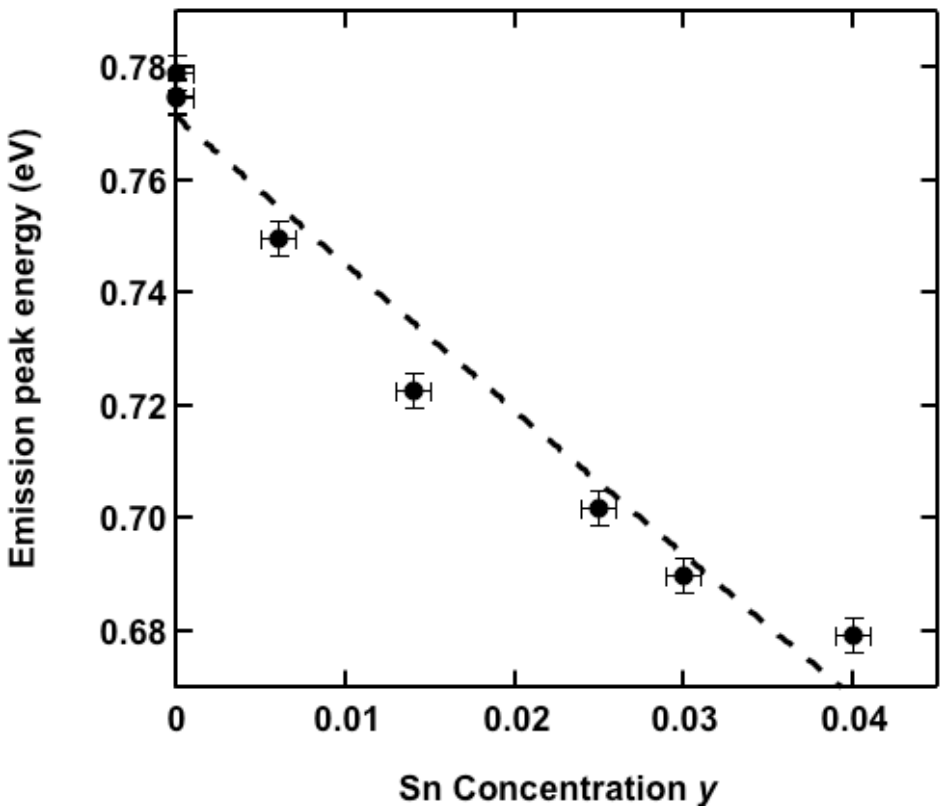

FIG. 50. Plot of emission energy of direct gap peaks from $Ge_{1-y}Sn_y$ films as a function of Sn concentration y. The solid line is a fit with a quadratic dependence constrained to yield the E_0 gap of α-Sn for y=1. From this fit, we obtain a quadratic bowing coefficient b=1.5 eV.

Since the band gap at the Γ-point is expected to drop faster than the band gap at the L-point, the separation between the peaks of the direct and indirect transitions should decrease as a function of y, and this appears to be confirmed by the measured results shown in FIG. 51. There is a general trend of decreasing separation with increasing Sn concentration, but there is a large uncertainty in the determination of the value of the peak energy for the indirect gap, so there is quite a bit of scatter in the plot. A line fit to the data predicts that the separation between the two peaks goes to zero at around y = 0.11. However, if we leave out the data point for y = 0.04, the fit predicts the

separation will go to zero at y = 0.09. These values are lower than those predicted by theory,[111,112] and agree reasonably well with other experimental results.[110]

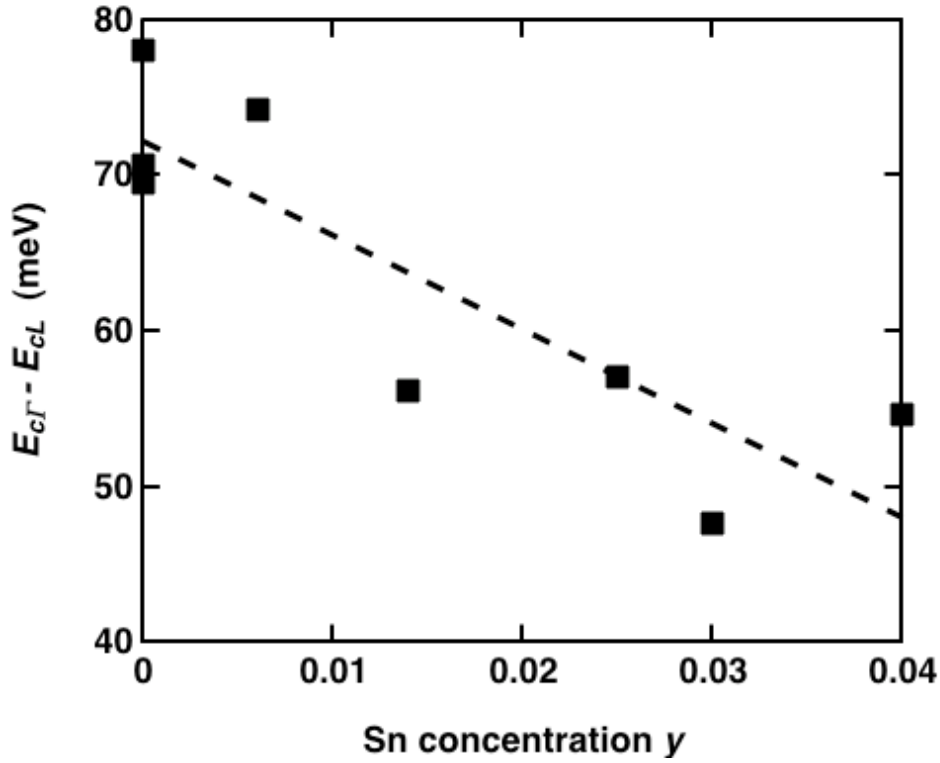

FIG. 51. Plot of energy separation between peaks assigned to the direct and indirect band gaps in $Ge_{1-y}Sn_y$ films as a function of Sn concentration y.

The direct gap emission spectra were also modeled using Eq. 89 and fit to the experimental spectra, as shown in FIG. 52. Since the expression only models the direct gap emission, the "fits" are somewhat qualitative. The fit is done by hand and we emphasize agreement on the high-energy side, which is less affected by the indirect edge. The Ge samples were fit first, using the temperature as an adjustable parameter to match the peak emission. Next, the GeSn samples were fit individually, using a fixed temperature taken as

the average of the Ge samples, and the bowing parameter *b* was adjusted until perfect agreement with the peak energy was achieved.

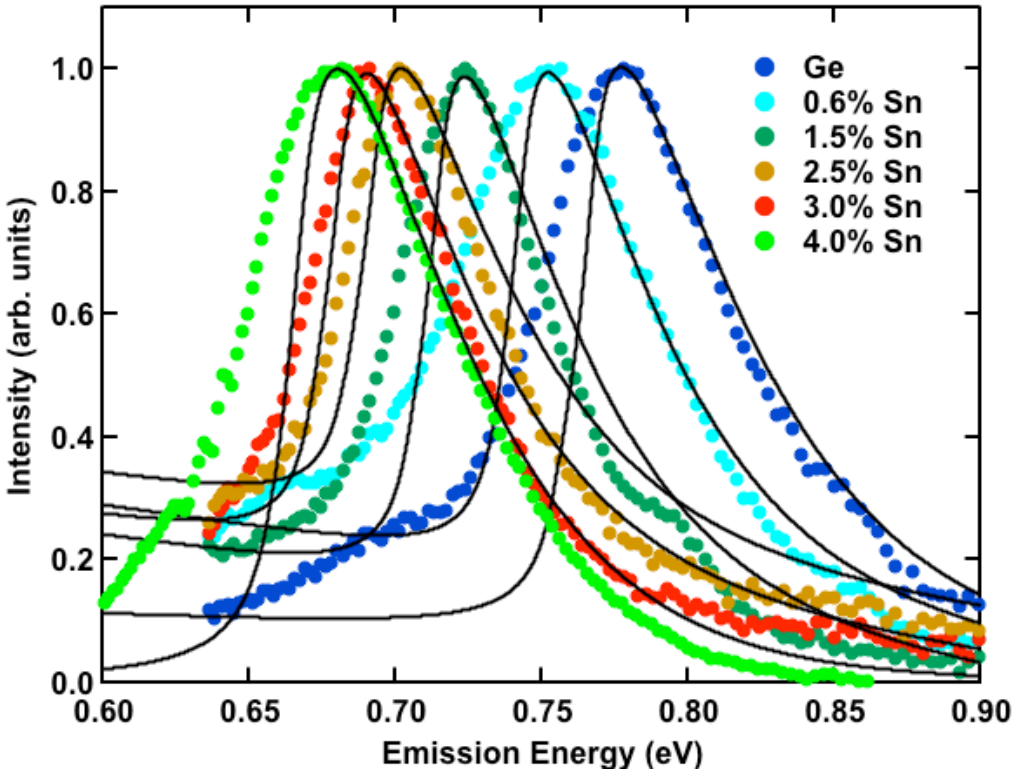

FIG. 52. The experimental PL spectra (markers) are compared with the fits (lines) obtained using the theoretical expression in Eq. 89.

As an example, we consider the spectrum obtained from the 4% Sn sample under 400 mW illumination power, as shown in FIG. 53. The fit to the pure Ge spectra under the same illumination power yielded an average temperature of 345 K. Using this temperature as a fixed value, we then fit the spectrum for the 4% Sn sample using the bowing parameter *b* as an adjustable parameter, until the peak value matches. A value of b = 1.5 eV

works well, and this is in agreement with the bowing parameter calculated from the fit in FIG. 50.

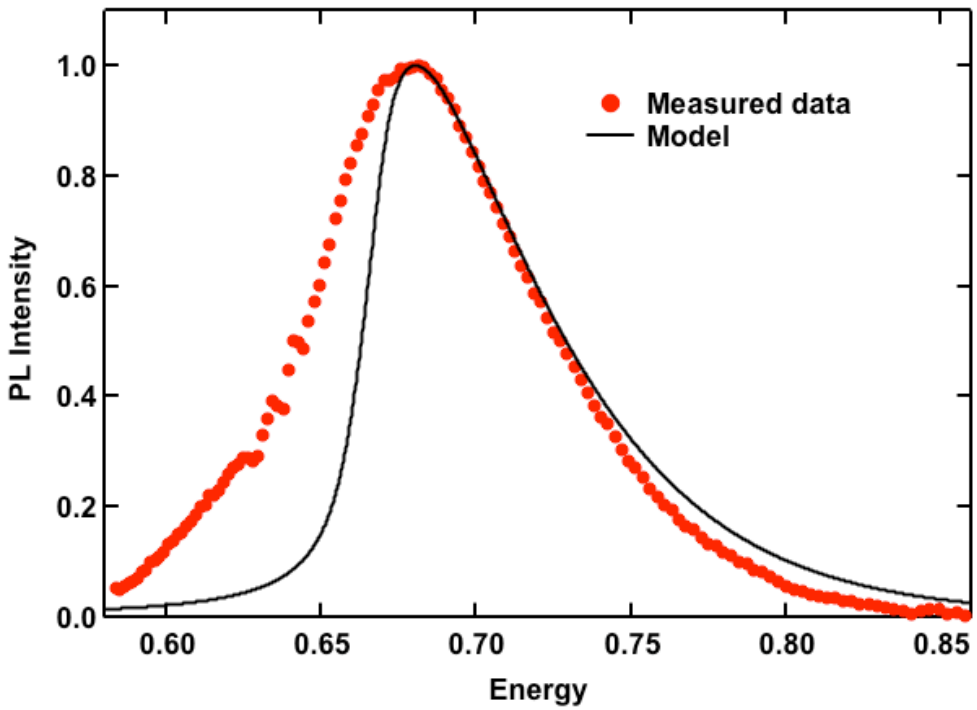

FIG. 53. Measured PL spectrum (red markers) and theoretical fit (black line) for 4% Sn sample under 400 mW illumination by 980 nm laser.

The main factor that affects the intensity of the fit is the carrier concentration. Of course, since we are photoexciting, the electron and hole concentrations are the same. In this case, I find good agreement with the high-energy lineshape for $n = p = 5\times10^{18}$ cm^{-3}. In all of the fits, which are presented with the experimental data in FIG. 52, the carrier concentration n was found to be in the 10^{18}-10^{19} cm^{-3} range.

Using the sample parameters and optical data for 2% GeSn, the amount of light absorbed in the layer should be approximately 40%. This should not

be very far off for 4% Sn, so we will take this as 0.4. The laser spot size is estimated to be 125 μm. With a thickness of 410 nm, this gives a volume of 5×10^{-9} cm^3. The carrier concentration is

$$n = \frac{G\tau}{V}, \tag{90}$$

where τ is the recombination lifetime and G is the electron-hole pair generation rate:

$$G = 0.4 \times \frac{P}{\hbar\omega}, \tag{91}$$

where P is the laser power. Combining these two equations, we get

$$\tau = \frac{(\hbar\omega)nV}{0.4P}, \tag{92}$$

If we insert values using an incident power of 400 mW, a photon wavelength of 980 nm, and the above-calculated volume, we obtain for n = 5×10^{18} cm^{-3} a value of τ = 30 ns. This value is several orders of magnitude shorter than the values found for undoped bulk Ge, but this could be accounted for by the higher carrier concentrations, which tend to decrease the lifetime.[158] The lower value could also be due to higher surface and interface recombination, as well as a higher density of defects, in the film relative to bulk Ge. In fact, the lifetime is not too far off the value of 5 ns found for the 2% Sn photoconductors in Chapter II. However, the films used in the PL experiments were grown later than those for the photoconductors, and the quality of the films has shown general improvement over that time.

The change from 5 ns to 30 ns might just be due to the different techniques involved, but if one wants to be optimistic, it might reflect the improvement in sample quality over time and the effect of the H2 annealing.

5. Conclusions

In summary, we have detected room-temperature photoluminescence from $Ge_{1-y}Sn_y$ alloys directly grown on Si substrates. The main luminescence peak is assigned to the E_0 gap of the alloy and displays a compositional dependence very similar to that of the E_0 gap obtained from spectroscopic ellipsometry experiments.[110] A weaker peak is assigned to the indirect gap transitions, and the separation between the direct and indirect emission appears to decrease as a function of the Sn-concentration y, as expected for these alloys. The tunable nature of the emission wavelength, the reduced separation between the direct and indirect minima in the conduction band, and the successful *p*- and *n*-type doping of these alloys[133] makes them an attractive alternative to pure Ge for laser devices grown on Si.

B. Electroluminescence from Ge and $Ge_{0.98}Sn_{0.02}$ *p-i-n* heterostructure diodes

1. Introduction

Luminescence from interband transitions occurs when electrons in the conduction band recombine with holes in the valence band and the excess energy is released as a photon. In the case of photoluminescence, the initial excitation of electrons into the conduction band occurs via absorption of photons. However, this is not the only way to excite the electrons across the gap. Consider a semiconductor *p-n* junction under forward bias. As current flows, minority carriers are injected across the depletion region, thereby promoting them to the higher energy state. In the case of Ge, this can populate both the L- and Γ-valleys, giving rise to both indirect and direct band edge luminescence, as described in Chapter I. In this study, electroluminescence from Si/Ge and Si/$Ge_{0.98}Sn_{0.02}$ *p-i-n* heterostructure photodiodes under forward bias was measured and analyzed.

2. Materials and Methods

The heterostructure diodes studied in this section were two of the photodiodes described in Chapter II. Schematics of the two devices are shown in FIG. 54. In both cases, nominally intrinsic $Ge_{1-y}Sn_y$ films were grown on *p*-type Si(100) wafers with resistivity ρ=0.01-0.02 Ω-cm. This layer was

capped by an *n*-type $Ge_{1-y}Sn_y$ layer, with addition of $P(GeH_3)_3$ as the source of the dopant P atoms. For y=0, the pure Ge films were grown using the low-pressure CVD method (described in Chapter I), based on mixtures of Ge_2H_6 and $(GeH_3)_2CH_2$, while the y=0.022 films were grown using the hot-wall CVD method (also described in Chapter I) with Ge_2H_6 and SnD_4. The thicknesses of the layers, doping concentrations, and values for residual tensile strain are listed in TABLE VII.

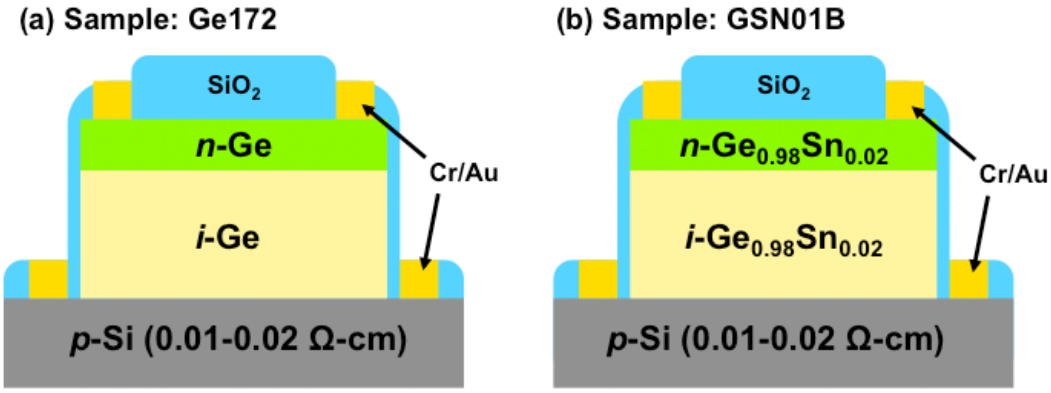

FIG. 54. Diagrams illustrating the structures of the (a) *p*-Si/*i*-Ge/*n*-Ge and (b) *p*-Si/*i*-GeSn/*n*-GeSn heterostructure diodes.

TABLE VII. List of Sn contents, thickness of intrinsic layers, thickness of and doping concentration in capping layers, and residual tensile strains (measured by HR-XRD) for the two heterostructures in this study.

Sample ID	Sn content (%)	Intrinsic layer thickness (nm)	Capping layer thickness (nm)	Concentration in capping layer (cm^{-3})	Tensile strain (%)
Ge172	0.000	900	90	2.5×10^{19}	0.17
GSN01B	0.022	350	60	1.0×10^{20}	0.12

Both samples were processed into circular mesa diodes with a diameter of 300 μm. The mesas were defined by lithography and processed by reactive ion etching using BCl_3 gas. Both contacts to the diode electrodes consist of Cr (20 nm)/Au (200 nm) layer stacks. The contact areas were patterned by lithography, the metals were deposited by electron beam evaporation, and the pads were finalized by liftoff. The final devices exhibited good rectifying diode characteristics. A full account of their fabrication process and a detailed analysis of their optical responsivity and I-V characteristics can be found in Chapter II.

The excitation of the diode devices for the EL measurements was provided by a stabilized current source. The light emitted from the devices was collected with a focusing lens (numerical aperture = 0.5), monochromatized by an f = 320 mm grating spectrometer, and detected with an extended LN-cooled InGaAs detector operating in the 1300-2300 nm range. The injection current source was pulsed to provide modulation for lock-in detection. Further details of the experimental apparatus can be found in Appendix C. The spectral dependence of the emission intensity was recorded at various magnitudes of current for each device.

3. Theory

The electroluminescence produced by the diodes can be modeled in the same way as the photoluminescence. The observed spectra can be modeled using the same generalized van Roosbroeck–Shockley expression[159] in Eq.

89. The absorption coefficient is modeled in exactly the same way as presented in Chapter III.

Using appropriate band structure parameters,[160] our model provides a convenient way to account for strain, composition, and temperature effects. While the calculated absorption is limited to the direct band gap, the conduction band minima at the *L*-point are fully taken into account for the computation of E_{Fc}. We assume that the emitted light originates from the nominally intrinsic layers, even though the highly *n*-doped cap layers might be expected to make an important contribution. However, surface recombination will reduce the light emission from these layers, and in fact we do not see PL associated with the *n*-layers of the *p*-*i*-*n* devices.

The emission intensity is taken as proportional to the intrinsic layer thickness, and with this assumption the experimental EL spectra for all measured currents and both samples can be fit simultaneously with the van Roosbroeck-Shockley equation, assuming that the carrier concentrations are proportional to the injection current and using as adjustable parameters an overall normalization factor, the value n_0 of the electron concentration at the lowest injection current for each diode, and the sample temperatures T_i at each current. Since the model does not account for indirect gap emission, we can fit only the peak and high-energy range of the direct gap emission. This avoids the spectral region where direct and indirect emissions overlap most noticeably. The correlation between the fit parameters n_0 and T_i is very low because the peak emission energy is essentially determined by T_i.

4. *Results and Discussion*

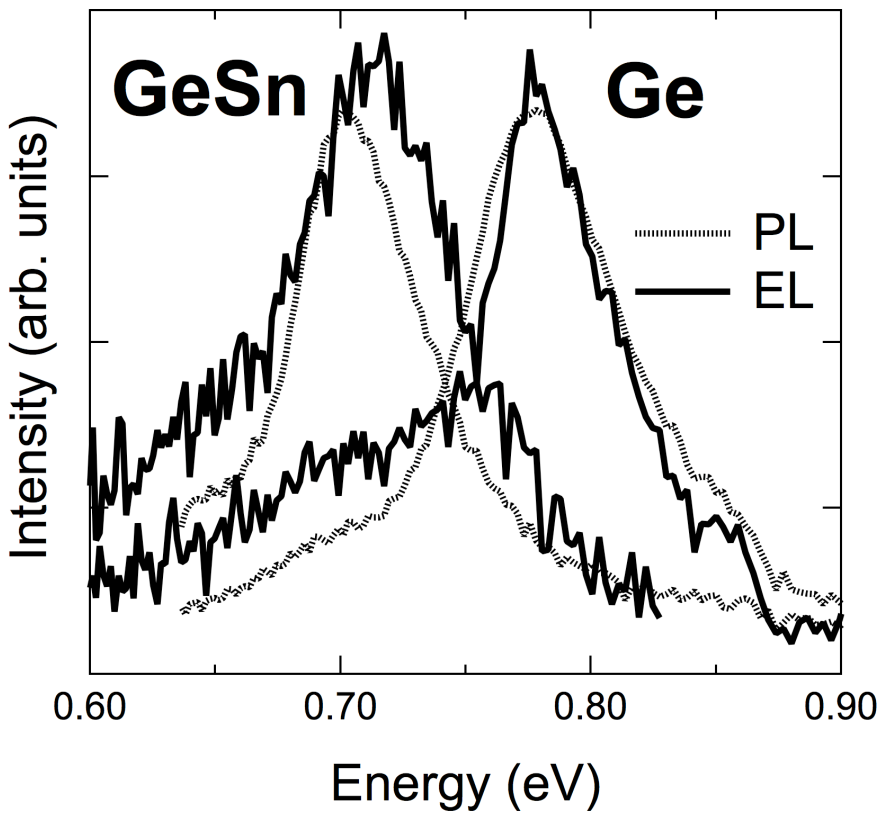

FIG. 55. Electroluminescence (EL) signal from the Ge and GeSn diode devices compared with room temperature photoluminescence (PL) spectra from similarly grown Ge and GeSn layers. For the EL spectra, the current density was 0.8 kA/cm^2 for the Ge device and 1.4 kA/cm^2 for the GeSn device. The PL spectra were obtained under 980 nm laser excitation. The relative scale of all spectra is arbitrary. The main emission peak is assigned to direct-gap transitions in all spectra.

FIG. 55 shows EL spectra at the lowest currents for which the signal was measured. These are compared with PL spectra from equivalent layers grown on Si using the same technique. The main peak is assigned to emission from the E_0 gap. In the pure Ge case, the peak energies from the EL and PL spectra are in excellent agreement. For the GeSn samples, there is a small relative shift, which is mainly due to the slightly higher (2.5% versus 2.2%)

Sn concentration in the PL sample. The shoulder on the low-energy side of the spectra is assigned to indirect gap transitions. We notice that the shoulder appears closer to the main peak in the GeSn samples, in agreement with the expected reduction of the direct-indirect separation as a function of the Sn concentration. The relative direct/indirect signal strength is larger in the PL experiments as compared with the EL measurements. This will be discussed below.

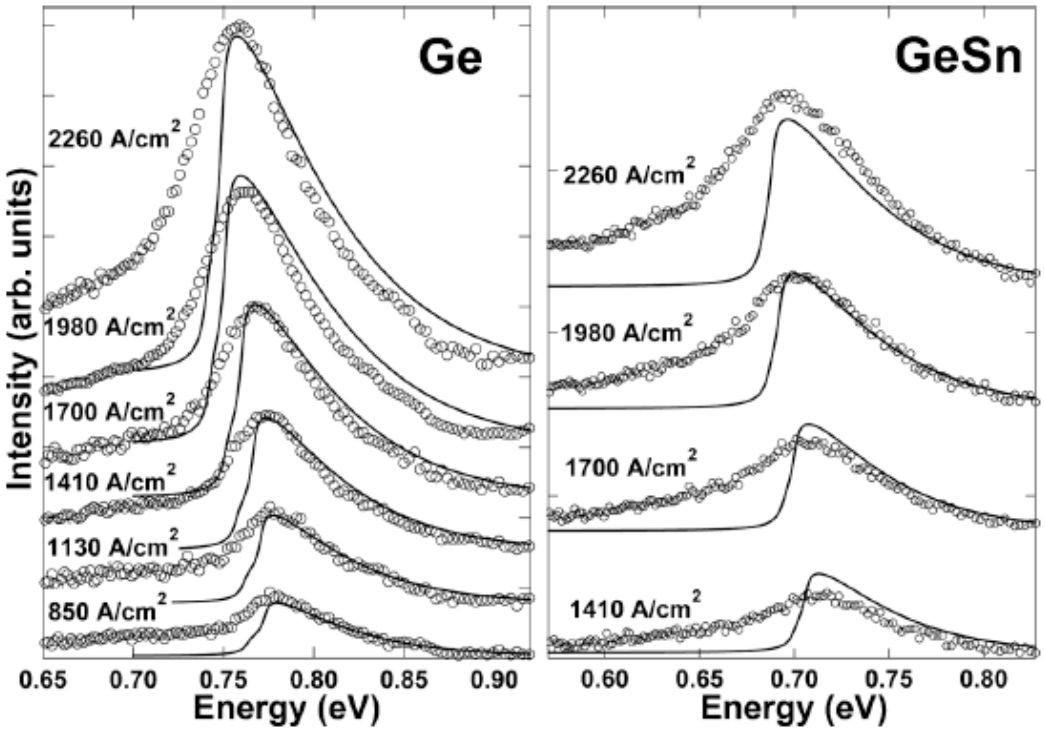

FIG. 56. (Left) Electroluminescence spectra from a Si/Ge heterostructure p-i-n diode as a function of the injection current density. (Right) Electroluminescence spectra from a $Si/Ge_{0.978}Sn_{0.022}$ heterostructure *p-i-n* diode as a function of the injection current density. The successive spectra have been shifted vertically for easy visualization. The solid lines represent a fit with Eq. 89. All spectra were fit simultaneously using a single normalization parameter.

The results of the fits of the PL data with Eq. 89 are shown as solid lines in FIG. 56. For the Ge diode we find a nearly perfect fit of the peak intensities for $n_0 = 1\times10^{19}$ cm^{-3} and a nearly perfect fit of the high-energy line shapes for $n_0 = 1\times10^{18}$ cm^{-3}. The curves shown correspond to $n_0 = 5\times10^{18}$ cm^{-3} at 0.85 kA/cm^2, which provides a good compromise. The device temperatures obtained from the fit are in the 330–380 K range. For the GeSn diode there is more ambiguity in the fit parameters because a change in temperature or composition could shift E_0 the same way. Also, the compositional dependence of the Γ-L separation is not known with certainty, and the range of injection currents is reduced with respect to the pure Ge diode. We obtain a good fit with $n_0 = 2.5\times10^{18}$ cm^{-3} at an injection current of 1.4 kA/cm^2, about three times less than in the Ge device. This suggests shorter nonradiative recombination lifetimes for the GeSn device, in qualitative agreement with its less optimal I-V characteristics, as discussed in Chapter II.

FIG. 56 (left) shows the injection current dependence on the EL spectra for the Ge diode and FIG. 56 (right) shows the corresponding data for the GeSn diode. For both devices, the signal intensity shows a superlinear behavior, as seen in FIG. 57. A similar superlinear behavior has already been reported in pure Ge diodes grown on Si substrates.[86,90]

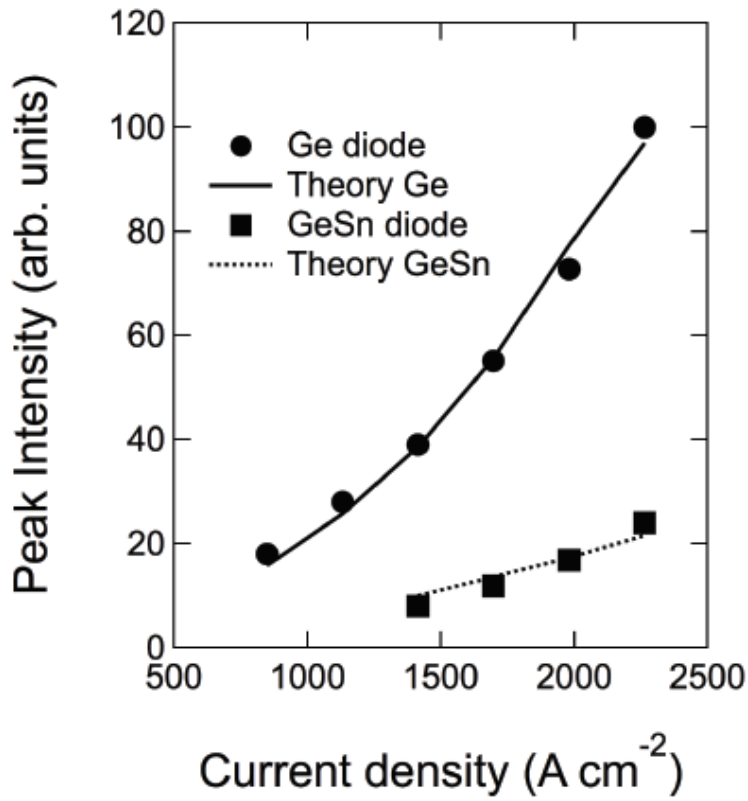

FIG. 57. Experimental electroluminescence peak intensities (markers) and corresponding theoretical predictions (lines) based on Eq. 89. The different emission intensities from the two samples are explained by their different thicknesses as well as by their different electron-hole concentrations at a given injection current.

The calculated intensities are also summarized in FIG. 57, and we see that the agreement with experiment is very good. Implicit in our modeling is the assumption of quasithermal equilibrium in the conduction band. Under these conditions there is a common quasi-Fermi level E_{Fc} for both the Γ- and L-valleys, and the calculated emission intensity is sensitive to their separation. For example, our model assumes that for y = 0.022, the Γ minimum is 82 meV above the L minimum.[160] If we keep this separation at 140 meV, as in pure Ge, a fit of the emitted intensities would require roughly the same electron concentration in both diodes at a given injection current.

This is less likely in view of the higher nonradiative recombination rates expected for GeSn. While this analysis is qualitative, the sensitivity to the Γ-*L* separation suggests that it may be possible to obtain the compositional dependence of this quantity from a comparison of the EL spectra of a series of $Ge_{1-y}Sn_y$ diodes with varying Sn concentrations.

Within the context of the quasiequilibrium model, the different ratios of direct/indirect emission intensities in the PL and EL experiments, as shown in FIG. 55, can only be explained by assuming a higher electron concentration in the PL samples. It is not clear, however, if a quasiequilibrium model can also explain the notorious differences between the emission from bulk Ge and the emission from Ge or GeSn layers on Si.[70,86,90] In the former, the indirect gap luminescence is much stronger relative to the direct gap luminescence than in the films. Moreover, earlier experiments in *p*-doped Ge showed that the ratio of indirect to direct PL intensity was affected by the excitation photon energy.[161] Different relative emission intensities were obtained if the photoexcited electrons were injected into the Γ- or *L*-valleys, which indicates a departure from quasiequilibrium. This, combined with the surprisingly good Γ-valley confinement observed in the quantum Stark effect experiments,[162] suggests that the intervalley relaxation times may not be much shorter than the characteristic recombination times in Ge, and therefore the quasiequilibrium approximation may break down. If this turns out to be the case, the modeling of the direct gap PL and EL in Ge and GeSn

devices would require a much more sophisticated approach that incorporates an explicit mechanism for intervalley electron transfers.

5. Conclusions

In summary, we have observed direct gap EL in p-i-n heterostructures with $Ge_{1-y}Sn_y$ active regions. The data are consistent with the reduction of the Γ-L separation expected on theoretical grounds and observed in PL experiments. The emission from both pure Ge and GeSn alloy samples can be understood in terms of the same model, suggesting the feasibility of electrical injection in devices based on GeSn layers with higher Sn concentrations and truly direct band gaps.

IV. CONCLUSIONS AND SUGGESTIONS FOR FURTHER WORK

This work presents several major results for GeSn alloys. First, processing protocols were developed and tested for fabrication of microelectronic devices from GeSn films grown on Si. These protocols were used to create photoconductors from GeSn, which represent the first GeSn devices ever produced. From these simple detectors, a large change in conductivity was observed under illumination. Furthermore, measurements taken at different wavelengths suggested that the material could show extended wavelength response relative to pure Ge.

Next, the first *p-i-n* type structures were produced from Ge and GeSn films with up to 4 % Sn, high efficiency photodetectors were fabricated and characterized, and the results were compared to understand the effect of Sn incorporation on the optoelectronic properties of Ge. The dark currents in the devices were found to increase monotonically with increasing Sn content in the films. This could be due to higher defect densities in the films, but it could also indicate some other conduction mechanism in GeSn relative to Ge. This is supported by the fact that the 0.2 % Sn devices show higher dark currents than those produced from pure Ge films, despite the fact that the crystallinity of the samples seems to be nearly equal.

The spectral response of the devices was found to be extended to wavelengths past the band gap of Ge, due to the decrease in both the direct and indirect band gaps in GeSn as a function of Sn content. This results in

detectors that are tunable over the telecom windows by incorporating Sn at appropriate concentrations. With just 2 % Sn, all of the telecom bands are covered by a single detector. Additionally, the 2 and 3 % Sn detectors cover a portion of the solar spectrum that is not captured by pure Ge, suggesting possible applications for photovoltaics.

The emission properties of GeSn films were studied at room temperature via photoluminescence measurements. A series of GeSn films with Sn content up to 4 % Sn were illuminated with an IR laser and found to exhibit direct band gap luminescence with tunable peak emission wavelength. This is the first known luminescence from thick GeSn films. The peak energy shifts to lower energy with increasing Sn content, due to the decrease in the direct band gap with increasing Sn in the films. Additionally, indirect band gap luminescence was observed, and the peak was also found to shift to lower energies with increasing Sn content. The separation between the emission energies of the direct and indirect peaks decreases with increasing Sn, and the data suggest a crossover from indirect to direct band gap material between 9 and 11 % Sn.

Further studies were performed via electroluminescence measurements on Si/Ge and Si/$Ge_{0.98}Sn_{0.02}$ *p-i-n* heterostructure diodes under forward bias. The diodes were found to exhibit luminescence with lineshapes and peak energies similar to those seen in the PL experiments. A significant shift between the emission peak energies of the two samples was

observed, due to the shift of the direct and indirect band gaps with Sn. These results represent the first electroluminescence observed in GeSn films.

The positive results obtained from these experiments represent a large step forward for GeSn materials, making them potentially viable for commercial applications in the future. We have essentially created photodetectors integrated on Si using CMOS-compatible processes. However, the high dark currents may limit their widespread use. This may be addressed through further studies of the conduction mechanism and defect levels in GeSn films. The defects are probably the key to understanding the electrical properties of GeSn, so they must be studied in detail. A good next step for the detectors would be to integrate them with Si waveguides. This is already being done with pure Ge detectors, so it should be feasible for GeSn, and it would represent a significant step towards optical interconnects.

The observance of luminescence via both optical and electrical pumping bodes well for the future of GeSn as an emitter. The Sn content needs to be increased, and a direct gap material needs to be realized. Furthermore, the films presented here could be used to create laser structures, such as the optically pumped Ge-on-Si laser produced at MIT. A logical next step is to try and recreate this laser without using the *n*-type doping. Relaxing the requirement for doping would make it more feasible for an electrically pumped laser to be produced. With integrated photodetectors already produced, and with LED's and lasers within grasp, the prospects for GeSn as a material for optoelectronics are indeed bright.

REFERENCES

[1] E. E. Haller, *Mat. Sci. Semicon. Proc.* **9**, 408 (2006).

[2] C. Claeys and E. Simoen, *Germanium-Based Technologies: From Materials to Devices* (Elsevier, Netherlands, 2007), pp. 1-6.

[3] "On the relationship of the properties of the elements to their atomic weights", D. I. Mendeleev.

[4] C. Winkler and J. Prak, *Chemie* **34**, 177 (1886).

[5] L. Hoddeson, E. Braun, J. Teichmann, and S. Weart, *Out of the Crystal Maze* (Oxford, New York, 1992), pp. 458-460.

[6] K. Lark-Horovitz, "Preparation of Semiconductors," National Defense Research Council report 14-585, 1945 (unpublished).

[7] E. C. Cornelius, *Electronics* **19**, 118 (1946).

[8] J. Bardeen and W. H. Brattain, *Phys. Rev.* **74**, 230 (1948).

[9] V. A. Johnson and H. Y. Fan, *Phys. Rev.* **79**, 899 (1950).

[10] H. Y. Fan, *Phys. Rev.* **78**, 808 (1950).

[11] G. L. Pearson and J. Bardeen, *Phys. Rev.* **75**, 865 (1949).

[12] C. Herring, *Phys. Rev.* **57**, 1169 (1940).

[13] F. Herman, *Phys. Rev.* **88**, 1210 (1952).

[14] F. Herman and J. Callaway, *Phys. Rev.* **89**, 518 (1953).

[15] F. Herman, *Phys. Rev.* **93**, 1214 (1954).

[16] F. Herman, P. IRE. 43, 1703 (1955).

[17] C. Kittel, Physica 20, 829 (1954).

[18] B. Lax, *Rev. Mod. Phys.* **30**, 122 (1958).

[19] G. Dresselhaus, A. F. Kip, and C. Kittel, *Phys. Rev.* **92**, 827 (1953).

[20] W. Shockley, *Phys. Rev.* **90**, 491 (1953).

[21] E. J. Ryder and W. Shockley, *Phys. Rev.* **75**, 310 (1948)

[22] J. N. Shive, *Phys. Rev.* **75**, 689 (1948).

[23] J. R. Haynes and W. Shockley, *Phys. Rev.* **75**, 691 (1949).

[24] W. H. Brattain and J. Bardeen, *Phys. Rev.* **74**, 231 (1948).

[25] W. Shockley, *Phys. Rev.* **78**, 294 (1950).

[26] W. Shockley and J. Bardeen, *Phys. Rev.* **77**, 407 (1950).

[27] G. L. Pearson, J. R. Haynes, and W. Shockley, *Phys. Rev.* **78**, 295 (1950).

[28] W. Shockley, *Electrons and Holes in Semiconductors* (D. van Nostrand Company, Canada, 1950).

[29] J. R. Haynes and W. Shockley, *Phys. Rev.* **81**, 835 (1951).

[30] H. Gummel and M. Lax, *Phys. Rev.* **97**, 1469 (1955).

[31] S. G. Kalashnikov, *J. Phys. Chem. Solids* **8**, 52 (1959).

[32] J. A. Burton, *Physica* **20**, 845 (1954).

[33] W. W. Tyler, *J. Phys. Chem. Solids* **8**, 59 (1959).

[34] J. Czochralski, *Z. Phys. Chemie* **92**, 219 (1918).

[35] G. K. Teal and J. B. Little, *Phys. Rev.* **78**, 647 (1950).

[36] G. K. Teal, M. Sparks, and E. Buehler, *Phys. Rev.* **81**, 637 (1951).

[37] F. S. Goucher, G. L. Pearson, M. Sparks, G. K. Teal, and W. Shockley, *Phys. Rev.* **81**, 637 (1951).

[38] W. Shockley, M. Sparks, and G. K. Teal, *Phys. Rev.* **83**, 151 (1951).

[39] J. Kilby, *IEEE T. Electron. Dev.* **ED-23**, 648 (1978).

[40] J. A. Hoerni, *IRE T. Electron. Dev.* **ED-8**, 178 (1961).

[41] K. Prabhakaran and T. Ogino, *Surf. Sci.* **325**, 263 (1995).

[42] W. H. Brattain and H. B. Briggs, *Phys. Rev.* **75**, 1705 (1949).

[43] K. Lark-Horovitz and K. W. Meissner, *Phys. Rev.* **76**, 1530 (1949).

[44] M. Becker and H. Y. Fan, *Phys. Rev.* **76**, 1530 (1949).

[45] M. Fox, *Optical Properties of Solids* (Oxford, New York, 2001), p. 63.

[46] M. Fox, *Optical Properties of Solids* (Oxford, New York, 2001), p. 64.

[47] S. Benzer, *Phys. Rev.* **72**, 1267 (1947).

[48] J. N. Shive, Phys. Rev.

[49] M. Becker and H. Y. Fan, Phys. Rev. 78, 301 (1950).

[50] J. A. Becker, *Electr. Eng.* **68**, 937 (1949).

[51] B. J. Rothlein and F. A. Stahl, *Sylvania Technologist* **3**, 8 (1950).

[52] W. Shockley, *Phys. Rev.* **78**, 294 (1950).

[53] F. S. Goucher, *Phys. Rev.* **78**, 816 (1950).

[54] K. Nishioka, T. Takamoto, T. Agui, M. Kaneiwa, Y. Uraoka, *Sol. Energ. Mat. Sol. C.* **90**, 1308 (2006).

[55] R. R. King, C. M. Fetzer, P. C. Colter, K. M. Edmondson, D. C. Law, A. P. Stavrides, H. Yoon, G. S. Kinsey, H. L. Cotal, J. H. Ermer, R. A. Sherif, K. Emery, W. Metzger, R. K. Ahrenkiel, and N. H. Karam, *Proceedings of the Third World Conference on Photovoltaic Energy Conversion* (Arisumi, Japan, 2003), p. 622.

[56] R. R. King, D. C. Law, K. M. Edmondson, C. M. Fetzer, G. S. Kinsey, H. Yoon, R. A. Sherif, and N. H. Karam, *Appl. Phys. Lett.* **90**, 183516 (2007).

[57] D. C. Law, R. R. King, H. Yoon, M. J. Archer, A. Boca, C. M. Fetzer, S. Mesropian, T. Isshiki, M. Hadda, K. M. Edmondson, D. Bhusark, J. Yen, R. A. Sherif, H. A. Atwater, and N. H. Karam, *Sol. Energ. Mat. Sol. C.* **94**, 1314 (2010).

[58] Z. S. Judkin, M.E. thesis, Massachusetts Institute of Technology, (2007).

[59] S. A. Ringel, C. L. Andre, M. Lueck, D. Isaacson, A. J. Pitera, E. A. Fitzgerald, and D. M. Wilt, *Mater. Res. Soc. Symp. P.* **836**, L6.2 (2004).

[60] R. Ginige, B. Corbett, M. Modreanu, C. Barrett, J. Hilgarth, G. Isella, D. Chrastina, and H. v. Känel, *Semicond. Sci. Technol.* **21**, 775 (2006).

[61] D. J. Aiken, *28th IEEE Photovoltaics Specialist Conference* (IEEE, New Jersey, 2000), p. 994.

[62] D. J. Friedman, and J. M. Olson, *Prog. Photovoltaics* **9**, 179 (2001).

[63] P. Espinet, I. Rey-Stolle, B. Galiana, M. Baudrit, and C. Algora, *2007 Spanish Conference on Electron Devices* (IEEE, New Jersey, 2007), p. 96.

[64] J.B. Tice, A.V.G. Chizmeshya, J. Tolle, and J. Kouvetakis, *Dalton Transactions* **39**, 4551 (2010).

[65] L. Colace, G. Masini, and G. Assanto, *IEEE J. Quantum Elect.* **35**, 1843 (1999).

[66] H.-C. Luan, D. R. Lim, K. K. Lee, K. M. Chen, J. G. Sandland, K. Wada, and L. C. Kimerling, *Appl. Phys. Lett.* **75**, 2909 (1999).

[67] R. A. Soref, *Nat. Photonics* **4**, 495 (2010).

[68] M. Morse, *Laser Focus World* **43**, 111 (2007).

[69] D. D. Cannon, J. Liu, Y. Ishikawa, K. Wada, D. T. Danielson, S. Jongthammanurak, J. Michel, and L. C. Kimerling, *Appl. Phys. Lett.* **84**, 906 (2004).

[70] T.-H. Cheng, K.-L. Peng, C.-Y. Ko, C.-Y. Chen, H.-S. Lan, Y.-R. Wu, C. W. Liu, and H.-H. Teng, *Appl. Phys. Lett.* **96**, 211108 (2010).

[71] Y. Ishikawa, K. Wada, J. Liu, D. D. Cannon, H.-C. Luan, J. Michel, and L. C. Kimerling, *J. Appl. Phys.* **98**, 013501 (2005).

[72] L. Colace, G. Masini, F. Galluzzi, G. Assanto, G. Capellini, L. Di Gaspare, E. Palange, and F. Evangelisti, *Appl. Phys. Lett.* **72**, 3175 (1998).

[73] D. Buca, S. Winnerl, S. Lenk, S. Mantl, and Ch. Buchal, *J. Appl. Phys.* **92**, 7599 (2002).

[74] J. Oh, S. K. Banerjee, and J. C. Campbell, *IEEE Photonic Tech. L.* **16**, 581 (2004).

[75] J. Liu, J. Michel, W. Giziewicz, D. Pan, K. Wada, D. D. Cannon, S. Jongthammanurak, D. T. Danielson, L. C. Kimerling, J. Chen, F. Ömer Ilday, F. X. Kärtner, and J. Yasaitis, *Appl. Phys. Lett.* **87**, 103501 (2005).

[76] L. Colace, M. Balbi, G. Masini, G. Assanto, H.-C. Luan, and L. C. Kimerling, *J. Lumin.* **121**, 413 (2006).

[77] S. Klinger, M. Berroth, M. Kaschel, M. Oehme, and E. Kaspar, *IEEE Photonic Tech. L.* **21**, 920 (2009).

[78] L. Colace, G. Masini, G. Assanto, H.-C. Luan, K. Wada, and L. C. Kimerling, *Appl. Phys. Lett.* **76**, 1231 (2000).

[79] J. Osmond, G. Isella, D. Chrastina, R. Kaufmann, M. Acciarri, and H. von Känel, *Appl. Phys. Lett.* **94**, 201106 (2009).

[80] O. I. Dosunmu, D. D. Cannon, M. K. Emsley, B. Ghyselen, J. Liu, L. C. Kimerling, and M. Selm Ünlü, *IEEE J. Sel. Top. Quant.* **10**, 694 (2004).

[81] T. Yin, R. Cohen, M. M. Morse, G. Sarid, Y. Chetrit, D. Rubin, and M. J. Paniccia, *Opt. Express* **15**, 13965 (2007).

[82] H. Zhai, Z. Zhang, L. Li, and S. Ma, *Opt. Quant. Electron.* **41**, (2009).

[83] X. Zheng, J. E. Cunningham, G. Li, Y. Luo, H. Thacker, J. Yao, R. Ho, J. Lexau, F. Liu, D. Patil, P. Amberg, N. Pinckney, P. Dong, D.Feng, M. Asghari, A. Mekis, T. Pinguet, K. Raj, and A. V. Krishnamoorthy, *Proc. SPIE* **7797**, 779702-1 (2010).

[84] G. Masini, S. Sahni, G. Capellini, J. Witzens, and C. Gunn, *Adv. Opt. Tech.* **2008**, 196572 (2008).

[85] M. Fox, *Optical Properties of Solids* (Oxfort, New York, 2001), p. 94.

[86] S.-L. Cheng, J. Lu, G. Shambat, H.-Y. Yu, K. Saraswat, J. Vuckovic, and Y. Nishi, *Opt. Express* **17**, 10019 (2009).

[87] R. A. Soref and L. Friedman, *Superlattice Mircrost.* **14**, 189 (1993).

[88] Y. Huo, H. Lin, R. Chen, M. Makarova, Y. Rong, M. Li, T. I. Kamins, J. Vuckovic, and J. S. Harris, *Appl. Phys. Lett.* **98**, 011111 (2011).

[89] G. Sun, H. H. Cheng, J. Menéndez, J. B. Khurgin, and R. A. Soref, *Appl. Phys. Lett.* **90**, 251105 (2007).

[90] X. Sun, J. Liu, J. Michel, and L. C. Kimerling, *Opt. Lett.* **34**, 1198 (2009).

[91] W. Hu, B. Cheng, C. Xue, H. Xue, S. Su, A. Bai, L. Luo, Y. Yu, and Q. Wang, *Appl. Phys. Lett.* **95**, 092102 (2009).

[92] J. Liu, X. Sun, R. Camacho-Aguilera, L. C. Kimerling, and J. Michel, *Opt. Lett.* **35**, 679 (2010).

[93] B. Y. Tsaur, J. C. C. Fan, and R. P. Gale, *Appl. Phys. Lett.* **38**, 176 (1981).

[94] B. Y. Tsaur, M. W. Geis, J. C. C. Fan, and R. P. Gale, *Appl. Phys. Lett.* **38**, 779 (1981).

[95] M. Garozzo, G. Conte, F. Evangelisti, and G. Vitali, *Appl. Phys. Lett.* **41**, 1070 (1982).

[96] J. C. Bean, T. T. Sheng, L. C. Feldman, A. T. Fiory, and R. T. Lynch, *Appl. Phys. Lett.* **44**, 102 (1983).

[97] J. A. Venables, *Introduction to Surface and Thin Film Processes* (University Press, Cambridge, 2000), p. 146.

[98] J. Michel, J. Liu, and L. C. Kimerling, *Nat. Photonics* **4**, 527 (2010).

[99] E. A. Fitzgerald, Y. H. Xie, M. L. Green, D. Brasen, A. R. Kortan, J. Michel, Y. J. Mii, and B. E. Weir, *Appl. Phys. Lett.* **59**, 811 (1991).

[100] F. Scarinci, M. Fiordelisi, R. Calarco, S.j Lagomarsino, L. Colace, G. Masini, G. Barucca, S. Coffa, and S. Spinella, *J. Vac. Sci. Tech.* **B** 16, 1754 (1998).

[101] M. T. Currie, S. B. Samavedam, T. A. Langdo, C. W. Leitz, and E. A. Fitzgerald, *Appl. Phys. Lett.* **98**, 1718 (1998).

[102] M. Wistey, Y-Y Fang, J. Tolle, A.V.G Chizmeshya, and J. Kouvetakis, *Appl. Phys. Lett.* **90**, 082108 (2007).

[103] Y-Y Fang, J. Tolle, Vijay D'Costa, Jose Menendez, A.V.G Chizmeshya and J. Kouvetakis, *Chem. Mater.* **19**, 5910 (2007).

[104] C. Weng, Ph.D. thesis, Arizona State University, 2010.

[105] *CRC Handbook of Chemistry and Physics*, 90th ed. (CRC Press, Boca Raton, 2009), p. 12-90.

[106] M. L. Lee, E. A. Fitzgerald, M. T. Bulsara, M. T. Currie, and A. Lochtefeld, *J. Appl. Phys.* **97**, 011101 (2005)

[107] S. Groves and W. Paul, *Phys. Rev. Lett.* **11**, 194 (1963).

[108] C. H. L. Goodman, *IEE Proc.* **129**, 189 (1982).

[109] G. He and H. A. Atwater, *Phys. Rev. Lett.* **79**, 1937 (1997).

[110] V. R. D'Costa, C. S. Cook, A. G. Birdwell, C. L. Littler, M. Cononico, S. Zollner, J. Kouvetakis, and J. Menéndez, *Phys. Rev. B* **73**, 125207 (2006).

[111] D. W. Jenkins and J. D. Dow, *Phys. Rev. B* **36**, 7994 (1987).

[112] K. A. Mäder, A. Baldereschi, and H. von Känel, *Solid State Commun.* **69**, 1123 (1989).

[113] G.-E. Chang, S.-W. Chang, and S. L. Chang, *IEEE J. Quant. Electron.* **46**, 1813 (2010).

[114] G. Sun, R. A. Soref, and H. H. Cheng, *Opt. Express* **18**, 19957 (2010).

[115] G. Sun, R. A. Soref, and H. H. Cheng, *J. Appl. Phys.* **108**, 033107 (2010).

[116] *CRC Handbook of Chemistry and Physics*, 90th ed. (CRC Press, Boca Raton, 2009), p. 12-80.

[117] S. Oguz, W. Paul, T. F. Deutsch, B.-Y. Tsaur, and D. V. Murphy, *Appl. Phys. Lett.* **43**, 848 (1983).

[118] H. Fukumoto, H. Myoren, T. Nakashita, T. Imura, and Y. Osaka, *Jpn. J. Appl. Phys.* **25**, 1312 (1986).

[119] I. Chambouleyron, F. C. Marques, J. P. de Souza, and I. J. R. Baumvol, *J. Appl. Phys.* **63**, 5596 (1988).

[120] I. T. H. Chang, B. Cantor, and A. G. Cullis, *J. Non-Cryst. Solids* **117-118**, 263 (1990).

[121] S. I. Shah, J. E. Greene, L. L. Abels, Q. Yao, and P. M. Raccah, *J. Cryst. Growth* **83**, 3 (1987).

[122] E. A. Fitzgerald, P. E. Freeland, M. T. Asom, W. P. Lowe, R. A. Macharrie, Jr., B. E. Weir, A. R. Kortan, F. A. Thiel, Y.-H. Xie, A. M. Sergent, S. L. Cooper, G. A. Thomas, and L. C. Kimerling, *J. Electron. Mater.* **20**, 489 (1991).

[123] W. Wegscheider, J. Olajos, U. Menczigar, W. Dondl, and G. Abstreiter, *J. Cryst. Growth* **123**, 75 (1992).

[124] A. Harwit, P. R. Pukite, J. Angilello, and S. S. Iyer, *Thin Solid Films* **184**, 395 (1990).

[125] M. E. Taylor, G. He, H. A. Atwater, and A. Polman, *J. Appl. Phys.* **80**, 4384 (1996).

[126] O. Gurdal, P. Desjardins, J. R. A. Carlssson, N. Taylor, H. H. Radamson, J.-E.

[127] G. He and H. A. Atwater, *Appl. Phys. Lett.* **68**, 664 (1996).

[128] R. Ragan and H. A. Atwater, *Appl. Phys. Lett.* **77**, 3418 (2000).

[129] S. Takeuchi, Y. Shimura, O. Nakatsuka, S. Zaima, M. Ogawa, and A. Sakai, *Appl. Phys. Lett.* **92**, 231916 (2008).

[130] J. Taraci, J. Tolle, J. Kouvetakis, M. R. McCartney, D. J. Smith, J. Menéndez, and M. A. Santana, *Appl. Phys. Lett.* **78**, 3607 (2001).

[131] M. Bauer, J. Taraci, J. Tolle, A. V. G. Chizmeshya, S. Zollner, D. J. Smith, J. Menéndez, C. Hu, and J. Kouvetakis, *Appl. Phys. Lett.* **81**, 2992 (2002).

[132] M. R. Bauer, C. S. Cook, P. Aella, J. Tolle, J. Kouvetakis, P. A. Crozier, A. V. G. Chizmeshya, D. J. Smith, and S. Zollner, *Appl. Phys. Lett.* **83**, 3489 (2003).

[133] J. Xie, J. Tolle, V. R. D'Costa, C. Weng, A. V. G. Chizmeshya, J. Menéndez, and J. Kouvetakis, *Solid State Electron.* **53**, 216 (2009).

[134] R. T. Tung, *Mat. Sci. Eng. R* **35**, 1 (2001).

[135] S. M. Sze and K. K. Ng, *Physics of Semiconductor Devices*, 3rd Ed. (Wiley, New Jersey, 2007), p. 136.

[136] A. Dimoulas, P. Tsipas, A. Sotoropoulos, and E. K. Evangelou, *Appl. Phys. Lett.* **89**, 252110 (2006).

[137] T. Nishimura, K. Kita, and A. Toriumi, *Appl. Phys. Lett.* **91**, 123123 (2007).

[138] R. R. Lieten, S. Degroote, M. Kuijk, and G. Borghs, *Appl. Phys. Lett.* **92**, 022106 (2008).

[139] S. M. Sze and K. K. Ng, *Physics of Semiconductor Devices*, 3rd Ed. (Wiley, New Jersey, 2007), pp. 94-98.

[140] J. S. C. Prentice, *J. Phys. D: Appl. Phys.* **33**, 3139 (2000).

[141] V. R. D'Costa, Y. Fang, J. Mathews, R. Roucka, J. Tolle, J. Menéndez, and J. Kouvetakis, *Semicond. Sci. Technol.* **24**, 115006 (2009).

[142] D. Suh, S. Kim, J. Joo, and G. Kim, *IEEE Photonics Tech. Lett.* **21**, 672 (2009).

[143] L. Colace, L. Balbi, G. Masini, G. Assanto, H.-C. Luan, and L. C. Kimerling, *Appl. Phys. Lett.* **88**, 101111 (2006).

[144] M. Jutzi, M. Berroth, G. Wohl, M. Oehme, and E. Kasper, *IEEE Photonics Tech. Lett.* **17**, 1510 (2005).

[145] J. Osmond, L. Vivien, J.-M. Fedeli, D. Marris-Morini, P. Crozat, J.-F. Damlencourt, E. Cassan, and Y. Lecunff, *Appl. Phys. Lett.* **95**, 151116 (2009).

[146] L. Colace and G. Assanto, *IEEE Photonics J.* **1**, 69 (2009).

[147] G. Masini, L. Colace, G. Assanto, H.-C. Luan, and L. C. Kimerling, *IEEE Trans. Electron. Dev.* **48**, 1092 (2001).

[148] V. Sorianello, A. Perna, L. Colace, G. Assanto, H.-C. Luan, and L. C. Kimerling, *Appl. Phys. Lett.* **93**, 111115 (2008).

[149] Z. Huang, J. Oh, S. K. Banerjee, and J. C. Campbell, *IEEE J. Quantum Electron.* **43**, 238 (2007).

[150] E. Rosencher and B. Vinter, *Optoelectronics* (Cambridge University Press, Cambridge, 2002), p. 307.

[151] D. Choi, Y. Ge, J. S. Harris, J. Cagnon, and S. Stemmer, *J. Cryst. Growth* **310**, 4273 (2008).

[152] H.-Y. Yu, J.-H. Park, A. K. Okyay, and K. C. Saraswat, *T. Electrochem. Soc.* **16**, 823 (2008).

[153] A. Nayfeh, C. O. Chui, K. C. Saraswat, and T. Yonehara, *Appl. Phys. Lett.* **85**, 2815 (2004).

[154] N. Sato and T. Yonehara, *Appl. Phys. Lett.* **65**, 1924 (1994).

[155] J. L. Benton, C. J. Doherty, S. D. Ferris, D. L. Flamm, L. C. Kimerling, and H. J. Leamy, *Appl. Phys. Lett.* **36**, 670 (1980).

[156] M. Hiller, E. V. Lavarov, and J. Weber, *Phys. Rev. B* **71**, 045208 (2005).

[157] W.-J. Yin, X.-G. Gong, and S.-H. Wei, *Phys. Rev. B* **78**, 161203(R) (2008).

[158] E. Gaubas, M. Bauza, A. Uleckas, and J. Vanhellemont, *Mat. Sci. Semicon. Proc.* **9**, 781 (2006).

[159] W. van Roosbroeck and W. Shockley, *Phys. Rev.* **94**, 1558 (1954).

[160] V. R. D'Costa, Y. Y. Fang, J. Tolle, J. Kouvetakis, and J. Menéndez, *Thin Solid Films* **518**, 2531 (2010).

[161] J. Wagner and L. Viña, *Phys. Rev. B* **30**, 7030 (1984).

[162] Y.-H. Kuo, Y. K. Lee, Y. Ge, S. Ren, J. E. Roth, T. I. Kamins, D. A. B. Miller, and J. S. Harris, *Nature* **437**, 1334 (2005).

APPENDIX A

FABRICATION AND PROCESSING PROTOCOLS

This appendix contains a description of the clean room processing protocols developed for fabrication of microelectronic devices from Ge and GeSn films grown on Si substrates. Some work was also done on SiGeSn films, and the fabrication protocols seemed to transfer well.

There are several sets of masks for producing different devices. We currently have masks for producing (a) photoconductors, (b) photodiodes, (c) metal-semiconductor-metal diodes, and (d) solar cells. Each set of masks consists of one mask for the mesa definition and one or two masks for the metal contacts. The only set with two metal masks is for the MSM devices, so that two different metals can be used on the two contacts.

The first step in the fabrication process is to deposit about 150 nm of SiO_2 to act as a protective coating during the subsequent processing. This layer is sacrificial – it will be completely stripped later. As such, its quality is not critical. There are two PECVD tools for deposition of SiO_2, the Plasmaquest and the Oxford 100. The Plasmaquest is an older tool that uses a He plasma. The SiO_2 is formed by flowing SiH_4 and N_2O through the plasma onto the wafer surface. The deposition rate is typically around 1 Å/s. The Oxford 100 uses a lower power N_2O plasma. SiH_4 flows through the plasma and onto the wafer surface. This produces much higher deposition rates (up to 20 Å/s) than the Plasmaquest. Prior to the deposition, the native oxide is removed by sonicating the wafer in methanol for 10 minutes, and then drying in N_2. Whenever possible, a small piece of bare Si is placed on the

sample holder with the wafer so that the oxide thickness can be measured easily.

Once the oxide is deposited, the wafer is ready for the first lithography step. Prior to spincoating, the wafer should be rinsed with acetone, methanol, and IPA, and then dried with N_2 to assure there are no particles on the wafer surface. The mesa definition has always been done using AZ3312 photoresist, which is a positive photoresist. It can get sharp features down to about 1 μm with proper care. The lithography recipe is below.

AZ3312 recipe

1. Clean wafer with acetone, methanol, and IPA. Dry with N_2.
2. Spincoat with HMDS. Spinner recipe: 500 rpm, 2 s ramp, 10 s spin; 3000 rpm, 5 s ramp, 30 s spin.
3. Spincoat with AZ3312. Spinner recipe: 500 rpm, 2 s ramp, 10 s spin; 3000 rpm, 5 s ramp, 30 s spin.
4. Bake on hot plate for 60 s at 100 °C.
5. Expose at 45 mJ/cm^2.
6. Develop in AZ300MIF for 50 s.
7. Rinse with DI water, dry with N_2.
8. Check features under microscope and develop for additional 5 or 10 s, if necessary.
9. Rinse with DI water, dry with N_2.
10. Bake on hot plate for 60 s at 110 °C

It is best to use the 4” chuck on the spinner and use low tack blue tape squares cut to the size of the chuck, unless you have an entire 4” wafer. Typically, we have processed irregularly shaped pieces of wafers. There are two tools for alignment and UV exposure – the EVG and the OAI. The OAI is my tool of choice, but either can be used. The first exposure, for defining the mesas, is relatively easy. Care must be taken to orient the wafer to maximize the number of usable devices and alignment marks. When using small wafer pieces on the OAI, it is best to use the blue tape on the 4” chuck. The 2” chuck does not level correctly, which causes problems with the exposure.

The development must be done with care. I usually check the wafer under the microscope after 50 s of development, and then do 5 or 10 s more if needed. If it needs more time, there will be colorful patterns in between the device mesas. The alignment marks are the smallest features on the mask, so they can be used to check the development. The features should be sharp. If the development goes too long, the features will be washed out.

Next, the SiO_2 must be etched away so that the GeSn can be exposed. This is accomplished by immersing the wafer in BOE (20:1 NH_4:HF). The etch rate is typically 40-60 nm/min. Three minutes is usually sufficient to remove the oxide. Care must be taken not to etch too long. This can cause what is known as undercutting. The SiO_2 starts to etch underneath the photoresist, degrading the quality of the features in the pattern. The SiO_2 color will change as it is etched away. Once it is gone, the areas between the device

mesas should be the color of the GeSn film. It is helpful have a piece of unprocessed wafer to compare at this point. If the colors match, then the SiO_2 is etched.

The GeSn material is etched using RIE in BCl_3 plasma. Over time, the results of this process have been inconsistent. Etch rates can be as low as a few nm/min or as high as 50 nm/min. Typically it is something like 30-40 nm/min. In most cases, I etched all the way down to Si, so the etch time was not important. In a few cases, I tried to hit precise target depths, but I found that the etch rates were not always reproducible, so I was unsuccessful. The etch depth can be measured using the Tencor profilometer, but the photoresist must be removed first, so no further etching can be performed. This makes it very difficult to etch precise depths. If you etch down to the Si, it will be apparent by the color. It will be the color of a bare Si substrate. A side-by-side comparison in the microscope is a good check.

In some cases, a black residue formed during the etching process. It is unclear why this developed. It could not be removed by any subsequent processing. We tried oxygen plasma, boiling Microstrip 2001, and a variety of other solvents. The Oxford 80 RIE tool has some issues. In particular, the MFC that controls the BCl_3 has problems maintaining the proper flow. It is typically low, which causes the etch process to be interrupted when it goes out of tolerance. This can only be avoided by ignoring the tolerance and setting the target flow to a higher value. It is possible that there is something

wrong with the MFC. It is also possible that there is something wrong with the BCl_3 gas source, as it seems to have unstable pressure.

Once the mesas are etched, the photoresist can be removed by immersing the wafer in acetone for several minutes. Rinse with methanol and IPA and dry with N_2. Any remaining photoresist residue can be removed in the Tegal asher. The wafer should be exposed to oxygen plasma at 100 W for 5 min. The device areas are now formed on the wafers, and they are ready for formation of metal contacts.

The next step is to coat the wafer with SiO_2 passivate the GeSn surfaces and form the antireflection coating. This oxide layer is more critical than the previous, so the quality of the oxide must be high. Prior to deposition, the surface should be hydrogen passivated by immersing the wafer in 1:20 HF (49%) in methanol. Rinse in methanol, dry in N_2 and place immediately in the PECVD chamber. The tool should be ready for the wafer before starting the hydrogen passivation so that the time the wafer is exposed to air is minimized. It helps to have two people to do this. The low deposition rate of the Plasmaquest seems to help the surface passivation. Devices with the oxide from the Oxford 100 have shown high amounts of current along the surfaces. I think this is due to the higher deposition rate of this tool as compared to the Plasmaquest. It should be possible to develop a recipe on the Oxford 100 that achieves the same deposition rate as the Plasmaquest. This should be done in the future, as the Oxford 100 is a cleaner tool.

The oxide thickness is chosen to minimize reflection of incident light from the device at a certain wavelength. However, many of the devices are used over a large wavelength range, so the thickness must be chosen carefully. We used 520 nm at first, and then switched to 420 nm since it gave better broadband antireflection. Later, we moved to 270 nm, which is ideal for 1550 nm light. The thickness must be determined prior to processing, and this is used as the target thickness for the second oxide deposition.

After the oxide has been deposited, the wafer is ready for the second photolithography step. Most of the metals masks require using image reversal, but the older photodiode masks do not. When doing image reversal, AZ5214 is the photoresist to use. It can resolve features down to 2 μm easily. 1 μm is supposedly achievable, but I have not seen it done successfully. AZ5214 seems to work very well for lift-off, and it is the preferred photoresist for this process. The recipe for using AZ5214 is below.

AZ5214 recipe

1. Clean wafer with acetone, methanol, and IPA. Dry with N_2.
2. Spincoat with HMDS. Spinner recipe: 500 rpm, 2 s ramp, 10 s spin; 4000 rpm, 5 s ramp, 30 s spin.
3. Spincoat with AZ5214. Spinner recipe: 500 rpm, 2 s ramp, 10 s spin; 4000 rpm, 5 s ramp, 30 s spin.
4. Bake on hot plate for 90 s at 95 °C.
5. Expose with mask at 50 mJ/cm^2.

6. Bake on hot plate for 60 s at 115 °C.
7. Expose without mask (flood exposure) at 200 mJ/cm^2.
8. Develop in AZ300MIF for 50 s.
9. Rinse with DI water, dry in N_2.
10. Check features under microscope and develop for additional 5 or 10 s, if necessary.
11. Rinse with DI water, dry in N_2.

If a positive photoresist must be used for lift-off, as is the case for the older photodiode masks, then AZ4330 must be used. AZ3312 is not thick enough (~1.4 μm) for an effective lift-off. AZ4330, which has a thickness of 4 μm using the recipe below, is better suited for this purpose.

AZ4330 recipe

1. Clean wafer with acetone, methanol, and IPA. Dry with N_2.
2. Spincoat with HMDS. Spinner recipe: 500 rpm, 2 s ramp, 10 s spin; 3000 rpm, 5 s ramp, 30 s spin.
3. Spincoat with AZ4330. Spinner recipe: 150 rpm, 2 s ramp, 2 s spin; 500 rpm, 2 s ramp, 5 s spin; 5000 rpm, 5 s ramp, 30 s spin.
   Bake on hot plate for 90 s at 95 °C.
4. Expose at 80 mJ/cm^2.
5. Develop in AZ300MIF for 50 s.
6. Rinse with DI water, dry with N_2.

7. Check features under microscope and develop for additional 5 or 10 s, if necessary.
8. Rinse with DI water, dry with N_2.
9. Bake in oven for 30 min at 80 °C

The alignment of the metal contact pattern to the device mesas is critical for producing working devices. For the photoconductors and solar cells, this is fairly easy to do, as there is much room for error in the mask design. The other devices have smaller tolerances and require precise alignment. When using small wafer pieces, this can be very difficult, as only one of the two microscope objectives can be used. This makes adjusting the rotation of the wafer relative to the mask very hard to do. I have found that it is best to start with a gap of 100 μm and do a course alignment. Next, move to 50 μm separation, focus on an alignment mark at the top left of the wafer, and adjust the position and rotation of the wafer to match the alignment as closely as possible. Move the microscope objective to an alignment mark on the same line, but on the right side of the wafer. Adjust the rotation, then the position. It is important to remember which way you rotated it. Keep going back and forth between the two opposite alignment marks, making small adjustments at each step. Once it is aligned as well as possible, move to the bottom of the wafer and do the same thing. Repeat as many times as necessary until all alignment marks look good everywhere on the wafer. This can be a tedious process, but this alignment is critical. If you are using both

microscope objectives simultaneously on a large wafer, this is very easy to do since you have two points of reference.

Misalignment of the metal contacts to the mesas can cause the devices to be shorted. This happens when the metal pad connects the top of the mesa to the substrate. On the older photodiode masks, this is especially true since the spacing between the contacts is so small. The newer photodiode masks have a little more tolerance, so they are a bit easier to align.

After the metal patterning is complete, the oxide must be etched away to expose the surfaces for subsequent deposition of metals. This is done using BOE, as for the previous oxide etch. Again, this etch is critical. If the oxide is not completely etched away from the contact area, there will be a barrier between the metal and the semiconductor. This will cause the contacts to not behave as intended. If the etch goes too long, the oxide starts to etch underneath the photoresist. This can cause the devices to be shorted. The etch depth can be checked via optical microscopy. When all of the oxide has been etched away, the surface should be the same color as the unprocessed sample.

Metal contacts are formed via electron beam evaporation at a base pressure of 3×10^{-6} Torr. Immediately prior to placement in the evaporation tool, the native oxide should be removed by immersing the wafer in BOE for 20 s. Ohmic contacts can be formed on highly doped ($\sim10^{19}$ cm^{-3}) Ge, GeSn, and Si by depositing 20 nm Cr, followed by 200 nm Au. These contacts should not need any annealing. If the semiconductor is not as highly doped, then

formation of Ohmic contacts can become difficult. On Si, one can typically form Ohmic contacts by evaporation of Al, followed by annealing at 400 °C for up to 30 min. However, Al does not form Ohmic contacts on most Ge and GeSn surfaces. For almost all our devices, there is only one type of metal contact, so this does not produce working devices. Accordingly, one should always use the lowest resistivity Si wafers possible, if an Ohmic contact will need to be formed on the Si.

Schottky contacts were only attempted on Ge or GeSn once. I deposited 50 nm amorphous Ge, followed by 200 nm Ag, when trying to fabricate a MSM device. The MSM requires two metal depositions and thus two lithography steps for metal patterning. The second pattern is formed while there is metal on the surface from the first contact. It was found that the Ag reacts with the photoresist, turning the metal contacts black. This situation can be avoided by depositing an additional layer of metal, such as Au. These contacts were found to be slightly rectifying, but they did not have adequate barrier heights to produce a reasonable device.

Evaporation of metals takes some practice to control the deposition rates. Al is particularly tricky, as it has a tendency to creep up the sides of the crucible. Use a FabMate crucible with Al or Al/Si(1%) whenever possible, as it has a special coating to help prevent this. The Al provided by the clean room uses the FabMate crucibles. Cr comes in small pieces and it never really melts in the crucible. It stays as individual pieces, which glow red when hot. It is important to burn off the oxidized surface of the Cr prior to opening the

shutter for the actual deposition. Deposition rate should be about 1-1.5 Å/s. Au will melt completely, and the deposition rate should not exceed 2 Å/s.

Lift-off is performed by immersing the wafer in acetone. This is usually done overnight, but may be done in just a few minutes. The acetone should dissolve the photoresist and allow the metal to peel off. It has a tendency to stick to the surface, but it can be removed by spraying with acetone repeatedly. Quick dips in an ultrasonic bath can also help, but you should not leave the wafer sonicating for extended periods of time. Once the metal is lifted off, the only metal on the wafer should be the contacts. This can be verified by optical microscopy. Finally, any remaining photoresist is removed by exposing the wafer to 200 W oxygen plasma for 5 min.

APPENDIX B

ELECTRO-OPTICAL DEVICE CHARACTERIZATION APPARATUS

This appendix contains a description of the measurement apparatus designed and used for the electrical and optical characterization of GeSn-based microelectronic devices presented in this dissertation. The system is capable of performing standard 2-point electrical measurements, as well as measuring the external quantum efficiency (EQE) of photodetectors in the range 0.8-1.8 μm.

The system is centered around a microprobe station with a chuck capable of mounting wafers up to 6". The probe station is enclosed in a large metal dark box in order to shield it from light and electrical noise. The chuck is connected to a vacuum pump so that the substrate can be can be held stationary. There are two electrical probes mounted on micropositioners. The probes have triaxial (triax) leads coming off of them, which connect to panel mount triax connectors on the dark box. There is a microscope with a CCD camera attached to the computer to aid in positioning the probes.

The triax cables are specially shielded for very low noise applications. These cables are similar to regular coaxial cables, but there is an extra conductor sleeve between the signal and ground. The center conductor is low impedance and carries the signal. The inner ring also carries the signal, but this lead is high impedance. Since the inner ring and center leads are at the same potential, there is no leakage between them. The outer ring is the ground. The high impedance signal lead does not carry a significant amount of current, so there is very little leakage between it and the ground. Thus, there is very little leakage between the signal and ground, and the

capacitance of the cable is drastically reduced. These cables were essential for making the quantum efficiency experiments work.

Electrical measurements are performed using a Keithley 2400 sourcemeter. The Keithley does not have triaxial connections. Instead, the two triaxial cables from the dark box are connected to a small box which then couples the signal into a single BNC connector. The Keithley is connected via a BNC cable. The Keithley is capable of simultaneously performing one source and one measure function. This can be any combination of current and voltage. Simple functions can be done from the Keithley front panel, but current-voltage measurements are typically done via a custom LabVIEW program written for this purpose.

Optical measurements require a more complicated setup. Illumination of devices is achieved via a halogen lamp connected to a spectrometer or discrete laser diodes coupled into a custom fiber optic cable that has been specially shaped on one end to focus the light to a small spot. The incident light is modulated by an optical chopper, and the device response is measured using a simple current-to-voltage converter circuit and a lock-in amplifier.

The lamp and spectrometer are both made by Spectral Products. The lamp is a 100 W high power tungsten-halogen (part number ASBN-W, replacement bulb part number ASBN-WB-100L), which is coupled to a grating spectrometer (part number CM110, serial number 22241). The exit slit of the spectrometer has a fiber coupling assembly so that the light can be

focused into the end of a fiber optic cable equipped with an SMA connector. The light is coupled into a 600 μm diameter fiber (Thorlabs part number M41L02), which is connected to a custom-made fiber bridge. The fiber bridge consists of a collimation lens, which creates a free space beam, followed by a focusing lens to couple into another fiber. There is a gap of about 4 inches in between so that the optical chopper and interference filters can be inserted. On the other side of the fiber bridge, the light is coupled back into a 50 μm diameter fiber that is goes into the dark box. The other end of the fiber is shaped such that it creates a spot with diameter ~5 μm at a working distance of only about 1 μm. The end of the fiber is held in place by a fiber chuck, which is connected to a micropositioner. The fiber tip can be seen in the microscope, and is positioned such that the spot is in the center of the device.

The power output from the fiber can be measured using a power meter (Newport part number 1931-C) with a Ge diode detector. There is a custom LabVIEW program (MC spectrum measurement.vi) set up for measuring the light power output as a function of wavelength. You input the starting and ending wavelengths and the step size (in nm). It sweeps through the specified range setting the wavelength on the spectrometer, and then reading the power from the power meter. The data are recorded in a tab-delimited text file with wavelength (in nm) and power (in W) as columns. When doing measurements in the IR, it is necessary to use a long pass filter to block unwanted harmonics from the light source. The power output delivered to

the device is typically around 1 μW when using the halogen and 975 nm long pass filter.

There are also several fiber-coupled laser diodes, which can be connected directly to the input on the fiber bridge. These discrete sources have much higher power output than the halogen. They are typically in the mW range. These do not require the long pass filter to be used. The diodes have variable power output, which can be controlled using a current source. The DC power supply (Agilent part number E3640A) is used in constant current mode for this purpose. When using the laser diodes, it is important to have the specifications handy, so that you never exceed the maximum current rating. If the current goes too high, it will destroy the diode.

Detection is accomplished by measuring the voltage across a resistor placed in series with the diode. A fixed bias is held across the series circuit. This circuit is hardwired into a metal box with 4 connections. The two triax connectors are for the electrical probes, while the two BNC connections go to the input on the lock-in amplifier and the Keithley sourcemeter. The Keithley is used to apply the bias voltage across the voltage divider circuit. The circuit is hardwired to reduce noise, but the resistor must be changed to fit the experimental parameters. Low resistance does not provide much gain, but it tends to reduce noise since Johnson noise increases with resistance. One must also be sure to keep the absolute voltage across the load resistor below 1 V, as that is the maximum input voltage for the lock-in amplifier. Responsivity of devices often increases with increasing bias voltage, but this

increases the dark current and absolute voltage across the load resistor, so this can affect the choice of load resistance. There is a balance between gain and noise while keeping the voltage at appropriate levels.

In principle, one could do this measurement without the use of a lock-in amplifier. You could measure the voltage across the load resistor with a multimeter before and after illumination. The difference in the voltage could then be used to calculate the photocurrent and EQE. However, the photocurrent is typically very small compared to the dark current, especially when a bias is applied, so the measurement has a very poor signal-to-noise ratio (SNR). By modulating the light with the optical chopper, an oscillating voltage signal is produced across the load resistor. This oscillating signal is measured by the lock-in, which is essentially a very narrow bandpass filter. Noise occurs at every frequency, so by only selecting a certain frequency, it is possible to drastically reduce the noise level, thereby increasing the SNR.

The lock-in measures the voltage using Fourier analysis. The input signal (voltage across the load resistor) and the reference signal (TTL signal supplied by the optical chopper is converted to a sine wave in the lock-in) have the same frequency, but are out of phase. The two signals are phase-shifted and multiplied together, then expanded in a Fourier series. The readout (R) of the lock-in is the coefficient on the Fourier component that is at the fundamental frequency. All other components are ignored, which removes most of the noise. The input signal is a square wave, while the reference signal is a sine wave. Using standard Fourier analysis, the change in

voltage across the load resistor ΔV_L is related to the voltage readout on the lock-in V_R by

$$\Delta V_L = \frac{\sqrt{2}\pi}{2} V_R . \tag{B1}$$

The photocurrent can then be calculated by

$$I_{ph} = \frac{\Delta V_L}{R_L} = \frac{\sqrt{2}\pi V_R}{2R_L} , \tag{B2}$$

where R_L is the load resistance. The responsivity $\Re$ is calculated by taking the ratio the photocurrent to incident light power.

The detection circuit is frequency dependent. It seems to work best at low frequencies, so I typically used 50 Hz. The lock-in has a button labeled SYNC FILTER, which should be used whenever the frequency is below 200 Hz. Also, the line filter will cut out frequencies near 60 Hz, so that should be used as well. The sensitivity should be set so that the highest measured value is just within range. You want to use as much gain as possible without going into overload. It helps if you know where the highest response will be, but this is not always predictable.

The lock-in takes some time to make a measurement. This time is determined by the time constant. This is essentially the time over which the signal is integrated. Longer time constants usually decrease noise, but past a certain point there is no improvement. The time constant has to be long enough that it captures a significant number of periods from the oscillating signal. There is also a significant delay in the response of the lock-in to

changes in the measurement. For instance, if the wavelength of the incident radiation is changed, the signal measured by the lock-in will change. Because of the filtering on the lock-in, there is significant capacitance on the input, so it takes several time constants for the lock-in reading to catch up. A good rule of thumb is to wait 5 time constants before taking a measurement. In the LabVIEW program that runs the spectral response measurement, there is a field titled "Set wavelength delay". This field is time the program waits after changing the wavelength on the spectrometer before measuring the value from the lock-in. Thus, it should always be at least 5 times the time constant. The time constants for EQE measurements on photodiodes are typically 3 or 10 s.

The spectrometer, lock-in, and sourcemeter are all connected to the computer and controlled via a custom LabVIEW program (spectral response measurement.vi). The program needs as an input the file which contains two tab-delimited columns. The first column is the wavelength (in nm), and the second column is the incident power (in W). This input data is put into an array, and the wavelength column determines at which wavelengths the responsivity will be measured. At each wavelength specified in the file, the voltage from the lock-in is read, and the photocurrent and responsivity are calculated. The wavelength (in nm), incident power (in W), lock-in voltage (in V), photocurrent (in A), and responsivity (in A/W) are recorded as columns in a tab-delimited text file whose name and location are input by the user. This file can then be imported into a spreadsheet program for data analysis.

The system is also capable of measuring the responsivity as a function of bias voltage using a custom LabVIEW program (Response vs. bias measurement.vi). The wavelength and intensity of the incident light are held constant, and the bias voltage across the detector circuit is swept, measuring the responsivity at each voltage. The data are recorded in a tab-delimited text file with voltage (in V) and responsivity (A/W) as columns. This measurement is best performed using one of the laser diode sources. 1300 and 1550 nm are common wavelengths for telecommunications and are used for comparison in the literature. The higher intensity of the laser diode source produces a higher SNR, which means the time constants can be reduced.

The spectrometer also has its own software called CM-B. It was written in LabVIEW by the manufacturer of the spectrometer. It can be used to move the spectrometer to a certain wavelength, change gratings, or perform calibrations. LabVIEW cannot be open at the same time as CM-B. If they are both open, the computer can go to blue screen and all data is lost. This is because of the way CM-B communicates with the spectrometer via the RS-232 port. It seems to leave the connection open all the time, so if another program tries to access that port, there is a hardware conflict and the system shuts down.

APPENDIX C

ROOM TEMPERATURE PHOTOLUMINESCENCE AND ELECTROLUMINESCENCE MEASUREMENT APPARATUS

This appendix contains a description of the apparatus designed and used for measurement of near-IR (0.8-2.3 μm range) photoluminescence (PL) and electroluminescence (EL) from GeSn materials and devices. This system is designed to measure small amounts of luminescence. It maximizes the amount of light collected, while sacrificing on wavelength resolution. Thus, the peaks tend to be broad. This is not a problem for our application, since band edge luminescence is typically very broad anyway.

The wafer is prepared for the experiment by mounting it to a glass slide using rubber cement. The wafer is placed on the slide first, and then tiny dabs of rubber cement are put on the corners. This minimizes the stress put on the wafer during temperature changes. The laser tends to heat the sample some, so this could have a small effect. The glass slide is mounted to a stage using double-sided tape. The stage has vertical and horizontal tilt adjustment knobs and is mounted on a pole that can slide along a rail.

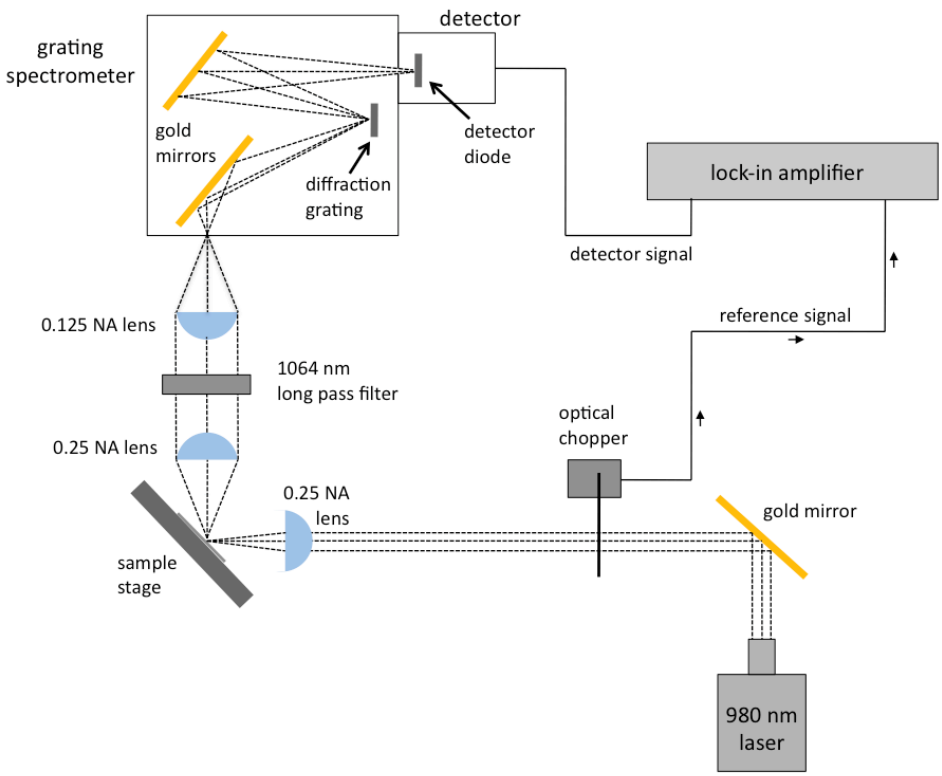

FIG. C1. Schematic of photoluminescence measurement system.

A schematic of the PL system is presented in FIG. C1. A 980 nm solid-state laser (OEM systems) with power up to 400 mW is used as the excitation source. It puts out a collimated square beam about 3 mm in width. It has a dedicated power supply that supplies constant current. The power output of the laser can be measured using the smaller power meter (Newport part number 1916-R) with the thermopile detector (Newport part number 818P). Around 680 mA of current is needed to produce 400 mW of power from the laser.

The beam is bounced off of a gold-coated mirror, and then focused on the sample. The beam is aligned along the rail that the sample stage is mounted on so that the beam and sample stage are always aligned in one

direction. The beam is focused by a 1" diameter, 2" focal length spherical plano-convex lens (Thorlabs part number LA1131-C) with antireflection coating for the near-IR. An optical chopper (Stanford Research Systems part number SR540) is placed in the beam path to provide modulation of the light for detection using a lock-in amplifier.

The light is collected and focused into an f = 320 mm grating spectrometer (Horiba-JY Micro-HR) for wavelength selection, which is controlled by the Fluoressence softare provided by Horiba. The light from the wafer is collected with 1" diameter, 2" focal length plano-convex lens (Thorlabs part number LA1131-C) with antireflection for the near-IR. When focused properly, this lens creates a collimated beam. This lens was chosen to have a large numerical aperture (NA). The NA can be calculated using

$$NA = \frac{f}{2D}, \tag{C1}$$

where f is the focal length of the lens and D is the diameter. It is also proportional to the sine of the collection angle. Thus, increasing the NA of the collection lens increases the amount of light captured. This is critical when trying to measure small signals.

The collimated beam produced by the collection lens is focused onto the entrance slit of the spectrometer using a 1" diameter, 4" focal length plano-convex lens (Thorlabs part number LA1509-C) with antireflection coating for the near-IR. The spectrometer has a numerical aperture (NA) of 0.125, which

is also the NA of the focusing lens. The spectrometer performs best when the NA of the lens is matched to that of the spectrometer.

As the light enters the spectrometer, it is bounced off of a convex mirror, which focuses the light onto a diffraction grating. The light reflected off of the grating is sent to another convex mirror that focuses the light onto the exit slit and into the detector housing. The detector housing contains a focusing mirror and a photodiode detector. The wavelength selection is performed by rotating the diffraction grating to allow the specified wavelength. The detector has a built-in transimpedance amplifier, which puts out a voltage that is proportional to the light intensity incident on the photodiode. Since the light is modulated by the optical chopper, the voltage on produced by the detector will oscillate at the same frequency. This signal is sent to the lock-in input via a BNC cable, and a reference signal is connected from the chopper controller to the reference input on the lock-in. The lock-in uses Fourier analysis and outputs a voltage that is proportional to the intensity of the light incident on the detector. By sweeping through a range of wavelengths and recording the voltage produced by the lock-in at each step, a luminescence spectrum is produced.

There are two exit slits on the spectrometer. Currently, only one is used. This is because we were originally going to connect the InGaAs multichannel detector (Princeton model OMA V) that is on the low temperature setup in PS-A2C. In fact, the exit slit has a custom flange specifically for that detector.

However, we did not ever connect this detector, as we were getting good results using the single-channel detectors.

There are two single-channel photodiode detectors. Both are cooled to reduce noise. One has a Ge photodiode, while the other has an extended InGaAs photodiode. The Ge detector (Electro-Optical systems part number G-050-TE2-H) is powered and TEC-cooled by an external power supply (Electro-Optical Systems part number PS/TC-1). It can detect wavelengths in the range 0.8-1.8 μm. It should be held at -30 °C during use. The InGaAs detector (Electro-optical systems part number IGA2.2 010-LN7) is powered by an external power supply (Electro-Optical Systems part number PS-1) and cooled via LN_2. It can detect wavelengths in the range 1.3-2.3 μm. The dewar should be filled with the power to the detector off. It must be filled slowly over the course of several minutes, or it will overflow. Having the detector cooled is essential for obtaining a good signal-to-noise ratio. The InGaAs detector is the most sensitive of the two.

The entrance and exit slits of the spectrometer determine how much light gets through it and the bandwidth of the admitted light. The wider the slits, the more light gets through the spectrometer and the larger the bandwidth. Thus, if you want fine wavelength resolution, you should keep the slits as narrow as possible. If you want light throughput, open them all the way. Often, the signal from the laser is used as a reference peak for PL spectra. The Ge detector can capture the fundamental wavelength, while the InGaAs detector captures the first harmonic. When sending the laser through

the spectrometer, care must be taken not to saturate the detector. If the 1064 nm long pass filter is in place, the slits can be all the way open. Without the filter, the slits must be narrow. It is always good practice to keep the slits closed and only open them as much as necessary.

The luminescence spectra are obtained using Fluoressence. Most of the guidelines for using lock-in amplifiers for this type of measurement are described in Appendix B. For this system, the frequency of the chopper is not really limited by the speed of the circuit, so I typically used 190 Hz. The time constants used on the lock-in are typically 1-10 s. Fluoressence also has an input for the integration time. This is the time the software waits before reading the voltage from the lock-in after setting the wavelength on the spectrometer. This should always be at least 5 times the time constant used on the lock-in. The software also has an option for auto gain, which means that it sets the sensitivity on the lock-in automatically. This does not work very well. It is best to set the gain for the maximum signal in the spectrum. It helps if you know where the peak is going to be. If not, it can take some manual scanning to see where the peak is. You can also use the peak from the laser as a reference, but the intensity of the PL may be very weak comparatively.

The key to getting good data from samples that have very weak luminescence is to have the optics aligned perfectly for maximum signal. Accordingly, I have developed some alignment procedures, which can be followed for optimal alignment of the optics. The following procedure

outlines how to align the laser, optics, and sample to the spectrometer. It assumes the optical breadboard and spectrometer are already aligned to the optical table. The alignment is extremely sensitive, and it requires a very light touch. It is also easy to knock it out of alignment by bumping any of the components. Alignment of the entire system should be done using a sample that is known to luminesce and a specific wavelength (e.g. bulk Ge). Before starting the procedure, make sure the slits on the spectrometer are closed and the laser is on. There is an IR target (threaded for use with Thorlabs SM1 components), and there are a few IR cards. They all have a phosphorescent material on them so that they luminesce in the visible when they are hit with an IR beam. This allows you to view the beam for alignment. One IR card is cut in half, which is especially useful for getting in small places, like the spectrometer entrance. The procedure below is for alignment of the entire optical system. If the system is already aligned and you have mounted a new sample, start at step 13.

System alignment procedure

1. Turn on the laser and turn up the power to 50-100 mW.
2. Set the spectrometer to the wavelength of the laser or the first harmonic.
3. Attach a rail to the breadboard in front of the laser along the axis of the beam. Mount a post on the rail so that it can slide along the beam path. Mount the IR target on top of the post and use it view the beam. The laser is on a mount that can adjust the height, pitch, and yaw. Adjust the pitch

and yaw so that the laser is aligned to the axis created by the breadboard and rail. This can be done by checking the vertical and horizontal position of the beam on the IR target at two different positions along the rail. When it is aligned, the beam position on the target will not change no matter where it is located along the rail. Once it is aligned, this rail is no longer needed.

4. Mount the gold-coated mirror on the longer, permanent rail directly in front of the laser. Use it to direct the beam down the axis of the rail, using the adjustment knobs on the kinematic mirror mount. The beam should be perfectly centered on the rail, and it should be aligned vertically and horizontally. Again, use the IR target mounted on a pole that can slide along the rail.
5. Mount the glass slide with the wafer on the sample stage. Mount a rail to the x-y stage that is on the breadboard below the spectrometer entrance slit so that it is aligned along the beam path. Reflect the laser off the surface of the wafer toward the spectrometer entrance slit. The beam does not need to be hitting the spectrometer entrance perfectly at this point. Use the adjustment knobs on the sample stage to align the beam to the axis of the rail and breadboard. Again, use the IR target mounted on a post that can slide along the rail to aid in alignment. The beam should be stay at the same position on the IR target as it moves along the rail.
6. The post that holds the sample stage is also mounted to the rail. Slide the post along the rail until the beam is centered horizontally about the

spectrometer slit. If you keep the exit slit all the way closed, it is okay to open the entrance slit. No light should get to the detector. Opening the entrance slit a bit can act as a visual aid in alignment. Get it as centered as possible, and then lock it in place by tightening the thumbscrew at the base of the mount.

7. Open the entrance slit all the way. There is a metal strip just past the entrance slit that has some apertures, which can aid in alignment. Use the aperture that is a wide rectangle. This allows you to see the vertical alignment of the beam with respect to the spectrometer. Since the beam is contained to a horizontal plane, the vertical height of the beam can be adjusted by rotating the sleeve on the bottom of the laser mount. Adjust the vertical height of the beam until it is centered on the aperture. Once this is done, beam path is set, and we are ready to put in the optics.
8. Mount the laser focusing lens on the rail in the beam path with the flat side of the lens facing the sample. Adjust the height of the lens so that the laser is hitting the center of the lens. By putting the IR card on the other side of the lens, you should be able to see the beam focusing. Position the lens so that the focused spot is incident on the sample surface. Now, the beam will still reflect off the wafer, but it will not be collimated. Instead, it will diverge as if it were a point source. Still, you should be able to see the beam at the entrance slit of the spectrometer clearly with the IR card. The spot will be larger, but it still gives you an idea of the alignment. If the vertical position of the beam relative to the entrance slit is off, you need

to adjust the height of the lens until it is centered. If the horizontal alignment is off, you need to rotate the lens slightly. Fine adjustments can also be made using the knobs on the kinematic mount for the lens.

9. Mount the collection lens on a post on the x-y stage in front of sample with the flat side toward the sample. This lens takes the diverging light and creates a collimated beam. When positioned correctly, the laser beam will be centered on the entrance slit of the spectrometer. This lens is identical to the laser focusing lens, so it should be the same distance from the focused spot on the wafer. Adjust the x-y stage to get the centered on the lens. Adjust the height of the lens until the beam is centered on the rectangular aperture behind the entrance slit. Adjust the position along the beam path until you have a collimated beam. The beam spot on the IR target should stay constant in size as you slide the target along the rail. Continue adjusting all parameters until you have a beam that is aligned along the axis of the rail, perfectly collimated, and centered on the entrance slit.
10. Now the focusing lens is inserted. This takes the collimated beam and focuses it to a spot on the spectrometer entrance slit. Remove the rail on the x-y stage and mount the focusing lens on a post on the stage with the flat side of the lens toward the spectrometer. The focusing lens has a 4" focal length, but the working distance is more like 3.5", and that is the distance it should be away from the entrance slit. Adjust the height of the lens until the beam goes through the center of the lens and the focused

spot is centered vertically on the spectrometer entrance. Adjust the tilt and position of the lens until a perfectly focused spot is centered on the entrance slit as closely as possible.

11. Close the entrance slit. Open the exit slit a tiny bit. Slowly open the entrance slit until you see signal on the lock-in. The laser is very powerful, so the slit just barely needs to be open. Use the reading on the lock-in as a guide to finely adjust the position of the focusing lens. The goal is to maximize the signal. Once this is done, the optics are aligned.
12. Carefully rotate the sample stage (counter-clockwise looking down) until the reflected beam no longer hits the collection lens.
13. Increase the laser power to 400 mW.
14. Loosen the thumbscrew at the base of the mount for the sample stage so that it can slide along the rail. You will probably need to open up the slits a little more to see a good amount of signal. Slide the mount along the rail until the signal is maximized. This has to be done with a very light touch. Do not even lean on the table. Tighten the thumbscrew at the base of the mount to lock it in place. This actually moves it slightly, so it can be difficult to get it locked in place with maximum signal.
15. Adjust the position of the laser focusing lens along the rail to get maximum signal.
16. Adjust the thumbscrews on the back of the sample stage to get maximum signal. This must be done with a very light touch.

17. Adjust the position of the collection lens in the direction perpendicular to the beam path to get maximum signal.
18. Adjust the position of the focusing lens in the direction perpendicular to the beam path to get maximum signal.
19. Adjust the position of the collection lens in the direction parallel to the beam path to get maximum signal.
20. Adjust the position of the focusing lens in the direction parallel to the beam path to get maximum signal.
21. Put the 1064 nm long pass filter in place. Set the spectrometer to the wavelength that the sample is known to luminesce at. You should be able to see the luminescence strongly. If not, go through the procedure again.

Calibration of the spectrometer can be performed by measuring the spectrum of a gas discharge lamp, such as the Ne lamp in the lab. It helps if the system is already aligned. Start with the entrance and exit slits closed. Remove the sample stage and collection lens, and position the lamp so that the arc source is aligned along the beam path for the spectrometer entrance. Mount an iris on a pole and position it in the beam path on the optical table to create a narrow (~2-3 mm) beam that hits the center of the focusing lens. Adjust the focus until the beam is focused on the entrance slit. Insert a long pass filter in the beam path. Once this is done, the spectrum can be obtained and compared with the known wavelengths of the atomic transitions. Take a spectrum with very narrow spacing (0.1-0.2 nm). Reference data can be

obtained on the NIST website. Once you know how much the spectometer is off, you can follow the calibration procedure in the Fluoressence manual.

When taking spectra that include the laser wavelength or its first harmonic, it is important to use a long pass filter to block the laser light. There are several long pass filters in the lab, but the 1064 nm long pass has the highest optical density at the laser wavelength. Even using that filter, the peak from the laser is still visible. The data can be corrected by fitting the curves with Gaussian peaks and subtracting the laser peak from the measured data.

I measured the transmittance of the filters by recording the spectrum of a halogen lamp with and without the filters in place. The transmittance is the ratio of the intensity with the filter to the intensity without the filter. The transmittance curves are presented in FIG. C3. In each case, there is a step at twice the cutoff wavelength. In the case of the 1064 nm filter, this occurs around 2150 nm. This leads to a discontinuity in the measured PL spectrum if there is emission around that wavelength.

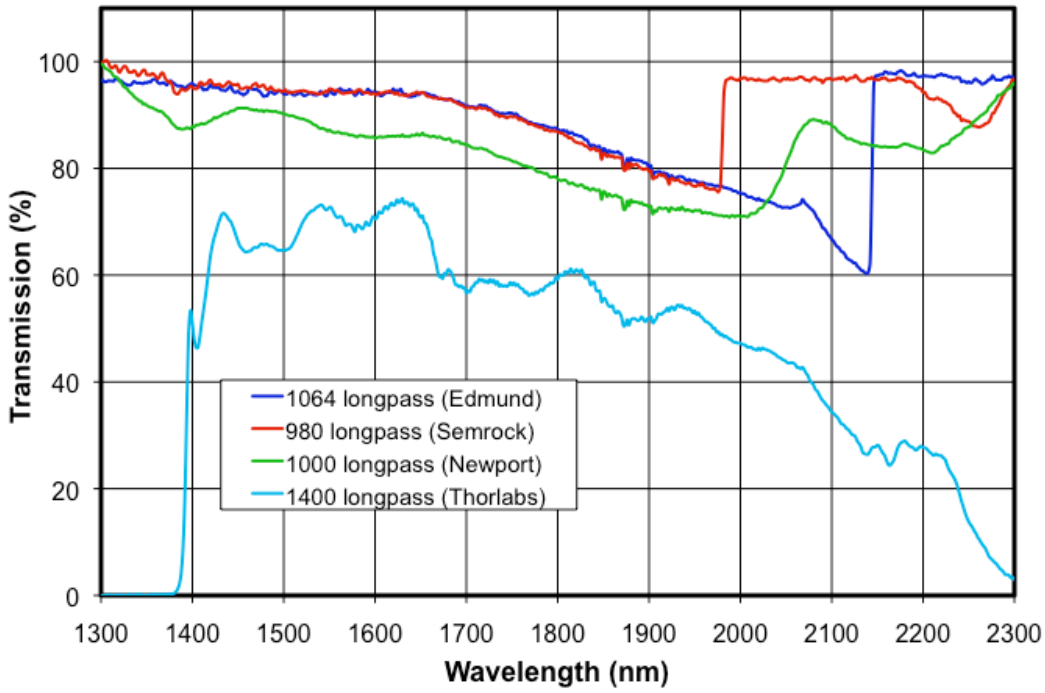

FIG. C3. Measured transmittance curves for various long pass filters.

This optical system can also be used for electroluminescence measurements in the same wavelength range. A schematic of the system is presented in FIG. A2. It is a modified version of the PL system. In this case, there is no optical excitation, so the laser is not used. Instead, a power supply (Keithley model 2602A) is used to run current through the diode under forward bias.

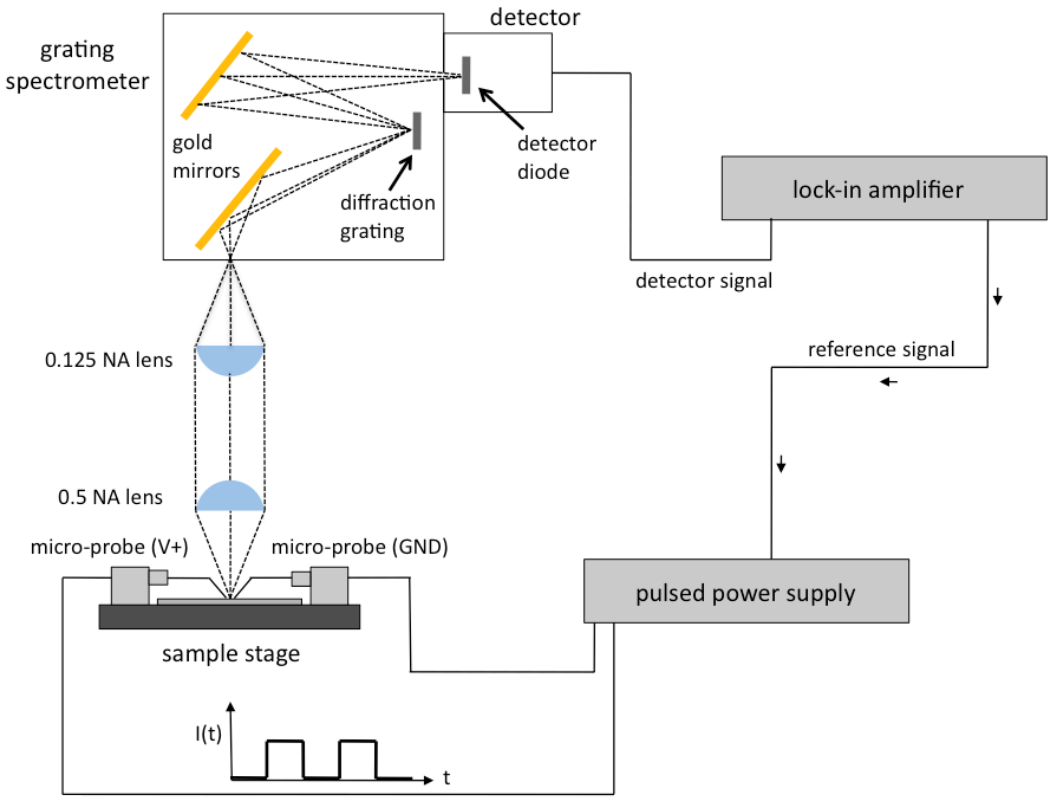

FIG. C2. Schematic of electroluminescence measurement system.

To modify the apparatus for EL measurements, you must remove the PL sample stage, the collection lens, and the laser focusing lens. The sample stages is an x-y stage with a steel plate. The wafer is placed on the plate with the two micro-probes with magnetic bases. Electrical connections are made from the probes to channel 1 on the power supply, and the probes are connected to the device pads on the wafer. The light produced from the device is directed vertically, rather than horizontally, so the light must is collected with a vertically mounted lens. There is an L-shaped 30 mm cage assembly with 1” diameter, 1” focal length plano-convex lens (Thorlabs part number LA1951-C) with antireflection coating for the near-IR lens on one

end. The lens is on a micrometer driven assembly for precision focusing. Mount the cage assembly to the optical breadboard so that the lens is directly over the device. There is a gold mirror at the corner of the L for deflecting the beam toward the spectrometer. The cage assembly must be placed such that the beam reflected from the mirror with pass through the center of the focusing lens and into the spectrometer entrance. Aligning the cage assembly to the spectrometer can be done by replacing the collection lens with a red LED. This gives you a visible beam to work with.

Once the cage assembly is aligned to the spectrometer, the electrical connections can be made to the device. The signal from the detector is measured using the lock-in, as in the PL experiments. Thus, our source must be modulated. In the case of PL, this was accomplished by using the optical chopper. Here, we must somehow "chop" the current. This is done by pulsing the current from the power supply. Keithley has its own TestScript language from programming the power supply. I have written a program in their TestScriptBuilder software for this. A TTL reference signal (square wave) is generated by the lock-in and sent to of the digital inputs on the power supply. When the power supply detects an edge, it produces a pulse. The pulse width is set by the user to be exactly one half the period. This produces a modulated current source for driving the diode. Once the program is run, the pulse train continues until a switch is flipped, which breaks the loop. This switch is connected to another digital input on the power supply.

Measurement of the spectrum is performed using Fluoressence, as in the PL experiments. In fact, there is no difference here in the way data is collected. The same rules and caveats for using the lock-in still apply. The wafer and electrical probes are on an x-y stage so that individual devices can be focused on. Unfortunately, the only light to use as a reference for focusing is the EL signal. If the peak wavelength is known, then you can set the spectrometer to that wavelength and move the x-y stage until the signal is maximized. If the peak wavelength is not known, you can roughly position the device in the following way. There is a small, blue, fiber-coupled halogen lamp. There is a 30 mm cage plate with a fiber collimation lens that has an SMA connector. Connect a fiber between the lamp and the cage plate, and then attach the cage plate to the end of the cage assembly. This will direct the light down the axis of the cage and focus on the wafer. Move the x-y stage until the device is in the spot. Now you can remove the light source and try to take a spectrum. Once you see some signal, you can move to the peak wavelength and focus from there.

APPENDIX D

PERMISSIONS FOR REPRINTED MATERIALS

This appendix contains the licensing agreements and permissions for the materials in this dissertation that have been reprinted from other sources.

Powered by RIGHTSLINK COPYRIGHT CLEARANCE CENTER, INC. Home Account Info Help

Title:	Direct-gap photoluminescence with tunable emission wavelength in Ge1−ySny alloys on silicon	Logged in as: Jay Mathews Account #: 3000378534
Author:	J. Mathews, R. Beeler, J. Tolle, et al	LOGOUT
Publication:	Applied Physics Letters	
Volume/Issue	97/22	
Publisher:	American Institute of Physics	
Date:	Dec 2, 2010	
Page Count:	3	
ID:	To be determined	

Copyright © 2010, American Institute of Physics

Order Completed

Thank you very much for your order.

This is a License Agreement between Jay Mathews ("You") and American Institute of Physics ("AIP"). The license consists of your order details, the terms and conditions provided by American Institute of Physics, and the payment terms and conditions.

Get the printable license.

License Number	2606070083512
License date	Feb 11, 2011
Licensed content publisher	American Institute of Physics
Licensed content publication	Applied Physics Letters
Licensed content title	Direct-gap photoluminescence with tunable emission wavelength in Ge1−ySny alloys on silicon
Licensed content author	J. Mathews, R. Beeler, J. Tolle, et al
Licensed content date	Dec 2, 2010
Volume number	97
Issue number	22
Type of Use	Thesis/Dissertation
Requestor type	Author (original article)
Format	Print
Portion	Figure/Table
Number of figures/tables	1
Title of your thesis / dissertation	Investigation of light absorption and emission in Ge and GeSn films grown on Si
Expected completion date	Apr 2011
Estimated size (number of pages)	100

Total 0.00 USD

ORDER MORE... CLOSE WINDOW

Copyright © 2011 Copyright Clearance Center, Inc. All Rights Reserved. Privacy statement.
Comments? We would like to hear from you. E-mail us at customercare@copyright.com

ELSEVIER LICENSE
TERMS AND CONDITIONS

Jan 28, 2011

This is a License Agreement between Jay Mathews ("You") and Elsevier ("Elsevier") provided by Copyright Clearance Center ("CCC"). The license consists of your order details, the terms and conditions provided by Elsevier, and the payment terms and conditions.

All payments must be made in full to CCC. For payment instructions, please see information listed at the bottom of this form.

Supplier	Elsevier Limited The Boulevard,Langford Lane Kidlington,Oxford,OX5 1GB,UK
Registered Company Number	1982084
Customer name	Jay Mathews
Customer address	1851 E University Dr
	Tempe, AZ 85281
License number	2597721270462
License date	Jan 28, 2011
Licensed content publisher	Elsevier
Licensed content publication	Materials Science in Semiconductor Processing
Licensed content title	Germanium: From its discovery to SiGe devices
Licensed content author	E.E. Haller
Licensed content date	August-October 2006
Licensed content volume number	9
Licensed content issue number	4-5
Number of pages	15
Start Page	408
End Page	422
Type of Use	reuse in a thesis/dissertation
Portion	figures/tables/illustrations
Number of figures/tables /illustrations	2
Format	both print and electronic

Are you the author of this Elsevier article?	No
Will you be translating?	No
Order reference number	
Title of your thesis/dissertation	Investigation of light absorption and emission in Ge and GeSn films grown on Si
Expected completion date	Apr 2011
Estimated size (number of pages)	100
Elsevier VAT number	GB 494 6272 12
Permissions price	0.00 USD
Value added tax 0.0%	0.0 USD / 0.0 GBP
Total	0.00 USD
Terms and Conditions	

INTRODUCTION

1. The publisher for this copyrighted material is Elsevier. By clicking "accept" in connection with completing this licensing transaction, you agree that the following terms and conditions apply to this transaction (along with the Billing and Payment terms and conditions established by Copyright Clearance Center, Inc. ("CCC"), at the time that you opened your Rightslink account and that are available at any time at http://myaccount.copyright.com).

GENERAL TERMS

2. Elsevier hereby grants you permission to reproduce the aforementioned material subject to the terms and conditions indicated.

3. Acknowledgement: If any part of the material to be used (for example, figures) has appeared in our publication with credit or acknowledgement to another source, permission must also be sought from that source. If such permission is not obtained then that material may not be included in your publication/copies. Suitable acknowledgement to the source must be made, either as a footnote or in a reference list at the end of your publication, as follows:

"Reprinted from Publication title, Vol /edition number, Author(s), Title of article / title of chapter, Pages No., Copyright (Year), with permission from Elsevier [OR APPLICABLE SOCIETY COPYRIGHT OWNER]." Also Lancet special credit - "Reprinted from The Lancet, Vol. number, Author(s), Title of article, Pages No., Copyright (Year), with permission from Elsevier."

4. Reproduction of this material is confined to the purpose and/or media for which permission is hereby given.

5. Altering/Modifying Material: Not Permitted. However figures and illustrations may be altered/adapted minimally to serve your work. Any other abbreviations, additions, deletions and/or any other alterations shall be made only with prior written authorization of Elsevier Ltd. (Please contact Elsevier at permissions@elsevier.com)

6. If the permission fee for the requested use of our material is waived in this instance, please be advised that your future requests for Elsevier materials may attract a fee.

7. Reservation of Rights: Publisher reserves all rights not specifically granted in the combination of (i) the license details provided by you and accepted in the course of this licensing transaction, (ii) these terms and conditions and (iii) CCC's Billing and Payment terms and conditions.

8. License Contingent Upon Payment: While you may exercise the rights licensed immediately upon issuance of the license at the end of the licensing process for the transaction, provided that you have disclosed complete and accurate details of your proposed use, no license is finally effective unless and until full payment is received from you (either by publisher or by CCC) as provided in CCC's Billing and Payment terms and conditions. If full payment is not received on a timely basis, then any license preliminarily granted shall be deemed automatically revoked and shall be void as if never granted. Further, in the event that you breach any of these terms and conditions or any of CCC's Billing and Payment terms and conditions, the license is automatically revoked and shall be void as if never granted. Use of materials as described in a revoked license, as well as any use of the materials beyond the scope of an unrevoked license, may constitute copyright infringement and publisher reserves the right to take any and all action to protect its copyright in the materials.

9. Warranties: Publisher makes no representations or warranties with respect to the licensed material.

10. Indemnity: You hereby indemnify and agree to hold harmless publisher and CCC, and their respective officers, directors, employees and agents, from and against any and all claims arising out of your use of the licensed material other than as specifically authorized pursuant to this license.

11. No Transfer of License: This license is personal to you and may not be sublicensed, assigned, or transferred by you to any other person without publisher's written permission.

12. No Amendment Except in Writing: This license may not be amended except in a writing signed by both parties (or, in the case of publisher, by CCC on publisher's behalf).

13. Objection to Contrary Terms: Publisher hereby objects to any terms contained in any purchase order, acknowledgment, check endorsement or other writing prepared by you, which terms are inconsistent with these terms and conditions or CCC's Billing and Payment terms and conditions. These terms and conditions, together with CCC's Billing and Payment terms and conditions (which are incorporated herein), comprise the entire agreement

between you and publisher (and CCC) concerning this licensing transaction. In the event of any conflict between your obligations established by these terms and conditions and those established by CCC's Billing and Payment terms and conditions, these terms and conditions shall control.

14. Revocation: Elsevier or Copyright Clearance Center may deny the permissions described in this License at their sole discretion, for any reason or no reason, with a full refund payable to you. Notice of such denial will be made using the contact information provided by you. Failure to receive such notice will not alter or invalidate the denial. In no event will Elsevier or Copyright Clearance Center be responsible or liable for any costs, expenses or damage incurred by you as a result of a denial of your permission request, other than a refund of the amount(s) paid by you to Elsevier and/or Copyright Clearance Center for denied permissions.

LIMITED LICENSE

The following terms and conditions apply only to specific license types:

15. **Translation**: This permission is granted for non-exclusive world **English** rights only unless your license was granted for translation rights. If you licensed translation rights you may only translate this content into the languages you requested. A professional translator must perform all translations and reproduce the content word for word preserving the integrity of the article. If this license is to re-use 1 or 2 figures then permission is granted for non-exclusive world rights in all languages.

16. **Website**: The following terms and conditions apply to electronic reserve and author websites:
Electronic reserve: If licensed material is to be posted to website, the web site is to be password-protected and made available only to bona fide students registered on a relevant course if:
This license was made in connection with a course,
This permission is granted for 1 year only. You may obtain a license for future website posting,
All content posted to the web site must maintain the copyright information line on the bottom of each image,
A hyper-text must be included to the Homepage of the journal from which you are licensing at http://www.sciencedirect.com/science/journal/xxxxx or the Elsevier homepage for books at http://www.elsevier.com , and
Central Storage: This license does not include permission for a scanned version of the material to be stored in a central repository such as that provided by Heron/XanEdu.

17. **Author website** for journals with the following additional clauses:

All content posted to the web site must maintain the copyright information line on the bottom of each image, and
he permission granted is limited to the personal version of your paper. You are not allowed

to download and post the published electronic version of your article (whether PDF or HTML, proof or final version), nor may you scan the printed edition to create an electronic version,
A hyper-text must be included to the Homepage of the journal from which you are licensing at http://www.sciencedirect.com/science/journal/xxxxx , As part of our normal production process, you will receive an e-mail notice when your article appears on Elsevier's online service ScienceDirect (www.sciencedirect.com). That e-mail will include the article's Digital Object Identifier (DOI). This number provides the electronic link to the published article and should be included in the posting of your personal version. We ask that you wait until you receive this e-mail and have the DOI to do any posting.
Central Storage: This license does not include permission for a scanned version of the material to be stored in a central repository such as that provided by Heron/XanEdu.

18. **Author website** for books with the following additional clauses:
Authors are permitted to place a brief summary of their work online only.
A hyper-text must be included to the Elsevier homepage at http://www.elsevier.com

All content posted to the web site must maintain the copyright information line on the bottom of each image
You are not allowed to download and post the published electronic version of your chapter, nor may you scan the printed edition to create an electronic version.
Central Storage: This license does not include permission for a scanned version of the material to be stored in a central repository such as that provided by Heron/XanEdu.

19. **Website** (regular and for author): A hyper-text must be included to the Homepage of the journal from which you are licensing at http://www.sciencedirect.com/science/journal/xxxxx. or for books to the Elsevier homepage at http://www.elsevier.com

20. **Thesis/Dissertation**: If your license is for use in a thesis/dissertation your thesis may be submitted to your institution in either print or electronic form. Should your thesis be published commercially, please reapply for permission. These requirements include permission for the Library and Archives of Canada to supply single copies, on demand, of the complete thesis and include permission for UMI to supply single copies, on demand, of the complete thesis. Should your thesis be published commercially, please reapply for permission.

21. **Other Conditions**:

v1.6

Gratis licenses (referencing $0 in the Total field) are free. Please retain this printable license for your reference. No payment is required.

If you would like to pay for this license now, please remit this license along with your payment made payable to "COPYRIGHT CLEARANCE CENTER" otherwise you will be invoiced within 48 hours of the license date. Payment should be in the form of a check or money order referencing your account number and this invoice number RLNK10921606.
Once you receive your invoice for this order, you may pay your invoice by credit card. Please follow instructions provided at that time.

Make Payment To:
Copyright Clearance Center
Dept 001
P.O. Box 843006
Boston, MA 02284-3006

If you find copyrighted material related to this license will not be used and wish to cancel, please contact us referencing this license number 2597721270462 and noting the reason for cancellation.

Questions? customercare@copyright.com or +1-877-622-5543 (toll free in the US) or +1-978-646-2777.

Jay Mathews <jamathew@asu.edu>

Re: Request for permission to reprint figure

j.hansson@ieee.org <j.hansson@ieee.org> **28 January 2011 19:21**
Reply-To: Pubs-Permissions@ieee.org
To: Jay Mathews <jamathew@asu.edu>

Comments/Response to Case ID: 005FE48D

ReplyTo: Pubs-Permissions@ieee.org

From: Jacqueline Hansson Date: 01/28/2011

Subject: Re: Request for permission to reprint figure

Send To: Jay Mathews <jamathew@asu.edu>

cc:

Dear Jay Mathews:

We are happy to grant you permission to reuse the IEEE copyrighted figuresrequested in all electronic and printed formats.

Since the figure is for use in your thesis, our only requirements are that you credit the original source (author, paper, and publication), and that the IEEE copyright line (©© 1955 IRE (now IEEE). Reprinted, with permission, from (full journal name; volume, issue, and page numbers; month/year of issue) [1955 IEEE) appears prominently with the reprinted figure.

Sincerely,

Jacqueline Hansson, Coordinator
© © © © © © © © © © © © © © © © © ©
IEEE Intellectual Property Rights Office
445 Hoes Lane
Piscataway, NJ 08855-1331 USA
+1 732 562 3966 (phone)
+1 732 562 1746 (fax)

IEEE-- Fostering technological innovation

NATURE PUBLISHING GROUP LICENSE
TERMS AND CONDITIONS

Feb 12, 2011

This is a License Agreement between Jay Mathews ("You") and Nature Publishing Group ("Nature Publishing Group") provided by Copyright Clearance Center ("CCC"). The license consists of your order details, the terms and conditions provided by Nature Publishing Group, and the payment terms and conditions.

All payments must be made in full to CCC. For payment instructions, please see information listed at the bottom of this form.

License Number	2606640712966
License date	Feb 12, 2011
Licensed content publisher	Nature Publishing Group
Licensed content publication	Nature Photonics
Licensed content title	High-performance Ge-on-Si photodetectors
Licensed content author	Jurgen Michel, Jifeng Liu, Lionel C. Kimerling
Licensed content date	Jul 30, 2010
Type of Use	reuse in a thesis/dissertation
Requestor type	academic/educational
Format	print and electronic
Portion	figures/tables/illustrations
Number of figures/tables /illustrations	1
High-res required	no
Figures	Figure 2. The effect of tensile strain on the band structure of Ge.
Author of this NPG article	no
Your reference number	
Title of your thesis / dissertation	Investigation of light absorption and emission in Ge and GeSn films grown on Si
Expected completion date	Apr 2011
Estimated size (number of pages)	100
Total	0.00 USD
Terms and Conditions	

Terms and Conditions for Permissions

Nature Publishing Group hereby grants you a non-exclusive license to reproduce this material for this purpose, **and for no other use**, subject to the conditions below:

1. NPG warrants that it has, to the best of its knowledge, the rights to license reuse of this material. However, you should ensure that the material you are requesting is original to Nature Publishing Group and does not carry the copyright of another entity (as credited in the published version). If the credit line on any part of the material you have requested indicates that it was reprinted or adapted by NPG with permission from another source, then you should also seek permission from that source to reuse the material.

2. Permission granted free of charge for material in print is also usually granted for any electronic version of that work, provided that the material is incidental to the work as a whole and that the electronic version is essentially equivalent to, or substitutes for, the print version.

   Where print permission has been granted for a fee, separate permission must be obtained for any additional, electronic re-use (unless, as in the case of a full paper, this has already been accounted for during your initial request in the calculation of a print run).

   NB: In all cases, web-based use of full-text articles must be authorized separately through the 'Use on a Web Site' option when requesting permission.

3. Permission granted for a first edition does not apply to second and subsequent editions and for editions in other languages (except for signatories to the STM Permissions Guidelines, or where the first edition permission was granted for free).

4. Nature Publishing Group's permission must be acknowledged next to the figure, table or abstract in print. In electronic form, this acknowledgement must be visible at the same time as the figure/table/abstract, and must be hyperlinked to the journal's homepage.

5. The credit line should read:

   Reprinted by permission from Macmillan Publishers Ltd: [JOURNAL NAME] (reference citation), copyright (year of publication)

   For AOP papers, the credit line should read:

   Reprinted by permission from Macmillan Publishers Ltd: [JOURNAL NAME], advance online publication, day month year (doi: 10.1038/sj.[JOURNAL ACRONYM].XXXXX)

6. Adaptations of single figures do not require NPG approval. However, the adaptation should be credited as follows:

   Adapted by permission from Macmillan Publishers Ltd: [JOURNAL NAME] (reference citation), copyright (year of publication)

7. Translations of up to a whole article do not require NPG approval. The translation should be credited as follows:

   Translated by permission from Macmillan Publishers Ltd: [JOURNAL NAME] (reference citation), copyright (year of publication)

We are certain that all parties will benefit from this agreement and wish you the best in the use of this material. Thank you.

Gratis licenses (referencing $0 in the Total field) are free. Please retain this printable license for your reference. No payment is required.

If you would like to pay for this license now, please remit this license along with your payment made payable to "COPYRIGHT CLEARANCE CENTER" otherwise you will be invoiced within 48 hours of the license date. Payment should be in the form of a check or money order referencing your account number and this invoice number RLNK10930337.
Once you receive your invoice for this order, you may pay your invoice by credit card. Please follow instructions provided at that time.

Make Payment To:
Copyright Clearance Center
Dept 001
P.O. Box 843006
Boston, MA 02284-3006

If you find copyrighted material related to this license will not be used and wish to cancel, please contact us referencing this license number 2606640712966 and noting the reason for cancellation.

Questions? customercare@copyright.com or +1-877-622-5543 (toll free in the US) or +1-978-646-2777.